Liquid-Liquid Phase Separation and Intermolecular Interactions in Dense Protein Solutions

High Pressure SAXS Studies on Lysozyme Solutions of High Ionic Strength

Dissertation

zur Erlangung des Doktorgrades der Naturwissenschaften

der Fakultät Physik der Technischen Universität Dortmund

vorgelegt von

Dipl. Phys. Johannes Möller

März 2014

technische universität
dortmund

Contents

1 Introduction

Proteins are biological macromolecules, responsible for several structural and functional tasks in the human body. The structural investigation of these macromolecules has considerably increased in recent years due to the strong connection between the shape and conformation of a protein and its biological function. More and more studies reveal relations between diseases and structural deformations of bio-molecules and their consequential malfunction. Many protein structures were solved by X-ray crystallography, which is the most successful technique to determine the atomic structure of macromolecules. A three dimensional representation of the protein lysozyme is depicted in fig. 1.1. However, the determination of a protein structure with atomic resolution by X-ray diffraction requires the production of high quality protein crystals, which is a bottleneck in current research. Improved methods to increase the capability of handling proteins for storage as well as investigation purposes are therefore constantly needed.

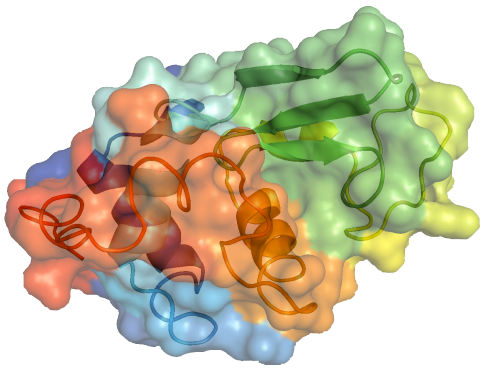

Figure 1.1: *The protein lysozyme.*

The native environment for a protein is in an aqueous, crowded solution. Highly concentrated protein solutions were found to yield a large number of different phases, like amorphous aggregates, gels, crystals, or a liquid-liquid phase separation, which are all governed by the underlying protein-protein interactions in water. Microscopy pictures of solution forming a liquid-liquid phase separation and a protein crystal are shown in fig. 1.2. The liquid-liquid phase separation (LLPS) is formed by two coexisting solutions that differ in their protein concentration. Small, micrometer-sized droplets with a high protein density are formed, surrounded by a less dense protein solution. Attractive protein-protein interactions, typically in highly concentrated protein solutions, are needed to

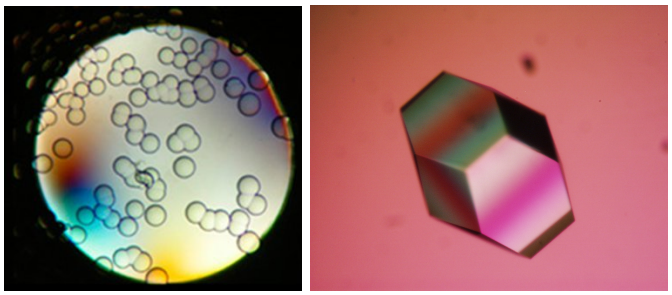

Figure 1.2: *Different phases can form in a protein solution, i.e., a liquid-liquid phase separated state (picture taken from [Dumetz et al., 2008]) or a protein crystal (picture taken from [Wikimedia, 2014]).*

induce such phase transitions from the dissolved protein to an aggregated or phase separated state. Understanding and tuning those intermolecular interaction potentials and with that the phase behavior of highly concentrated protein solutions is needed in several tasks, like for example protein purification or crystallization. Moreover, (self-)crowded protein environments are the typical *in vivo* environments of proteins, as macromolecular concentrations of up to 300 mg/ml can occur inside a living cell. Notably, proteins rarely crystallize even in these highly concentrated environments. For example, the human eye lens stays remarkably transparent for light, even though it is one of the most crowded environments in the human body. Several diseases, like cataract with a decreasing solubility of the protein γD-crystallin in the human eye lens, are directly connected to phase separation and aggregation phenomena of proteins. For these reasons, fundamental knowledge on the physical properties which govern protein-protein interactions and the resulting phase and crystallization behavior of proteins are of strong interest.

The interactions present in dense protein solutions are highly complex. Changes in the aqueous environment influence the inter- and intramolecular protein-protein interactions, the protein-solvent interactions, and the solvent-solvent interactions. Hence, a precise perturbation agent is needed, which is able to influence protein solutions in a controlled and reversible way. High hydrostatic pressure is used in this thesis, as it presents various preferable properties. Pressure is known as a relatively mild perturbation agent for soft matter systems that slightly weakens hydrophobic effects and even strengthens hydrogen bridges. The internal energy of a system is unchanged upon pressure increase, in contrast to investigations as a function of temperature. Additionally, the use of pressure is of considerable physiological and biotechnological interest, for example in deep sea biology and high pressure food processing. Therefore, the influence of pressure in the context of protein crystallization and phase separation is investigated in this thesis, emphasizing strongly attractive protein interactions.

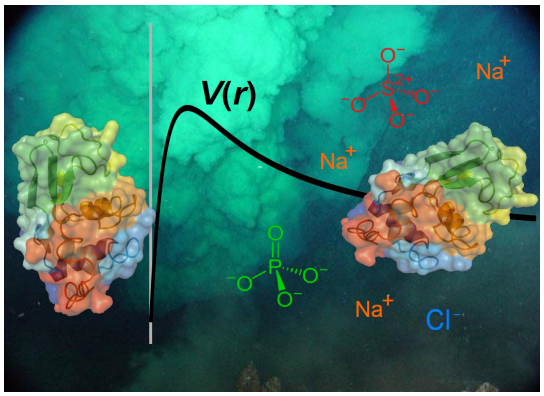

Figure 1.3: *The intermolecular interaction potential $V(r)$ is a function of temperature, pressure, and salt concentration. Furthermore, the type of salt influences the interaction potential. [Möller et al., 2014b]*

The focus of this thesis lies on the pressure dependence of the protein-protein interaction potential $V(r)$ as well as the resulting phase behavior in protein solutions of high ionic strength. Only few studies addressed the pressure dependence of protein-protein interaction potentials, systematic studies have been done on mainly repulsive interactions only. Furthermore, nothing is known about pressure effects on the liquid-liquid phase separation phenomena so far. To this purpose, small angle X-ray scattering (SAXS) experiments were conducted on dense lysozyme solution, with different parameters like salt concentration and type as well as temperature in combination with increasing hydrostatic pressure. SAXS is the ideal tool in this context as it gives structural information on

the length scale of several nanometers, which is in the size range of proteins and their intermolecular distances in crowded solutions. Therefore, the measured scattering intensity can give information on the structure of the investigated proteins, the interaction potential between the proteins, and the resulting phases formed. A liquid state theoretical approach is used to connect the obtained scattering information with the intermolecular interaction potential of the proteins. Furthermore, it will be shown that SAXS investigations are able to detect the phase transition in a protein solution, thus, rendering it an ideal tool to investigate the presented issues.

The chapters of this thesis are ordered as follows:

- First, a short review on proteins and the known implications of external parameters on inter- and intramolecular interactions is presented.
- In chapter 3, the theory of small angle X-ray scattering as well as tools for data analysation are introduced.
- A description of the experimental setup and the different beamlines at which SAXS experiments were conducted is given in chapter 4. The principle data handling and the established refinement routines are presented, too.
- The obtained results on the intermolecular interactions as function of various parameter, namely pressure, temperature, salt type, and salt concentration are presented in chapter 5.
- In chapter 6, interactions close to the phase boundary and the location of the liquid-liquid phase separation boundary as a function of pressure and temperature are discussed.

The results presented in this thesis are published in [Möller et al., 2012], [Möller et al., 2014a], and [Möller et al., 2014b].

2 Proteins Under Pressure

In this chapter, the use of hydrostatic pressure as a tool to investigate and tune proteins in solution will be introduced. A complete thermodynamical description of chemical systems includes knowledge on the response to external influences. In this context, pressure is one of the most fundamental thermodynamic variables. The use of pressure as perturbation agent in biophysical research presents several advantages, as it induces a very gentle disturbance to biochemical systems. First, non-covalent interactions are of major importance for the stability of biological systems. They can accurately be probed by pressure, in contrast to the major perturbations produced by changes in temperature or the chemical potential [Daniel et al., 2006]. Notably, a change in temperature results in a change of thermal energy and density of the considered system. The different influences can be distinguished by the additional use of pressure, which only changes the density of the system. Hence, pressure can be used to influence chemical equilibria and reaction rates, depending on the activation and reaction volumes involved [Daniel et al., 2006, Meersman et al., 2013].
Furthermore, nature has adapted to the most extreme habitats, forming life in extreme salinites, pH ranges, temperatures, or pressures. Deep sea environments with pressures up to the kbar range were found to host life forms that have adjusted considerably to these extreme conditions. Pressure dependent studies can provide knowledge on fundamental biochemical properties by revealing how nature has developed to deal with these extreme influences. Investigations of high pressure effects on biological model systems have for example been performed on folding and unfolding characteristics of proteins or the phase behavior of lipids [Daniel et al., 2006, Meersman et al., 2013]. Throughout these numerous studies, pressure has proven its value to probe structure and dynamics of proteins in solution.

The primary focus of this work lies on high pressure effects on the intermolecular interactions of proteins, which have been studied in much less extent so far. In the following chapter, the general structure of proteins and their interactions, intra- and intermolecular as well as with the surrounding solvent molecules, will be introduced. The influence of pressure and further external parameters on the stability of proteins will be discussed in order to establish the effect of external influences on inter- and intramolecular interactions. As the pressure effects on proteins are strongly determined by changes in the solvation and aqueous solution itself, changes in the water structure and the resulting solvation properties will also be introduced. In this context, different influences on protein systems will be discussed, like pressure, osmolytes, and salts.

2.1 Proteins

Soft matter systems can generally be classified into three distinct groups; colloids, polymers, and amphiphiles. All living matter, from DNA to cell membranes and proteins, can be described on the molecular level by the properties of these type of systems in aqueous solution.

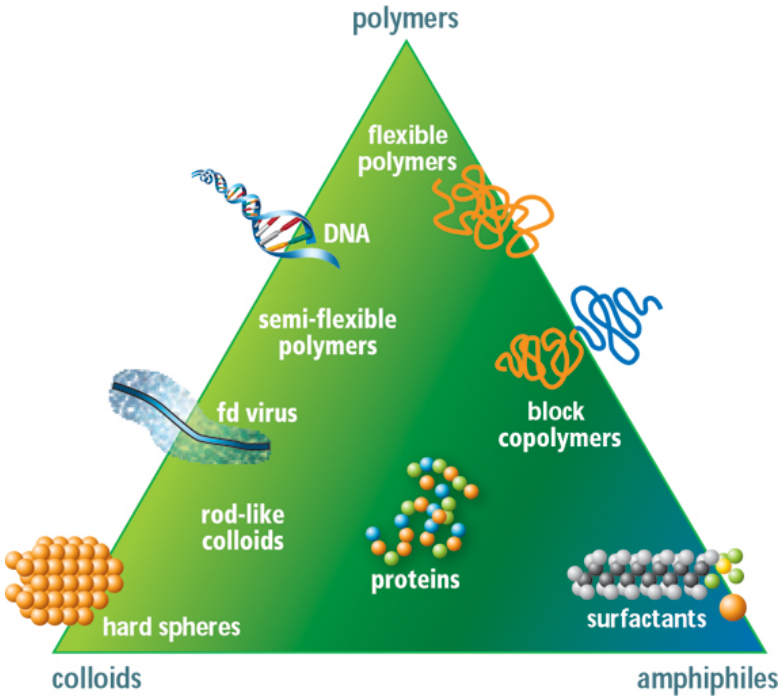

Figure 2.1: *The triangle of soft matter. Proteins are a special group of soft matter, as they combine the characteristics of polymers, colloids, and lipids. Picture taken from [Dhont et al., 2008].*

Proteins present one specific class of soft matter as they combine different characteristic attributes of soft matter systems. They address different functions in biochemistry, being responsible for replicating DNA, responding to external and internal stimuli, transporting molecules, and many more tasks. In the *Escherichia coli* cell, proteins constitute half of the dry weight [Voet et al., 2005]. Basically, proteins are linear polymers, consisting of a linear chain of amino acids. Since many proteins exist natively in a globular, very compact form, solvated proteins can often be described as colloidal particles. The strong interplay between hydrophobic and hydrophilic interactions in protein folding may also be seen as a resemblance to the behavior of surfactants. There are 20 standard proteinogenic amino acids, which are encoded directly by triplet codons in the DNA. The vast functional and structural variety of proteins is founded in the many combinatorial possibilities of these amino acid sequences. Every amino acid has different properties due to its characteristic side chain (fig. 2.2 a), which determines its size, charge, and polarity. The condensation of amino acids via peptide bonds formed between the carboxyl-group of one and the amino group of another amino-acid produce the long polypeptide backbones of proteins (fig. 2.2 b)). The sequence of amino acids in the backbone is characteristic for every protein and is called its primary structure (fig. 2.2 c)).

The three dimensional structure of a protein is based on the sequence of the amino acids and

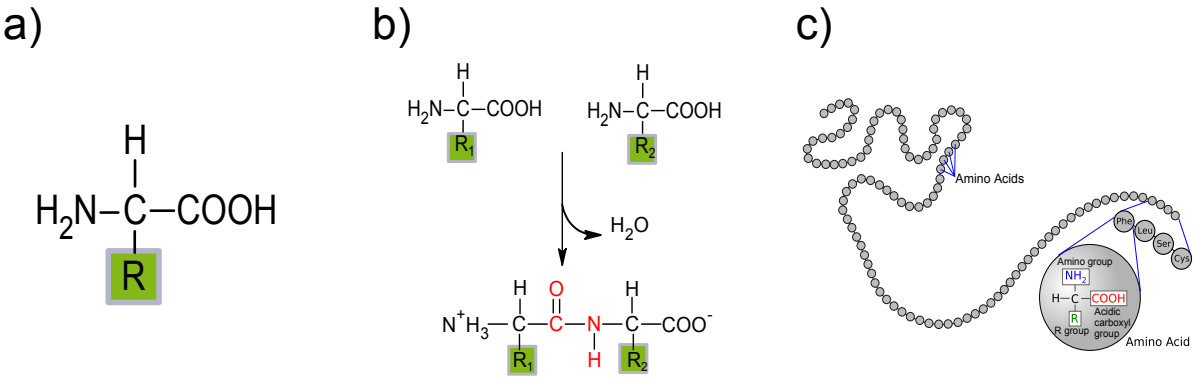

Figure 2.2: *a) A single amino acid, 'R' marks the location of the side group. b) The condensation of two amino acids. c) The resulting polypeptide chain. Picture c) adapted from [Wikimedia, 2014].*

their interactions among each other. There are different interactions involved, which cause the so-called folding of the protein:

- van der Waals interaction,
- ionic interaction,
- hydrophobic interaction,
- hydrogen bonds, and
- disulfide bonds.

The flexibility of the polypeptide chain allows many different conformations; however, one single conformation is characteristic for most proteins. Due to steric repulsion of two neighboring amino acids, the conformation of the chain is reduced to certain angles between these [Voet et al., 2005, Winter et al., 2011]. Furthermore, amino acids that are not closely located in the primary structure can interact with each other due to the properties of their side chains. The 20 different proteinogenic side chains can be classified in four basic classes, which are defined by their intramolecular interactions [Voet et al., 2005]. In fig. 2.3, the amino acids are shown, classified as polar/uncharged, nonpolar/hydrophobic, acidic, and basic.
Oppositely charged parts of the polypeptide chain attract each other and can result in closely located amino acids in the finally folded proteins. Additionally, all polar side chains are able to form hydrogen bonds with each other. Those interactions can give rise to characteristic structural elements, known as the secondary structure of the protein. The most frequent examples are the α-helix and β-sheets, which are depicted in fig. 2.4. The connecting hydrogen bonds are shown as dotted lines. The α-helix is stabilized through the hydrogen bonds formed between an amino acid side chain and its fourth neighbor of the same sequence. The β-sheet incorporates two neighboring parts of the polypeptide chain, which are located parallel or anti-parallel to each other. In rare cases, also left-handed α-helices can exist. Furthermore, even more highly ordered regions can be formed in structure proteins, like a triplet-helix in collagen [Winter et al., 2011]. Besides those highly ordered structures, interconnecting, less ordered parts of the proteins exist.

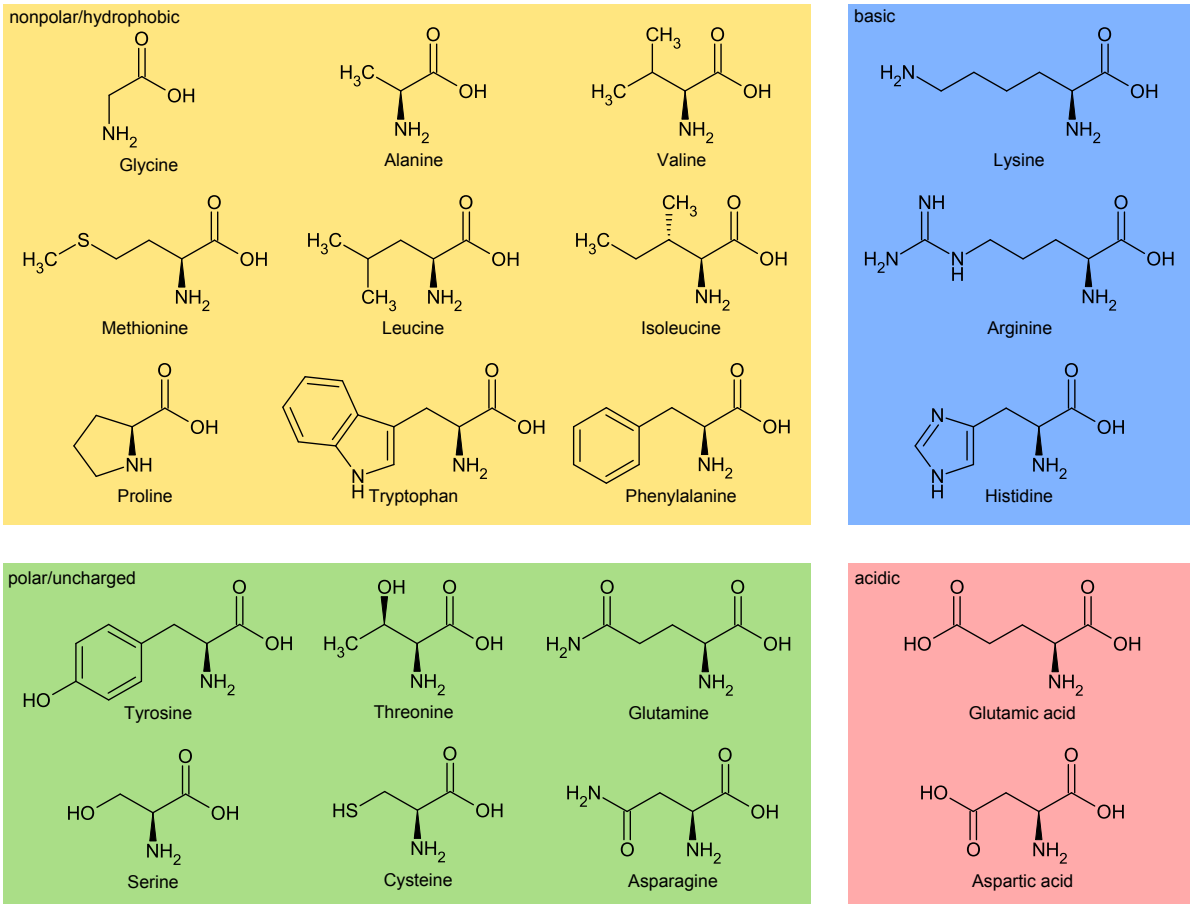

Figure 2.3: *The 20 different proteinogenic amino acids ordered corresponding to the characteristic of the side chain. Picture adapted from [Wikimedia, 2014].*

A protein natively functions in solvated form, which has direct implications on its folding. Roughly 40 % of a protein consists of nonpolar amino acids which tend to be located inside the folded protein due to the hydrophobic effect [Winter et al., 2011]. Also polar parts of the polypeptide chain can lay in the inside of the protein, forming hydrogen bonds. This results in a very compact conformation with a dense protein interior. The arrangement of the secondary structure elements and the further proteins parts are known as the tertiary structure of a protein. In the case of proteins consisting of more than one polypeptide chain, the association of those subunits is known as quartiary structure. Also incorporated metal atoms can occur in some cases [Löffler et al., 2007].

Other than the mentioned non-covalent, intramolecular interactions, also covalent interactions between side chains via so-called disulfide bonds are possible. Those can form between two cysteine side chains and are strongly involved in the stabilization of native proteins like insuline [Winter et al., 2011]. Important for this thesis is the protein lysozyme, which has four disulfide bonds incorporated [Canfield and Liu, 1965], making it very resistant against unfolding by pressure. This effect will be discussed later.

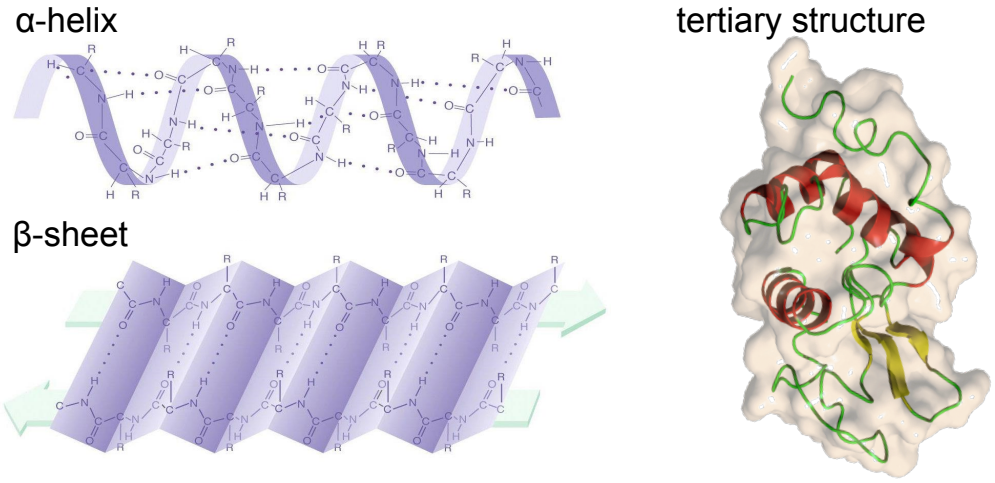

Figure 2.4: *The α-helix and β-sheet are the typical forms of secondary structure elements. Pictures adapted from [Oregon State University, 2008]. The arrangement of secondary structure elements is known as tertiary structure, shown here for the protein lysozyme. Picture adpated from [Wikimedia, 2014].*

The charged side chains of the polypeptide chain are mainly located at the surface of the protein, which has several implications. First, these amino acids can form hydrogen bonds with the surrounding water molecules, resulting in a dense water layer around the protein (see fig 2.5). Notably, the water molecules are packed much more densely at charged or polar sides, compared to nonpolar surface areas. The resulting so-called hydration shell was found to have $10-15$ % higher density compared to bulk water [Svergun et al., 1998, Merzel and Smith, 2002]. Furthermore, the charged surface parts result in an effective net charge of the protein surface, which has implications for the intermolecular protein interactions. An extended discussion of this interactions will follow in sec. 2.2.

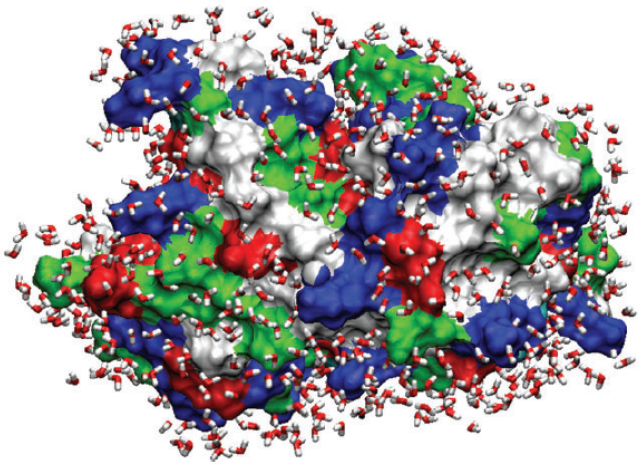

Figure 2.5: *Simulated localisation of water molecules on the surface of the protein staphylococcal nuclease (SNase). Different surface areas are marked in different colors; polar (white), charged (red, blue), and non polar (green). The water molecules are more closely packed in vincinity to hydrophilic areas. Picture taken from [Mitra et al., 2006].*

Considering the strong impact of the protein's hydration on its folding, it is clear that changes in the surrounding medium must have direct consequences on the conformation. For example, the addition of hydrophobic cosolutes like ethanol results in a destabilization of the protein structure, as the molecules can bind to the hydrophobic parts of the protein, which then are less strongly drawn to the protein's interior [Brandts and Hunt, 1967]. In general, every change in pH, temperature, or pressure, away from physiological conditions, results in a destabilization of the protein conformation. The physical processes and forces involved will be discussed in sec. 2.5.

2.2 Intermolecular interactions: DLVO theory

The forces and interactions connected to the folding of proteins can also act between different proteins, i.e., as intermolecular interactions. The two main contributions that influence the interaction potential are the Coulomb interaction caused by the surface charge of the proteins, and the van der Waals interaction. The Derjaguin-Landau-Verwey-Overbeek (DLVO) theory was independently established by Derjaguin and Landau [Derjaguin and Landau, 1941] and Verwey and Overbeek [Verwey, 1947], to describe the stability of colloidal dispersions. It models the interactions of charged colloidal particles in an implicit solvent by the combination of repulsive, long-ranged, screened Coulomb interaction and an attractive, short-ranged van der Waals interaction. Notably, the proteins are treated as spheres with an isotropic interaction potential in this description, hence neglecting the anisotropy of shape and charge distribution. Nevertheless, such idealized potentials were successfully used to model phenomena like a liquid-liquid phase separation [Rosenbaum et al., 1996, Pellicane et al., 2003, Dumetz et al., 2008].
A sketch of the different contributions is depicted in fig. 2.6. The interacting particles exhibit an effective surface net charge, which is determined by the pH of the solution. Dissolved salt ions are modeled as point like charges and form a counterion cloud around the particle surface. Therefore, the ions are able to screen partially the surface net charge of the protein and effectively decrease the repulsive interaction. In the course of scientific discussion, several extensions to the DLVO theory have been proposed in order to account for hydration forces, hydrohobic forces, water structure forces, or specific ion effects [Ninham, 1999, Boström et al., 2001, Boström et al., 2006, Dahirel and Jardat, 2010]. Anisotropic contributions were incorporated into the description by using computational methods [Quang et al., 2014], accounting for charge anisotropy of the proteins [Carlsson et al., 2001, Rosch and Errington, 2007] or modeling proteins with sticky, highly attractive patches [Bianchi et al., 2011].
Various experimental parameters were studied so far that impose different effects on the repulsive and attractive intermolecular forces. A common goal in these studies is to tune the protein interactions in order to improve protein crystallization. In fact, an exact interplay of attractive and repulsive intermolecular forces is crucial for obtaining high quality protein crystals.
Protein-protein interactions were studied as a function of protein type and concentration, pH, temperature, as well as salt concentration and type [Malfois et al., 1996, Tardieu et al., 1999, Bonneté et al., 1999, Tardieu et al., 2002, Narayanan and Liu, 2003, Zhang et al., 2007, Shukla et al.,

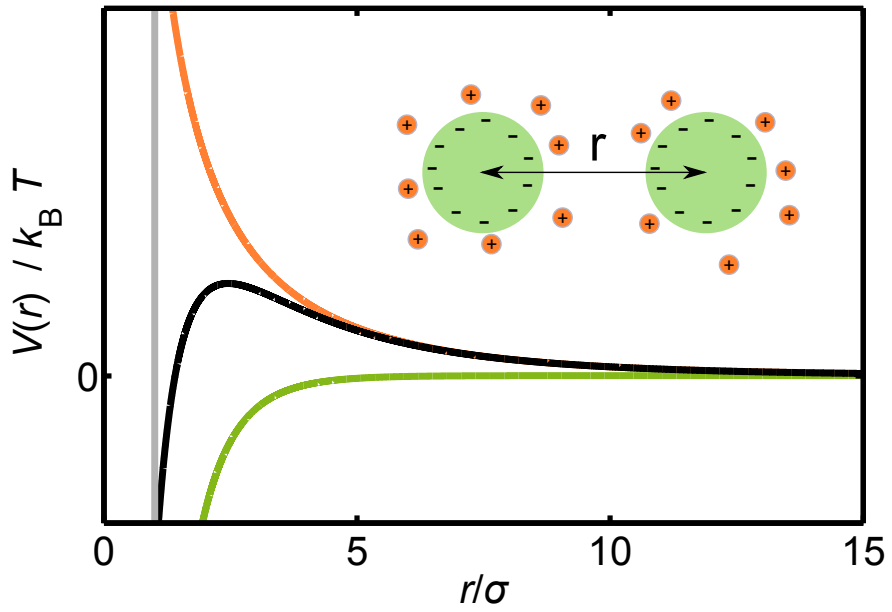

Figure 2.6: *Interaction potential as a function of separating distance r. The depicted DLVO potential (black) is given by the sum of a screened Coulomb (orange) and a van der Waals potential (green). The impenetrable surface is modeled as an infinite high potential (grey) at $r/\sigma = 1$, with σ being the diameter of the particles.*

2008a, Zhang et al., 2008, Zhang et al., 2012a], often by using small angle X-ray scattering. Furthermore, the effect of different cosolvents was included [Niebuhr and Koch, 2005, Sedgwick et al., 2007, Javid et al., 2007b]. However, the effect of pressure on the interaction potential was only studied in the strongly repulsive regime [Ortore et al., 2009, Schroer et al., 2011a, Schroer et al., 2011b, Russo et al., 2013, Schroer et al., 2012], but highly attractive interactions are of relevance for crystallization purposes. The experiments in this thesis are aimed to expand the investigation of high pressure effects to solution conditions of highly attractive protein-protein interactions.

2.3 Phase behavior of protein solutions

The phase behavior of a protein solution is directly connected to the underlying intermolecular interaction potentials. Understanding of the phase behavior of dense protein solutions is of fundamental importance in various fields of research. For example, protein aggregation and phase separation present the basic mechanisms in diseases such as sickle-cell anemia [Galkin et al., 2002], cataract [Pande et al., 2001, Wang et al., 2010], and conformational diseases such as Alzheimer's or diabetes mellitus type II [Javid et al., 2007a]. Furthermore, the study of phase separation phenomena has implications on the fundamental physical understanding of colloidal systems in general. For example, the occurrence of the so-called coffee-ring effect, found in drying colloidal dispersion, is believed to be connected to liquid-liquid phase separation [Miller et al., 2013]. In a more technological context, knowledge on the phase behavior of proteins is needed in applications such as protein crystallization, purification, and high pressure food processing [Curtis

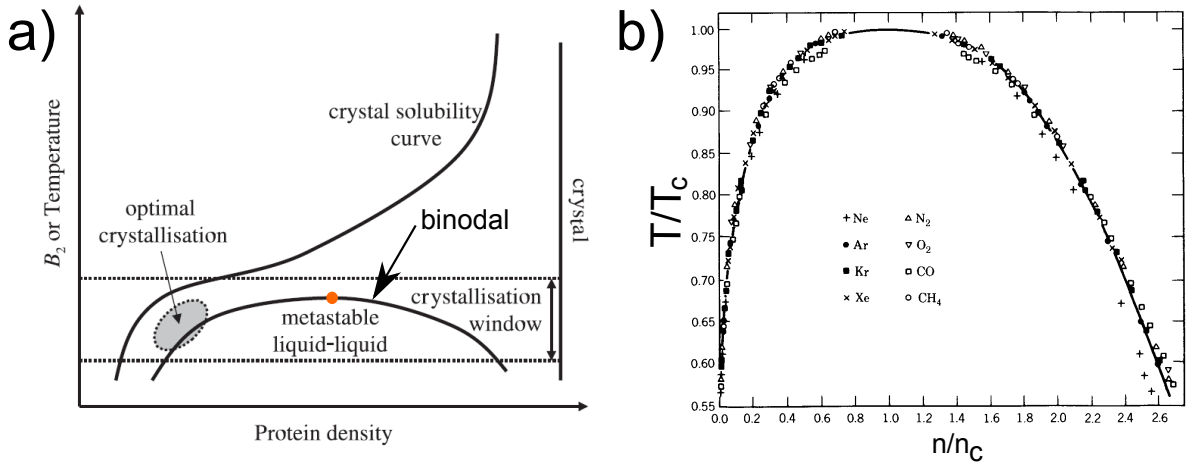

Figure 2.7: *a) Phase diagram of highly concentrated protein solutions. Below a binodal line, two coexisting protein phases form, which differ in their concentration. The optimal crystallization conditions are close to the phase separation boundary. The protein solution exhibits a critical point with the critical temperature T_c and the critical protein density (orange). Picture adapted from [Curtis and Lue, 2006]. b) Gas-liquid coexistence obtained for different substances, rescaled in terms of the critical temperature T_c and critical density n_c. The occurrence of a liquid-liquid phase separation in protein solution has similarities to the gas-liquid coexistence obtained for different one-component substances. Picture taken from [Huang, 1987].*

and Lue, 2006, Muschol and Rosenberger, 1997].

The occurrence of a metastable liquid-liquid phase separation (LLPS) region in the phase diagram of proteins has been reported, e.g., for lysozyme [Muschol and Rosenberger, 1997, Cardinaux et al., 2007], γ-crystalline [Thomson et al., 1987], and hemoglobin [Galkin et al., 2002, Chen et al., 2004]. A schematic representation is shown in fig. 2.7 a) as a function of temperature and protein concentration. Below the binodal phase separation line, two liquid protein phases coexist, which differ in their protein concentration. Small droplets of highly concentrated protein solution are formed, making the protein solution opaque for visible light. This behavior was found to be generally characteristic for colloidal systems exhibiting strong attractive interactions with a range much shorter than the size of the particles [Rosenbaum et al., 1996]. Such solution conditions are typically achieved by screening the repulsive Coulomb interaction with ions [Muschol and Rosenberger, 1997] or inducing a depletion attraction by crowding agents [Tardieu et al., 2002, Vivarès and Bonneté, 2004]. The formation of a LLPS in protein solution was studied as a function of pH, salt concentration, type of salt, and temperature [Taratuta et al., 1990, Muschol and Rosenberger, 1997, Grigsby et al., 2001, Cardinaux et al., 2007, Zhang and Cremer, 2009, Dumetz et al., 2008, Zhang et al., 2008, Zhang et al., 2012b]. Interestingly, the location where the LLPS occurs was found to foster protein crystallization [George and Wilson, 1994, Haas and Drenth, 1999, Muschol and Rosenberger, 1997]. The quantitative details of the phase diagram are controlled by the precise nature of the protein-protein interaction potential [Curtis and Lue, 2006]; for different proteins, the obtained phase diagrams can quantitatively differ. Nevertheless, a certain congruence can be found, when the phase diagram is obtained as a function of the second virial coefficient B_2 [Curtis and Lue, 2006], which will now be introduced.

The phase diagram exhibiting a critical point (fig. 2.7 a), marked orange) has distinct similarities to the liquid-gas coexistence line found in interacting, non-ideal gases. In fig. 2.7 b), the coexistence line for different one-component substances is depicted in terms of the critical temperature T_c and density n_c. The phase boundary marks conditions, where the systems are in coexistence between liquid and gas. Thus, it is possible to describe proteins dissolved in water by the thermodynamic description of such a non-ideal gas [Wills and Winzor, 2005]. The van der Waals equation includes deviations from an ideal gas

$$RT = \left(p + \frac{a}{(V/N)^2}\right)((V/N) - b), \tag{2.1}$$

with R the universal gas constant, T the temperature, p the pressure, and V the volume of the system. b is accounting for the reduced volume due to the volume of the molecules and a for corrections in the pressure of the system due to attraction between the particles. Those corrections are also needed for the description of protein solutions, where the size of the proteins and the intermolecular forces are of considerable importance.
Another representation of the equation of state in eq. 2.1 can be calculated by the virial expansion of the pressure in terms of the molecule concentration c:

$$\frac{p}{RT} = \frac{c}{M} + B_2(T)c^2 + B_3(T)c^3 + \ldots, \tag{2.2}$$

with B_i being the so-called virial coefficients and M the molecular weight of the molecule. The virial coefficients account for the intermolecular interactions between the molecules. The van der Waals equation is obtained by ending the expansion after the second order, the ideal gas equation is obtained in case of not interacting particles ($B_i = 0$).
In terms of proteins dissolved in solution, the pressure p in the description has to be replaced by the osmotic pressure of the solution Π. This gives for the virial expansion:

$$\frac{\Pi}{RT} = \frac{c_P}{M} + B_2(p, T, c_S)c_P^2 + \ldots, \tag{2.3}$$

with c_S being the salt and c_P the protein concentration in the solution. Attractive interactions between the proteins give negative B_2 values, therefore lowering the osmotic pressure of the solution. Consequently, repelling protein-protein interactions result in positive B_2 values and an increased osmotic pressure. Notably, the virial coefficients are not only a function of temperature in the case of proteins, which makes the complete thermodynamic description of protein solutions much more challenging. It has been shown in the previous section that the addition of salts has considerable influence on the protein-protein interactions and therefore also on B_2. Furthermore, the hydrostatic pressure can also be an adjustable parameter of the protein solution. A systematic investigation of the pressure dependence of $B_2(p)$ has never been done so far, but a complete thermodynamical description of protein solutions is needed, especially for the challenging task of protein crystallization. A systematic investigation of B_2 as a function of temperature and pressure as well as salt type and concentrations will be presented in chapter 5.

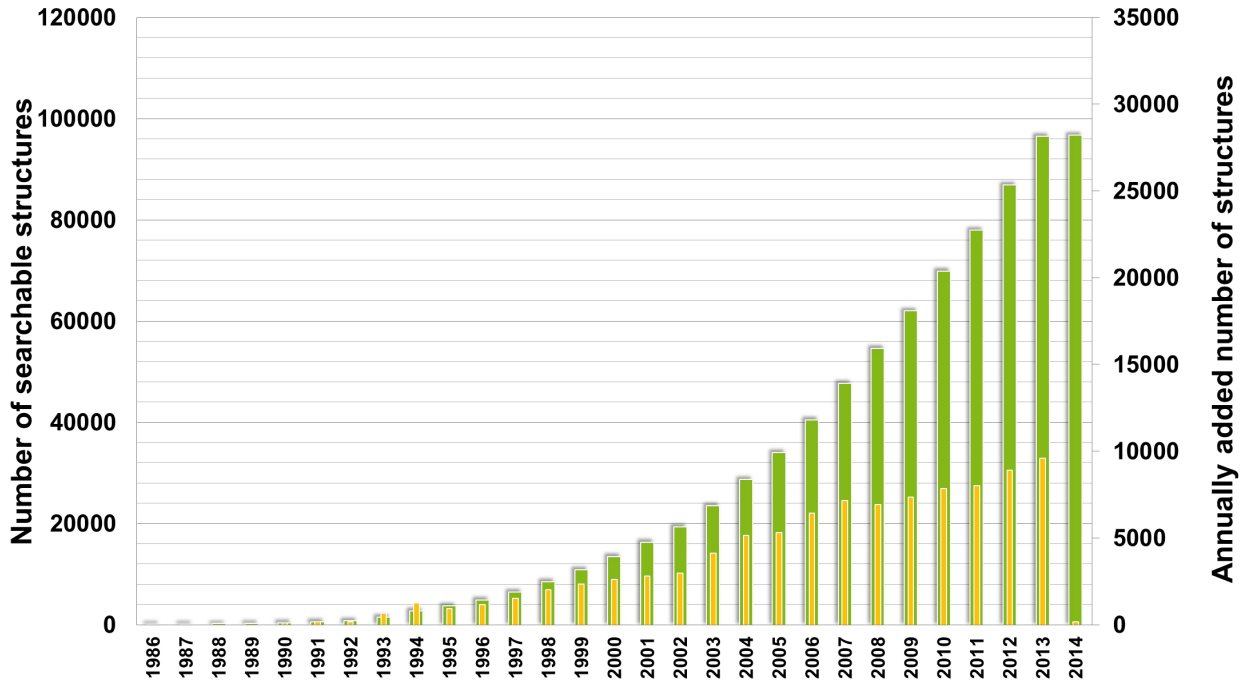

Figure 2.8: *Total number of deposited (green) and annually added (yellow) protein structures in the Protein Data Bank. Date: January 2014.*

2.4 Protein crystallization

With the advance of synchrotron radiation facilities and the increasing capability of computational data interpretation methods, the number of protein structures known with atomic resolution has increased dramatically. The structures that are deposited in the protein data bank [RCSB, 1971] as well as the number of annually added structures are shown in fig. 2.8. A nearly exponential increase can be noted until 2007, but the number of annually deposited structures has only slowly increased since. In 2013, 9600 new protein structures were deposited to the PDB. The huge need for improved investigation routines is shown by the fact that the TargetTrack [PSI, 2014] data bank currently holds more than 320000[1] targeted protein structures. The limiting step in most of the experiments has become the production of high quality protein crystals. Only such crystals can be investigated with atomic resolution. However, only a small amount of the targeted structures could be crystallized in the first place. Even today, the search for optimal crystallization conditions is usually carried out by a trial-and-error routine, i.e., empirical screening through a large field of parameter sets until suitable protein crystals are obtained [Mueller et al., 2007, Chayen and Saridakis, 2008, Giegé, 2013]. This procedure certainly presents a bottleneck for current research. Thus, further tools for protein crystallization are constantly needed.

Protein crytallization routines were investigated at high pressure conditions in a series of studies on various proteins, such as subtilisin [Webb et al., 1999, Waghmare et al., 2000], glucose isomerase [Suzuki et al., 2002b, Suzuki et al., 2005], thaumatin [Kadri et al., 2003, Kadri et al., 2005], and

[1] Date: January 2014

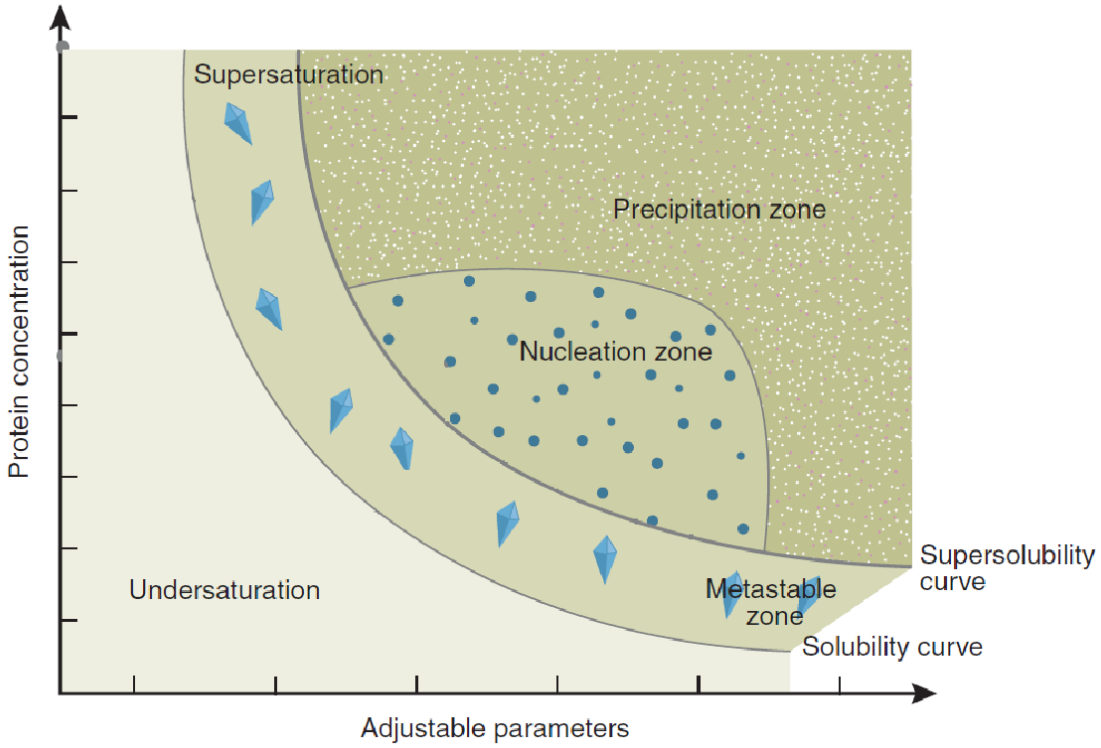

Figure 2.9: *Schematic phase diagram of protein crystallization. The task is to tune the protein solution from the undersaturated state into the so-called nucleation zone. The adjustable parameter of the protein system will be introduced in the following sections. Picture adapted from [Chayen and Saridakis, 2008].*

lysozyme [Gross and Jaenicke, 1991, Gross and Jaenicke, 1993, Schall et al., 1994, Saikumar et al., 1995, Lorber et al., 1996, Takano et al., 1997, Sazaki et al., 1999, Suzuki et al., 2002a, Nagatoshi et al., 2003]. These studies investigated the solubility, nucleation, and growth rates of protein crystals under pressure, yielding diverse results for different proteins, however. Less attention was directed towards the resulting protein crystal structure and quality [Kadri et al., 2005, Lorber et al., 1996] as well as towards the underlying intermolecular interaction potentials.

In this context, knowledge on the effect of increasing hydrostatic pressure on the phase diagram as well as the underlying intermolecular interactions is needed to explore the possibility of improving crystallization processes by pressure modulation. The protein interactions and the resulting phases behavior can be tuned by several different parameters [Giegé, 2013]. A principle phase diagram is sketched in fig. 2.9 as a function of protein concentration and an adjustable parameter. Commonly used parameters in crystallization routines are temperature or the concentration of different salts and crowders. The exact knowledge on the interaction strength as a function of the applied parameter is crucial as the protein solution has to be tuned from outside the solubility curve (see fig. 2.7 a) and 2.9) into the so-called nucleation zone (fig. 2.9). This presents a very challenging task as too attractive interactions result in unordered precipitation (precipitation zone) and too repulsive interactions in completely solvated proteins (undersaturation). No systematic studies on the intermolecular interactions of proteins as a function of pressure have been made

in this highly attractive regime yet.

2.5 High pressure effects on protein solutions

Several parameters can be used to influence the intermolecular interactions of proteins. However, all changes in the aqueous environment can also have potential denaturating effects on proteins. The unfolding of a protein is closely related to the initial folding from the single, unfolded polypeptide chain. The mostly accepted model for describing protein folding is using an energy landscape (see fig. 2.10), which is predicting a funnel-like shape of the free energy as function of the protein's conformation [Bryngelson et al., 1995]. Consequently, the folding can be understood as a reduction of the configuration space by a decrease in the total free energy. Therefore, the folding kinetics of a protein are directly connected to the roughness of the corresponding energy landscape [Dill and Chan, 1997].

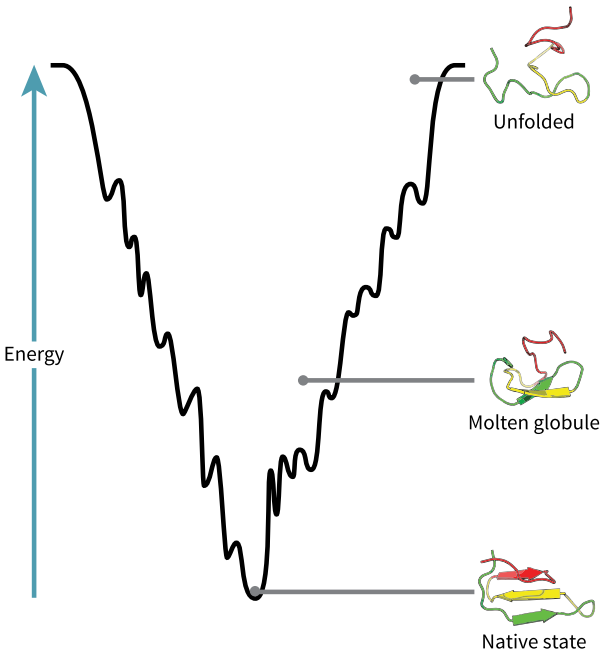

Figure 2.10: *Sketch of folding funnel of proteins. The intermediate state is represented as molten globule. Picture adapted from [Wikimedia, 2014].*

For small single domain proteins, the energy landscape can have a relatively smooth surface without local minima, corresponding to a direct folding without characteristic intermediate states. In experiments, the obtained folding and unfolding process can typically be described by a single exponential decay. In the case of multi domain proteins, the energy landscape has a rougher surface with several local minima, corresponding to intermediate folding states that the protein can adopt during the folding process. In fig. 2.11, the different possible conformations are depicted. Notably, the unfolding due to denaturating conditions can roughly be viewed as the same process with opposite direction.

These different states of the protein can be described with two simplistic conformations, the molten globule and the random coil. The latter corresponds to a completely unfolded protein, where secondary and tertiary structure elements are missing and the only structuring elements are the peptide bonds in the backbone. In contrast, the molten globule still has a certain compact form with secondary structure elements. As the tertiary structuring of these elements is missing, the conformation is much more flexible than the native form. A further description of this state is known as swollen protein because much more parts of the protein are hydrated. This structure can be assigned to the intermediate states in proteins synthesis or destabilized protein

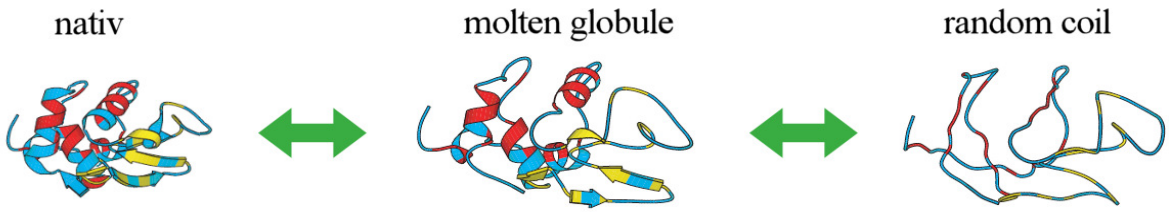

Figure 2.11: *Sketches of the different conformations: native, molten globule, and random coil for the example of lysozyme. Picture taken from [Krywka, 2008].*

in mild denaturating conditions. In principle, these different conformations can be determined in a SAXS experiment. The different influences that can induce such an unfolding of the protein are described in the following paragraphs.

One very effective way to unfold proteins is the heat denaturation as an increase of several 10 °C can for example already break up the hydrogen bonds to the solvent [Koizumi et al., 2007]. This directly affects the secondary structure and can lead to a complete unfolding of the protein. On the other hand, also cold denaturation can have a destabilizing effect. However, the necessary temperatures can be below the freezing point of water and are therefore harder to achieve experimentally.

Every protein has its isoelectric point, i.e., the solution pH where the surface net charge is vanishing. Drastic changes to lower pH values can induce the acid denaturation as the number of surface charges increases. The resulting Coulomb repulsion can cause an unfolding of the protein [Dill, 1990]. The same mechanism can cause unfolding at very high pH values.

Increased pressure presents a very gentle disturbance to the protein conformation. An increase in pressure results in an increasing density of the pressurized system. In contrast, changes in temperature alter the density as well as the internal energy of the system [Silva et al., 2001]. Furthermore, pressure can have an even stabilizing effect on hydrogen bond formation. In fact, the secondary structure of a protein is not affected by pressure perturbations below 10 kbar [Boonyaratanakornkit et al., 2002, Meersman et al., 2006]. Typically, a smaller radius of gyration for pressure unfolded proteins than in the temperature unfolded state is obtained [Panick et al., 1998, Schroer et al., 2010]. Furthermore, protein denaturation with pressure has been found to be completely reversible [Perrett and Zhou, 2002, Winter et al., 2011, Heremans and Smeller, 1998, Silva et al., 2001, Mishra and Winter, 2008], in contrast to temperature denaturation. In the case of pressure denaturation, typical values for unfolding obtained in experiments were between 1 and 7 kbar [Smeller, 2002, Winter et al., 2011], depending strongly on the used protein. Pressure effects on chemical systems generally follow LeChatelier's principle, i.e., an increase in pressure leads to a shift of the chemical equilibrium of the system to the state with the smaller overall volume. In terms of protein unfolding, volumetric properties like hydrophobic packing or the hydration of different amino acids are affected by a pressure increase. The important characteristic is the difference in volume between the unfolded and the native, folded state, known as the volume of unfolding ΔV. In general, this quantity is small ($< 1\%$) and negative [Royer, 2002], meaning that the unfolded protein occupies less space. Here, collapses of internal cav-

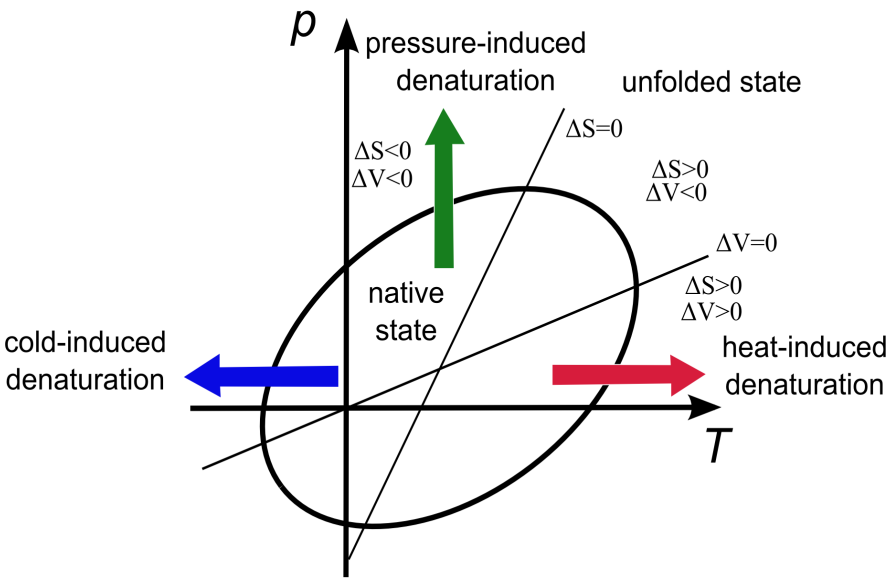

Figure 2.12: *A typical elliptically shaped pressure-temperature stability diagram. The protein is in its native conformation for thermodynamic parameters inside the phase boundary, corresponding to $\Delta G(p,T) > 0$. Sketch taken from [Schroer, 2011].*

ities, void volumes, and packing defects are the main contributions [Frye et al., 1996, Royer, 2002, Roche et al., 2013]. Furthermore, the effect of pressure typically results in a penetration of water molecules into the protein's interior, leading to a partially unfolded, swollen, and increasingly hydrated conformation [Meersman et al., 2006]. Because of the increased hydration of the unfolded protein, the volume of unfolding is negative.

The combined influence of temperature and pressure on protein stability can be treated in terms of the Gibbs free energy $G(p,T)$. In the case of proteins, where the unfolding can be described by a simple two state model[2], the so-called Hawley equation [Hawley, 1971] describes the difference $\Delta G(p,T)$ between the folded and the unfolded state as

$$\begin{aligned}\Delta G(p,T) = \Delta G_0 - \Delta S_0(T-T_0) - \Delta C_p\left[(T-T_0) - T\ln(T/T_0)\right] \\ + \Delta V_0(p-p_0) + \frac{\Delta\tilde{\kappa}}{2}(p-p_0)^2 + \Delta\tilde{\alpha}(p-p_0)(T-T_0),\end{aligned} \tag{2.4}$$

with S being the entropy, C_p the heat capacity, $\tilde{\kappa} = (\partial V/\partial p)_T$ the compressibility factor, and $\tilde{\alpha} = (\partial V/\partial T)_p$ the thermal expansion factor. The equilibrium between unfolded and folded state, $\Delta G(p,T) = 0$, marks the boundary of the native state in the temperature-pressure phase diagram [Meersman et al., 2013, Heremans and Smeller, 1998]. By expanding the term in square brackets in eq. 2.4, one obtains the elliptic shape of the transition line for $\Delta G(p,T) = 0$, shown in fig. 2.12. For thermodynamic parameters lying inside the elliptic contour the protein has its native conformation ($\Delta G > 0$), outside the protein is unfolded ($\Delta G < 0$).

From the course of the phase boundary, some interesting observations can be made. For example, increasing pressure can have a stabilizing effect near the denaturating temperature. The exact

[2] This is the case for proteins without characteristic intermediate states.

location of the phase boundary, however, is strongly dependent on the protein's structure as well as the solution conditions. The addition of cosolvents to the solution can markedly change the location of the phase boundary. This will be discussed in sec. 2.7.

Studies on intermolecular interactions as a function of pressure and temperature have often been performed by tuning the solution conditions out of the stability region of the proteins, where phenomena like aggregation and fibrillation can occur as consequence to the unfolding [Smeller, 2002, Grudzielanek et al., 2006]. It was found that pressure can have a dissociating influence on protein aggregates [Gorovits and Horowitz, 1998, Foguel et al., 1999, St. John et al., 1999]. In the framework of protein crystallization however, the response to non-denaturating solution conditions is studied.

Still, changes in the intermolecular interactions can occur due to changes of the aqueous environment, but the interaction behavior can markedly be different as the proteins stay in their native conformation. A dissociation effect on β-lactoglobulin oligomers was found for pressures up to 2 kbar [Gebhardt et al., 2012], which is in line with an increasing repulsive interaction due to pressure increase [Russo et al., 2013]. This increasing repulsiveness with pressure was also found for lysozyme [Ortore et al., 2009], but for higher pressures this effect is reversed [Schroer et al., 2011a]. This non-linear pressure dependence is associated to structural changes in the second coordination shell of water, starting roughly at a pressure of 2 kbar. This effect will be discussed in the next section. It will be investigated in this thesis, if the resulting non-linear pressure dependence is still present in strongly attractive solution conditions of high ionic strength.

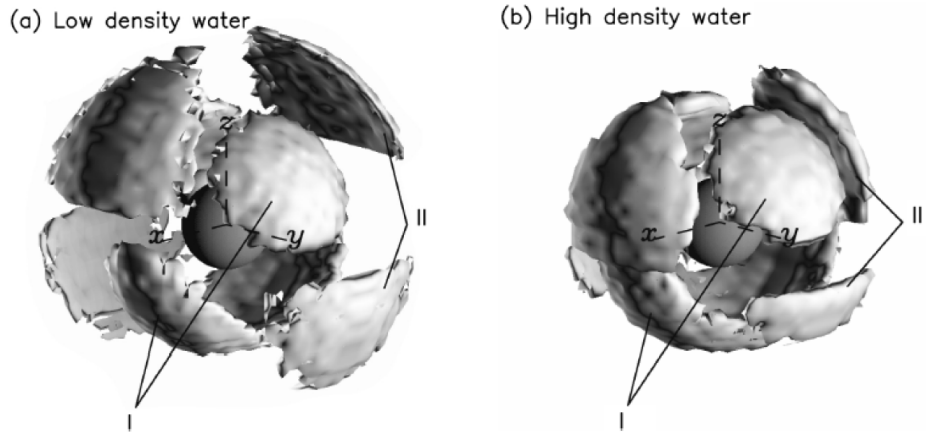

Figure 2.13: *Spatial density function for water of low (a) and high (b) density. A closer location of the second hydration shell can be seen for high density water. Picture adapted from [Soper and Ricci, 2000].*

2.6 High pressure effects on solvation

Notably, changes in temperature, pressure, pH, and cosolvent concentration mainly change the properties of the solvent and not of the protein. In order to understand the changing hydrational properties of macromolecules under high pressure conditions, one has to consider that those are closely linked to the changes in the local water structure itself. It has to be mentioned that even at atmospheric conditions the local water structure is still a subject of scientific debate [Ball, 2008, Nilsson and Pettersson, 2011], as it presents many unusual properties, which are assigned to the strong influence of constantly forming and breaking hydrogen bonds.

This results in unusual characteristics under increased pressure, such as the lowest temperature were water is liquid was found to be $-22\,^{\circ}\mathrm{C}$ at 2100 bar. Different transport properties of water also show a marked pressure dependence in this pressure region, with a maximum of the diffusion coefficient at 2 kbar [Ludwig, 2001] and a minimum of the shear viscosity between $1-2$ kbar [Debenedetti, 2003].

This behavior comes in hand with structural changes, namely a collapse of the second hydration shell at pressures above 2 kbar [Okhulkov et al., 1994, Soper and Ricci, 2000]. The structural representations, obtained from pressure dependent neutron scattering experiments, of the first (I) and second (II) hydration shell around a central water molecule are shown in fig. 2.13 for low (a) and high (b) density water [Soper and Ricci, 2000]. Starting at 2 kbar, the increasing pressure results in an increasing population of the high density conformation of water and therefore a closer location of the second hydration shell in respect to the central water molecule, almost at the same distance as the first hydration shell.

As a consequence of the higher average number of water molecules surrounding another water molecule due to increasing pressure, the average binding energy decreases [Sciortino et al., 1991]. This reduces the cost of inserting a water molecule into unfavorable non-polar locations [Meersman et al., 2013], pointing out an effective decrease of the hydrophobic effect at higher pressure. Computer simulations on the pair potential of hydrophobic methane molecules in water support

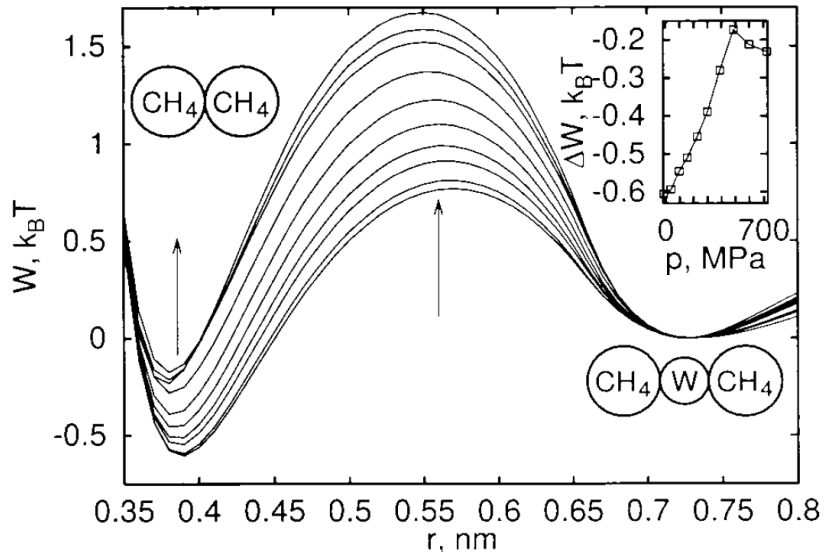

Figure 2.14: *Potential of mean force for methane molecules as a function of separating distance. The minimum of the water molecule separated distance stays constant as a function of pressure whereas the direct contact minimum is strongly destabilized. Changes due to increasing pressure are depicted by arrows. Picture taken from [Hummer et al., 1998].*

this supposition [Hummer et al., 1998, Ghosh et al., 2001]. The potential of mean force[3] for a pair of methane molecules is depicted in fig. 2.14. With increasing pressure, the direct contact minimum is destabilized compared to the solvent separated minimum, owing to a preferred solvation of the hydrophobic molecules. A similar behavior has also been found for protein oligomers [Gebhardt et al., 2012]. In general, it can be stated that pressure increases the hydration of hydrophobic and polar moieties [Meersman et al., 2013], which can result in the aforementioned swollen conformation of proteins, but can also change markedly the intermolecular interactions of solvated molecules.

2.7 Osmolytes and salts

The effective solution conditions cannot only be influenced by changes in temperature and pressure, but also the addition of further molecules or cosolvents can alter stability and interactions of proteins significantly. Those can be small osmolytes, salts, or larger polymers, so-called crowders. In fact, the cytoplasm of the cell is a highly crowded solution with a complex variety of different salts and osmolytes [Daniel et al., 2006].

Cosolvents are generally classified into kosmotropic cosolvents, which have a stabilizing effect on proteins, and chaotropic cosolvents, which destabilize the native protein conformation. Well studied examples are urea as denaturating agent and trimethylamine-*N*-oxide (TMAO) or glycerol as kosmotropic cosolutes.

[3] The potential of mean force (PMF) is defined as the potential between two particles in a systems that results as an average force over all the possible configurations.

The microscopic working mechanisms that cause the markedly different behaviors of those cosolutes are still subject to large efforts in research. Simulations suggest that TMAO increases the number of strong hydrogen bonds of the water structure, so that a direct interaction between the protein and the osmolyte is disfavored in comparison with the surrounding water [Zou et al., 2002, Bennion and Daggett, 2004, Street et al., 2006]. This depletion causes the trend to reduce the interaction interface and therefore the native protein conformation is favored. Notably, it was shown that the kosmotropic effect of TMAO is able to counteract the denaturating influence of pressure or urea on the conformation of SNase [Krywka et al., 2008].
Interestingly, similar characteristics were found in the pressure dependence of the protein-protein interaction potential of lysozyme. TMAO shifts the minimum of the before described non-linear pressure dependence to higher pressure values, indicating a stabilizing effect on the water structure against pressure perturbation [Schroer et al., 2011b]. Additionally, the canceling effect of TMAO and urea in a ration of 1 : 2 has been found in the pressure dependence of the interaction potential.

A ranking from kosmotropic to chaotropic characteristics can also be found for different anions and cations. The empirical Hofmeister series describes the minimal concentration required of a certain salt to precipitate a given protein from aqueous solution and was found by Franz Hofmeister over 125 years ago [Hofmeister, 1888, Kunz et al., 2004]. Notably, the precipitation properties of salts strongly depend on the anion and cation type. This empirical ranking was established in several further examples since, proving the remarkable universality of those specific ion effects [Bénas et al., 2002, Collins, 2004, Curtis and Lue, 2006, Zhang and Cremer, 2009]. Some cations and anions are depicted in fig. 2.15, ranked in accordance to their kosmotropic or chaotropic properties.
For example, an often used salt to unfold proteins is guanidinium chloride (CH_6ClN_3), kosmotropic properties are known for phosphate and sulphate anions. Interestingly, the influence of anions is in general much stronger compared to cations. Although the molecular origin of the Hofmeister effect is subject to large efforts in research in recent years, a detailed understanding of the interplay between the ions, water molecules, and the hydrated biomacromolecules is still missing [Omta et al., 2003, Batchelor et al., 2004, Zhang and Cremer, 2006, Smith et al., 2007, Zhang and Cremer, 2010, Paschek and Ludwig, 2011]. Interpretations on the molecular level are often referring to the structure making and structure breaking properties of the ions. Small cations and anions with a high charge density are considered as kosmotropic ions, as they are thought to reinforce the H-bond network of water and therefore are named structure makers. On the other hand, large ions are associated with chaotropic properties for being structure breakers that disturb the water structure. The exact interplay between ion and proteins, i.e. directly or indirectly via influences on the water structure are heavily discussed. To shed light into this topic, high pressure studies are crucial as they permit to directly disturb the local water structure.
Only few studies addressed the influence of ions on the water structure under high pressure conditions, mainly studying pressures above the range considered in this thesis. A discussion together

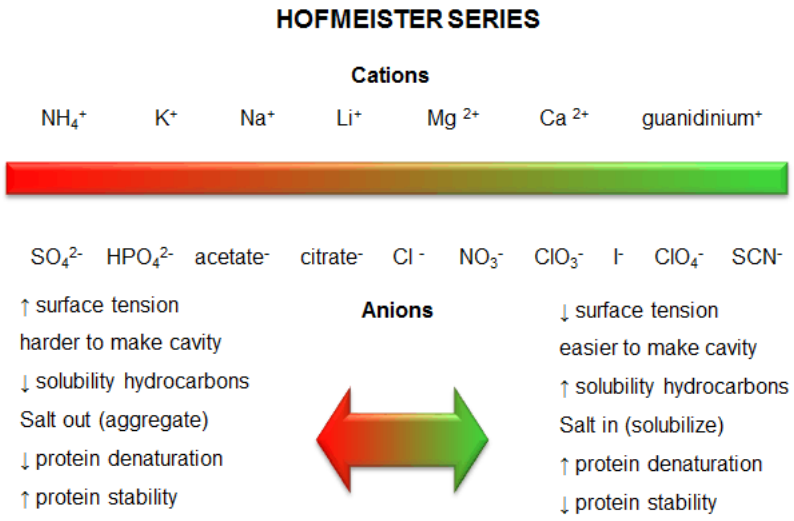

Figure 2.15: *Schematic representation of the Hofmeister series for different cations and anions. Characteristic properties for kosmotropic ions are listed on the left hand side, chaotropic properties on the right hand side. Picture adapated from [Jakubowski, 2014].*

with the results obtained in this thesis will follow in sec. 5.5. The influence of different anions on the pressure dependence of the protein-protein interactions is unknown and will be investigated in this work.

3 Small Angle X-ray Scattering

Since the first theoretical description of X-ray scattering at small angles [Guinier, 1939, Guinier and Fournet, 1955], SAXS has become a widely used technique. A development which has been strongly facilitated by the progress of high flux SAXS beamlines at synchrotron light sources. Due to the small scattering angle in the experiment ($\leq 5°$), structures larger than the wavelength of the used radiation are probed. Typically length scales of $1 - 100$ nm and in USAXS (Ultra small angle X-ray scattering) geometry even larger system lengths are accessible. The basic principle is that electron density inhomogeneities on the considered length scales give rise to X-ray scattering at small angles. Those inhomogeneities can be proteins or nanoparticles in solution as well as inclusions in porous materials. From the scattered intensity recorded as a function of the scattering angle, several structural quantities like size, shape, or polydispersity of the scattering entity can be obtained.

In case of SAXS on proteins, one special advantage is the investigation without the preproduction of protein crystals. The proteins can be handled and studied in solution, more similar to their *in vivo* environment. Nevertheless, the SAXS signal from such a disordered arrangement of macromolecules gives also a less detailed, so-called low resolution structure of the proteins. The possibility of obtaining these structural information from the scattering signal will be discussed in sec. 3.2.

A further important characteristic of SAXS, on which will be mainly focused in this work, is the possibility of investigating the intermolecular interactions of proteins in solution. The understanding and controlled tuning of these interaction potentials is the groundwork for protein crystallization and further bio-technological applications. Sec. 3.3 deals with the extraction of characteristic quantities of the protein interactions from the scattering patterns and how the inherent structure factor can be calculated theoretically.

The outline of the theoretical description of small angle scattering is based on [Glatter and Kratky, 1982], [Feigin and Svergun, 1987], [Als-Nielsen and McMorrow, 2001], [Lindner and Zemb, 2002], and [Schroer, 2011].

3.1 Fundamentals of small angle X-ray scattering

First, the typical scattering geometry of a SAXS experiment is described (fig. 3.1). A plane and monochromatic electromagnetic wave, characterized by the wave vector $\vec{k}_0$, is scattered at the

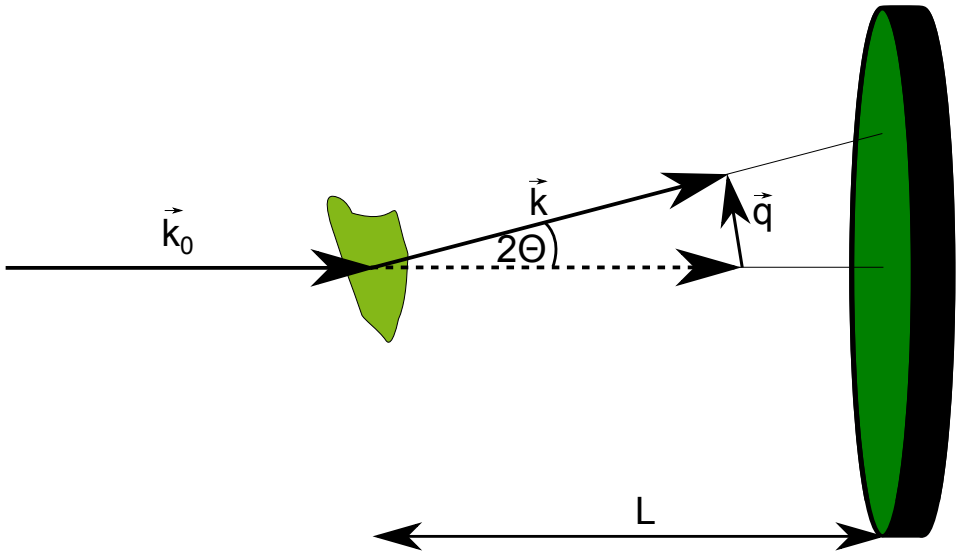

Figure 3.1: *Scattering geometry of a small angle X-ray scattering experiment [Möller, 2010]*

.

sample. The experimental observable is the scattered intensity at a certain point on the detector. The intensity is measured as a function of the wave vector transfer $\vec{q}$, which is defined as

$$\vec{q} = \vec{k} - \vec{k}_0, \tag{3.1}$$

with $\vec{k}$ being the wave vector of the scattered wave. As only elastic scattering contributions are considered, the wavelengths λ of incoming and scattered waves are the same:

$$\left|\vec{k}\right| = \left|\vec{k}_0\right| = \frac{2\pi}{\lambda}. \tag{3.2}$$

In the case of isotropic scattering samples, the wave vector transfer reduces to a function of the scattering angle 2Θ:

$$q = \frac{4\pi}{\lambda} \sin(2\Theta/2). \tag{3.3}$$

From the scattered intensity as a function of q, different structural information can be obtained. In the following, the scattering of X-rays from single electrons to complex particles will be described.

3.1.1 Scattering from a free electron

The interaction of an electron in the sample with the incoming X-ray can be calculated in a classical description, with the electron being forced to vibrate when placed in the alternating electric field of the incident X-ray beam [Als-Nielsen and McMorrow, 2001]. It can be assumed as a free electron, so that it acts as a small dipole. The ratio between incident intensity I_0 and scattered intensity I can than be calculated in dipole approximation by the Thomson scattering

formula [Als-Nielsen and McMorrow, 2001]

$$\frac{I}{I_0} = \left(\frac{e^2}{4\pi\epsilon_0 mc^2}\right)^2 \cdot \frac{1}{L^2} \cdot \frac{(1+\cos^2(2\Theta))}{2} \tag{3.4}$$

$$= \frac{r_0^2}{L^2} \cdot \Pi(2\Theta). \tag{3.5}$$

Here, e is the elementary charge, m the mass of the electron, ϵ_0 the vacuum permittivity, c the speed of light, and L the distance between the electron and the point of detection. The constants are combined to the classic electron radius $r_0 = 2.82 \cdot 10^{-5}$ Å. The polarization factor $\Pi(2\Theta)$ can be neglected in the case of small angle scattering.

The scattering from a single atom however, is a function of wave vector transfer $\vec{q}$ and the energy E of the radiation and can be calculated as [James, 1967]:

$$f(\vec{q}, E) = f_0(\vec{q}) + f'(E) + i \cdot f''(E). \tag{3.6}$$

Here, $f'(E)$ and $f''(E)$ describe the dispersion correction and the absorption of the X-rays. Both contributions are element specific and energy dependent, but have no dependence on $\vec{q}$, as their behavior is dominated by tightly bound inner-shell atoms [Als-Nielsen and McMorrow, 2001]. The imaginary part $f''(E)$ can be calculated from the absorption cross-section [Schurtenberger, 2002] and both contributions are related to each other by the Kramers-Kronig relation [Stuhrmann, 1982]. As the beam energy in a typical SAXS experiment is unchanged, these two contributions are constants. However, they offer the opportunity of changing the scattering contrast of certain elements in the sample by varying the X-ray energy as the two terms are strongly dependent on the beam energy near the absorption edge of the atom. This feature is used in anomalous small angle X-ray scattering (ASAXS) experiments.
The form factor of the atom, $f_0(\vec{q})$, is calculated as the Fourier transform of the electron density of the corresponding atom. At small angles, the atom form factor is proportional to the total electron number of the atom and is equal to $r_0 Z$ [Schurtenberger, 2002].

3.1.2 Scattering from a single particle

The next build up is the spatial arrangement of a certain number of atoms to a particle, like for example a small molecule, a nanoparticle, or a protein. The spatial arrangement of the electrons will be characterized by a charge distribution $\rho(\vec{r})$. The description of a particle by a continuous electron distribution is valid for particles sizes much larger than internal structural inhomogeneities [Porod, 1982]. As described before, the impingement of the X-ray wave with wave vector $\vec{k}_0$ and electrical field strength E_0 generates the emission of secondary waves from the sample. The

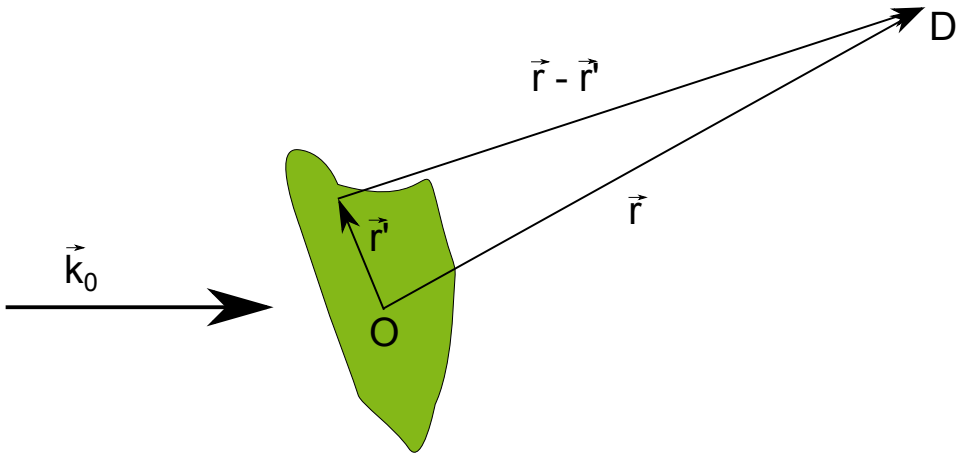

Figure 3.2: *Schematic drawing of the scattering geometry to calculate the scattering from a single particle. [Möller, 2010]*

resulting wave can be calculated in the first Born approximation [Lindner, 2002], as

$$E(\vec{r}) = E_0 \cdot \exp(i\vec{k}_0\vec{r}) + E_0 \cdot \exp(i\vec{k}_0\vec{r})/r \cdot r_0 \cdot \int_{Vol} \rho(\vec{r'}) \exp(i\vec{q}\vec{r'})\ \mathrm{d}^3r'. \tag{3.7}$$

A corresponding sketch can be found in fig. 3.2. Here, some approximations have to be made. First, the distance between the sample and the point of detection has to be much larger than the size of the sample system. This is known as far field approximation. Furthermore, the interaction between the incident X-ray wave and the sample is weak, so that only single scattering events have to be considered.

The result can then be described by the sum of two contributions. The first term of the relation presents the not with the sample interacting, plane wave. This primary beam will be removed in the experiment by a beamstop, see sec. 4.2. The second term corresponds to the emitted secondary waves from the sample. Here, every infinitesimal volume element d^3r' is source of a spherical wave, its amplitude is determined by the electron density $\rho(\vec{r'})$. As every volume element of the sample is a source of secondary waves, interference between the waves will occur. The second term in eq. 3.7 has the form of a Fourier transform of the electron density distribution. Therefore, the so-called scattering amplitude is defined as [Guinier and Fournet, 1955, Porod, 1982]:

$$\boxed{A(\vec{q}) = r_0 \int_{Vol} \rho(\vec{r'}) \exp(i\vec{q}\vec{r'})\ \mathrm{d}^3r'.} \tag{3.8}$$

With this formulation, the differential scattering cross section is calculated as

$$\frac{d\sigma}{d\Omega}(\vec{q}) = A(\vec{q}) \cdot A^*(\vec{q}), \tag{3.9}$$

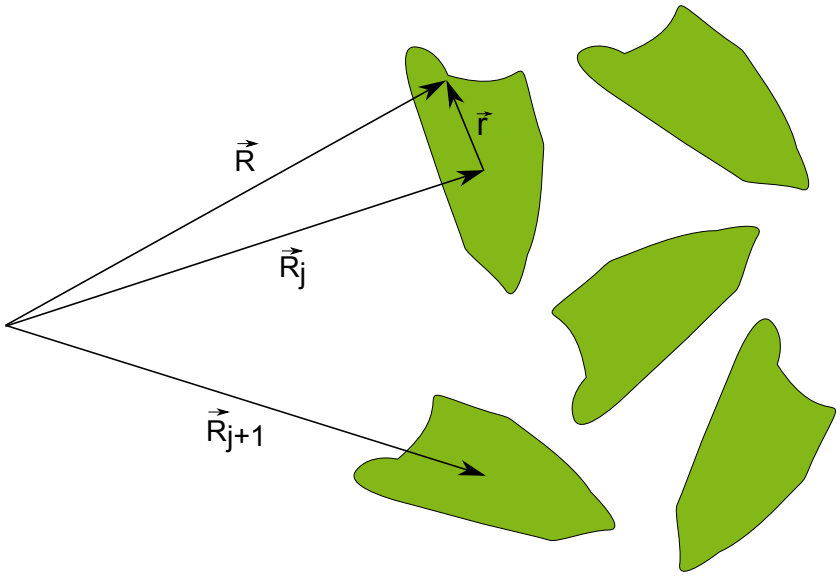

Figure 3.3: *Schematic drawing of the vectors used to calculate the scattering from an ensemble of many particles.*

from which the scattered intensity follows:

$$I(\vec{q}) = I_0 \frac{1}{L^2} \frac{d\sigma}{d\Omega}(\vec{q}). \tag{3.10}$$

The differential scattering cross section is defined as the fraction of photons scattered in the angle element $d\Omega$. $A^*(\vec{q})$ is the complex conjugated of the scattering amplitude and in accordance $I_0 = E_0^2$.

3.1.3 Scattering from an assembly of particles

The next step is to consider the scattering of an ensemble of many particles, as it is the case for example in a solution of proteins. The description starts from the calculation of the scattering amplitude (eq. 3.8), which is the Fourier transform of the system's electron density. Considering a system of N particles within a sample volume V_p, the position of the j-th particle is given by $\vec{R}_j$ and every single particle is described by its electron density $\rho_j^{(P)}(\vec{r})$. A sketch of the description can be found in fig. 3.3. The overall electron density of the system is than described by:

$$\rho(\vec{R}) = \sum_{j=1}^{N} \rho_j^{(P)}(\vec{R} - \vec{R}_j). \tag{3.11}$$

With this, the differential scattering cross section is given as

$$\frac{d\sigma}{d\Omega} = r_0^2 \left\{ \sum_{j=1}^{N} \exp(i\vec{q}\cdot\vec{R}_j) \int_{V_p} \rho_j^{(P)}(\vec{r}) \exp(i\vec{q}\cdot\vec{r})\ \mathrm{d}^3 r \right\} \cdot \left\{ \sum_{k=1}^{N} \exp(-i\vec{q}\cdot\vec{R}_k) \int_{V_p} \rho_k^{(P)}(\vec{r}') \exp(-i\vec{q}\cdot\vec{r}')\ \mathrm{d}^3 r' \right\}$$

$$= r_0^2 \sum_{j,k=1}^{N} \exp(i\vec{q}\cdot(\vec{R}_j - \vec{R}_k)) \int_{V_p}\int_{V_p} \rho_j^{(p)}(\vec{r})\rho_k^{(p)}(\vec{r}') \exp(i\vec{q}\cdot(\vec{r}-\vec{r}'))\ \mathrm{d}^3 r\ \mathrm{d}^3 r'. \tag{3.12}$$

Two cases can now be distinguished. First, terms of the double sum with the same index ($j = k$). These terms correspond to scattering contributions from only one particle. The other terms ($j \neq k$) describe scattering contributions from two different particles. These are not only a function of the electron density of the two particles but also of the distance between them. Therefore, particle-particle interactions affect these terms. Thus, the formula of the scattering cross section is decomposed into this two contributions

$$\frac{d\sigma}{d\Omega}(\vec{q}) = r_0^2 \left\{ \sum_{j=1}^{N} \left|F_j(\vec{q})\right|^2 + \sum_{j=1}^{N}\sum_{k\neq j}^{N} F_j(\vec{q}) \cdot F_k^*(\vec{q}) \cdot \exp(i\vec{q}(\vec{R}_j - \vec{R}_k)) \right\}, \tag{3.13}$$

with the form amplitude of the j-th particle

$$\boxed{F_j(\vec{q}) = \int_{V_p} \rho_j^{(p)}(\vec{r}) \exp(i\vec{q}\cdot\vec{r})\ \mathrm{d}^3 r.} \tag{3.14}$$

Up to now, scattering of a static sample systems was considered. However, particles in solution are diffusing, so that the scattered intensity is changing in time and the average over many configurations is measured [Spalla, 2002]. For these systems ergodicity is assumed, i.e. there is no difference between temporal reorientation of a single particle and different orientations of many particles [Spalla, 2002]. To further simplify the description, only identical particles are treated, which differ just in their orientation and spatial location. Therefore, the differential cross section is calculated, statistically averaged over all orientations:

$$\frac{d\sigma}{d\Omega}(q) = \left\langle \frac{d\sigma}{d\Omega}(\vec{q}) \right\rangle_{\Omega}. \tag{3.15}$$

Note that the scattering cross section is now only a function of the scalar q, i.e. a function of scattering angle 2Θ and the wavelength of the X-ray beam λ. It follows:

$$\frac{d\sigma}{d\Omega}(q) = r_0^2 \left\{ N \left\langle \left|F(\vec{q})\right|^2 \right\rangle_{\Omega} + \left\langle \sum_{j=1}^{N}\sum_{k\neq j}^{N} F_j(\vec{q}) \cdot F_k^*(\vec{q}) \cdot \exp(i\vec{q}(\vec{R}_j - \vec{R}_k)) \right\rangle_{\Omega} \right\}. \tag{3.16}$$

As a first characteristic quantity of small angle scattering, the so-called form factor is introduced:

$$\boxed{P(q) = \left\langle |F(\vec{q})|^2 \right\rangle_\Omega .} \tag{3.17}$$

It depends on the size and shape of the scattering particle and thus can be used to determine these quantities from the measured scattering intensities. A further discussion of the form factor of different systems will follow in sec. 3.2.

The second term in eq. 3.16 is characteristic for intermolecular interactions and will now be discussed further. It is assumed that interparticle distance and their orientation with respect to each other are not correlated. This decoupling approximation means that the relative orientation of two particles to each other is not influenced by their separating distance. Obviously, this approximation is only valid while the particle concentrations are not to high [Kotlarchyk and Chen, 1983]. Furthermore, very elongated shapes or anisotropic interactions between the particles (magnetic, electro static, hydrophobic surface spots,...) can interfere with this approximation.
In the decoupling approximation the form amplitudes can be averaged independently and therefore be factorized. It follows:

$$\left\langle \sum_{j=1}^{N} \sum_{k\neq j}^{N} F_j(\vec{q}) \cdot F_k^*(\vec{q}) \cdot \exp(i\vec{q}(\vec{R}_j - \vec{R}_k)) \right\rangle_\Omega = \langle F(\vec{q}) \rangle_\Omega^2 \cdot \left\langle \sum_{j=1}^{N} \sum_{k\neq j}^{N} \exp(i\vec{q}(\vec{R}_j - \vec{R}_k)) \right\rangle_\Omega . \tag{3.18}$$

Note, that in the first term of the right hand side the form amplitude is first averaged before the square is calculated, in contrast to the calculation of the form factor (eq. 3.17). Both quantities are only equal for particles with spherical symmetry (see eq. 3.25).
From the interference term, the spatial distribution of the scattering entities follows. In the isotropic, continuous case [Spalla, 2002], the interference term can be connected to the radial pair correlation function of the particles centers of mass, $g(r)$, as:

$$\left\langle \sum_{j=1}^{N} \sum_{k\neq j}^{N} \exp(i\vec{q}(\vec{R}_j - \vec{R}_k)) \right\rangle_\Omega = \frac{N^2}{V}\, 4\pi \int_0^{V^{1/3}} r^2\, g(r)\, \frac{\sin(qr)}{qr}\, \mathrm{d}r. \tag{3.19}$$

$g(r)$ is a measure for the order of the systems, i.e., to which extent the structure of the fluid deviates from complete randomness. It is defined so that the number of particles in a spherical shell of radius r and thickness $\mathrm{d}r$ around a particle at $r = 0$ is given by $4\pi n r^2 g(r)\mathrm{d}r$ [Klein, 2002]. A further discussion of the quantity follows in sec. 3.3. In this thesis, only systems lacking long range order will be discussed, therefore

$$\lim_{r\to\infty} g(r) \to 1$$

can be assumed. This fact can be used to split up the integral into two parts by the substituting

the distribution function as $g(r) - 1 + 1$. The first resulting integral reads as

$$\int_0^{V^{1/3}} r^2 \, (g(r) - 1) \, \frac{\sin(qr)}{qr} \, \mathrm{d}r, \tag{3.20}$$

being non-zero only for small r, where a short-ranged order is given. Hence, the upper limit of the integral boundary can be set to ∞ instead. The second integral reduces to the three-dimensional Fourier transform of the irradiated volume

$$\int_0^{V^{1/3}} r^2 \, \frac{\sin(qr)}{qr} \, \mathrm{d}r. \tag{3.21}$$

This results in a scattering contribution at very small and not detectable angles, so that this integral can be neglected.

The complete scattering can thus be written as:

$$\frac{d\sigma}{d\Omega} = r_0^2 N \cdot \left\{ P(q) + \langle F(\vec{q}) \rangle_\Omega^2 \cdot 4\pi \frac{N}{V} \int_0^\infty r^2 (g(r) - 1) \frac{\sin(qr)}{qr} \, \mathrm{d}r \right\}. \tag{3.22}$$

As a further characteristic quantity, the structure factor is introduced:

$$\boxed{S(q) = 1 + 4\pi \frac{N}{V} \int_0^\infty r^2 (g(r) - 1) \frac{\sin(qr)}{qr} \, \mathrm{d}r.} \tag{3.23}$$

The structure factor is connected to the radial pair correlation function and hence information on the intermolecular interactions of the sample systems can be obtained.

With this, the scattering cross section can be written as

$$\frac{d\sigma}{d\Omega} = r_0^2 N P(q) \cdot \{1 + \beta(q) \cdot (S(q) - 1)\}, \tag{3.24}$$

where

$$\beta(q) = \frac{\langle |F(\vec{q})| \rangle_\Omega^2}{\left\langle |F(\vec{q})|^2 \right\rangle_\Omega}. \tag{3.25}$$

As mentioned before, only in the case of centro-symmetric particles both terms on the right hand side are the same. In this case, $\beta(q) = 1$ and the scattering can be described by the product of form and structure factor. For not spherical particles, the so-called effective structure factor is introduced [Kotlarchyk and Chen, 1983]:

$$\boxed{S_{\mathrm{eff}}(q) = 1 + \beta(q) \cdot (S(q) - 1)}. \tag{3.26}$$

For the overall scattering intensity, this leads to

$$\boxed{I(q) = I_0 \frac{r_0^2}{L^2} \cdot N \cdot P(q) \cdot S_{\text{eff}}(q).} \tag{3.27}$$

As can be seen, the two q-dependent scattering contributions are the form factor, which exhibits information about the size and shape of the scattering particles, and the effective structure factor, which is sensitive to the spatial arrangement and thus intermolecular interactions of the scattering particles. Both quantities will be discussed in sec. 3.2 and sec. 3.3, respectively.

3.1.4 Contrast and transmission

Before discussing further the properties of form and structure factor, some general aspects of the experimental implementation and their consequences for the description of small angle X-ray scattering have to be considered.
So far, one assumption was the treatment of scattering particles in vacuum. However, the solvent or matrix, in which the particles are embedded, has its own, distinct electron density. These additional electrons in the irradiated sample volume give rise to further scattering of the X-ray beam, which has to be considered. Again, internal density fluctuations in the solvent or in the particle will be neglected and the density of the solvent will be treated as constant. The scattering amplitude of this system can be written in accordance to eq. 3.8 as:

$$A(\vec{q}) = \int_{\Phi V} \rho^{(P)}(\vec{r}) \cdot \exp(-i\vec{q}\vec{r})\ \mathrm{d}\vec{r} + \int_{(1-\Phi)V} \rho^{(S)} \cdot \exp(-i\vec{q}\vec{r})\ \mathrm{d}\vec{r}, \tag{3.28}$$

where $\rho^{(P)}(\vec{r})$ is the electron density of the particle, $\rho^{(S)}$ of the solvent, and Φ is the volume fraction of the sample occupied by the particles. The scattering amplitude can be rearranged as [Glatter, 2002]:

$$A(\vec{q}) = \int_{\Phi V} (\rho^{(P)}(\vec{r}) - \rho^{(S)}) \cdot \exp(-i\vec{q}\vec{r})\ \mathrm{d}\vec{r} + \int_{V} \rho^{(S)} \cdot \exp(-i\vec{q}\vec{r})\ \mathrm{d}\vec{r}, \tag{3.29}$$

so that follows:

$$A(\vec{q}) = \int_{V} \Delta\rho(\vec{r}) \cdot \exp(i\vec{q}\vec{r})\ \mathrm{d}\vec{r} + \rho^{(S)} \cdot \delta(\vec{q}). \tag{3.30}$$

The δ-function gives only a contribution at $\vec{q} = 0$, so that these scattering features are not detectable in the experiment. With this, an equal formulation for the scattering amplitude as in eq. 3.14 is calculated, only with an effective electron density $\boxed{\Delta\rho(\vec{r}) = \rho^{(P)}(r) - \rho^{(S)}}$ instead, which is the so-called contrast.
The scattering intensity is calculated by the square of the scattering amplitude, so the sign of the scattering contrast is lost. This means in particular that two complementary structures, like those shown in fig. 3.4, with opposite electron densities produce the same scattering pattern. This is known as the 'Babinet' principle in optics [Spalla, 2002].

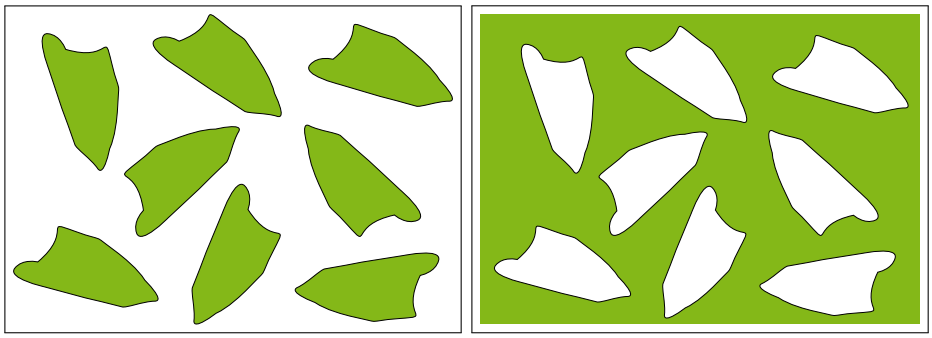

Figure 3.4: *The scattering pattern is dependent on the absolute electron density difference between the two phases. Two complementary structures, which have the same electron density difference (contrast), but with opposite sign, would give rise to the same scattering pattern.*

Comparing the electron density of proteins ($\approx 420 \frac{e^-}{nm^3}$) and water ($\approx 334 \frac{e^-}{nm^3}$), one can see the strong reduction of the scattering contrast, which results in a small signal-to-background ratio in the experiment. This problem can be accounted to by either increasing the measurement time or using an incoming X-ray beam of high flux, as it is the case for SAXS experiments at synchrotron facilities.

Besides the scattering contrast, also the absorption of the X-rays is of importance in the description of a scattering experiment. The absorption is characterized by the linear absorption coefficient μ, which can be considered in the case of protein solutions as the one of water. With d being the thickness of the sample, the transmission of the X-rays is calculated as $T = \exp(-\mu d)$ [Lindner, 2002].

With the described effects, the scattering intensity can be calculated as

$$\boxed{I(q) = I_0 \frac{r_o^2}{L^2} \cdot T \cdot A \cdot d \cdot n \cdot P(q) \cdot S_{\text{eff}}(q),} \tag{3.31}$$

with A being the spot size of the X-ray beam on the sample. Information about the structural properties of the investigated samples are only present in form and structure factor. Both quantities will be discussed in the following.

3.2 SAXS analysis: The form factor

The following paragraphs deal with the theoretical description of small angle scattering data to obtain information about the size and shape of the scattering particles from the measured data sets. The analysis methods can roughly be divided into model free approaches, when spatial information of the scattering object is directly calculated from the scattering curve, and approaches where scattering curves are calculated from suitable models. Here, the information are obtained by refining the models to the measured data.

In the case of highly diluted protein solutions ($c_P \leq 0.5$ mg/ml), the q-dependence of the scattering pattern can be described by the form factor of the proteins only because

$$\lim_{n \to 0} S(q) \to 1. \tag{3.32}$$

As already derived in the previous section, the form factor can be calculated as the orientational average of the square of the scattering amplitude of the considered particle:

$$P(q) = \left\langle |F(\vec{q})|^2 \right\rangle_\Omega .$$

The scattering amplitude has been established as the Fourier transform of the effective electron density, so that the square can be written out as:

$$\begin{aligned} |F(\vec{q})|^2 &= F(\vec{q}) \cdot F^*(\vec{q}) \\ &= \int \int_{V_p} \Delta\rho(\vec{r}_1) \cdot \Delta\rho(\vec{r}_2) \cdot \exp(-i\vec{q} \cdot (\vec{r}_1 - \vec{r}_2)) \, \mathrm{d}\vec{r}_1 \, \mathrm{d}\vec{r}_2 \\ &= \int \int_{V_p} \Delta\rho(\vec{r}_1) \cdot \Delta\rho(\vec{r}_1 - \vec{r}) \cdot \exp(-i\vec{q} \cdot \vec{r}) \, \mathrm{d}\vec{r}_1 \, \mathrm{d}\vec{r}. \end{aligned} \tag{3.33}$$

Here, $\vec{r}$ is defined as $\vec{r} = \vec{r}_1 - \vec{r}_2$. Now, the spatial autocorrelation function is introduced, which is defined as the convolution square of the effective electron density:

$$\gamma(\vec{r}) = \int_{V_p} \Delta\rho(\vec{r}_1) \cdot \Delta\rho(\vec{r}_1 - \vec{r}) \, \mathrm{d}\vec{r}_1 \tag{3.34}$$

A sketch of the geometrical form of the autocorrelation function is presented in fig. 3.5 a). It corresponds to the overlapping volume between the particle and itself shifted by the distance $\vec{r}$ [Glatter, 2002].

The square of the scattering amplitude can therefore be written as:

$$|F(\vec{q})|^2 = \int_{V_p} \gamma(\vec{r}) \cdot \exp(-i\vec{q} \cdot \vec{r}) \, \mathrm{d}\vec{r}. \tag{3.35}$$

The next step is the orientational averaging of this expression. The spatial average of this

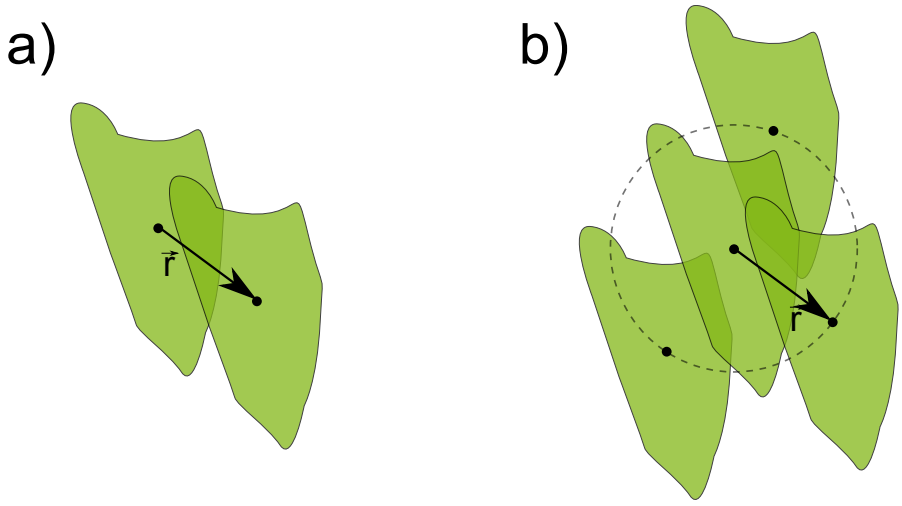

Figure 3.5: *a) Sketch of the calculation of the spatial autocorrelation function $\gamma(\vec{r})$. For a constant electron density $\Delta\rho(\vec{r})$ inside the particle, the overlapping volume between the particle and the same particle shifted by $\vec{r}$ corresponds to the convolution square [Glatter, 2002]. b) Spatially averaged performed for the calculation of the autocorrelation function $\gamma(r)$. The particle is shifted by $|\vec{r}| = r$, but averaged over all directions in space [Glatter, 2002].*

expression gives the form factor as [Debye, 1915, Glatter, 2002]

$$\begin{aligned} P(q) &= \left\langle |F(\vec{q})|^2 \right\rangle_\Omega \\ &= 4\pi \int_0^\infty \gamma(r) \cdot r^2 \cdot \frac{\sin qr}{qr}\, \mathrm{d}r. \end{aligned} \tag{3.36}$$

In this formulation, the autocorrelation function $\gamma(\vec{r})$ is replaced by the spatial average of the function $\gamma(r) = \langle|\gamma(\vec{r})|\rangle_\Omega$. This function has been introduced by [Debye and Bueche, 1949] and in its normalized form $\gamma_0(r)$ by [Porod, 1951]. It presents the spatial information from the scattering data transformed to real space.
The corresponding sketch can be seen in fig. 3.5 b). It shows that γ is only a function of the magnitude of the distance $r = |\vec{r}|$ and therefore the scattering intensity reduces to a function of the magnitude of q. Throughout this averaging, information about the system is lost so that a direct calculation of the particle's electron density from the scattering data is not possible. Nevertheless, routines have been established to interpret the scattering data in real space, which will be presented in the following.

In this context, the pair distance distribution function (PDDF) is now introduced, which is defined as

$$\boxed{p(r) = \gamma(r) \cdot r^2.} \tag{3.37}$$

For a homogeneous particle[1], the PDDF is a completely geometrical quantity. Considering two

[1] The electron density is treated as constant inside the particle. Therefore, the scattering intensity depends on the shape of the particle, only.

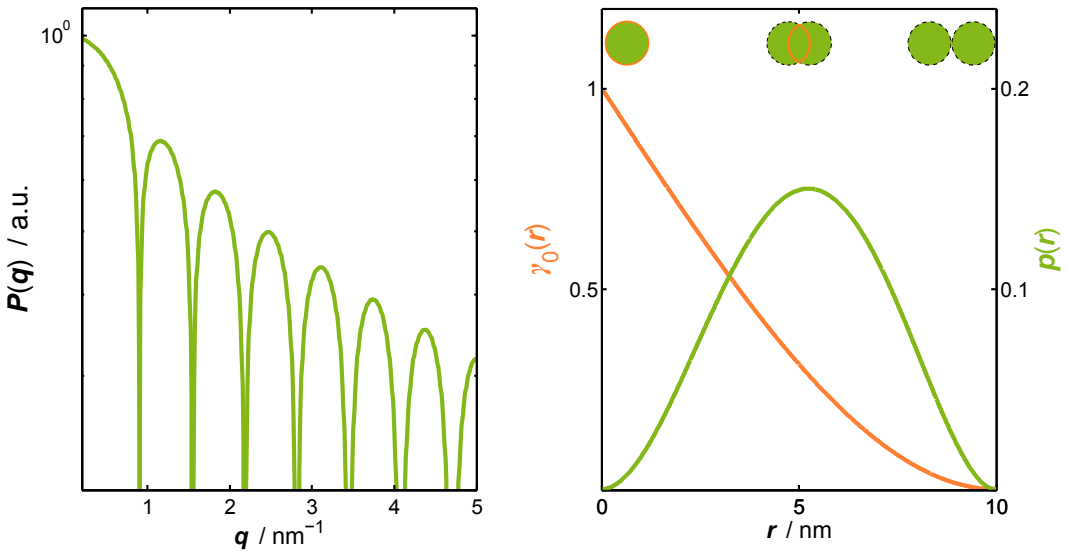

Figure 3.6: *Form factor $P(q)$, normalized autocorrelation function $\gamma_0(r)$, and partial distance distribution function (PDDF) $p(r)$ for a homogeneous sphere with radius $R = 5$ nm.*

arbitrary points inside a particle's volume, then $4\pi p(r)$ is the probability that the distance between them is equal to r [Porod, 1948].
In accordance to eq. 3.8, the scattering intensity can be calculated from $p(r)$ with

$$\boxed{P(q) = 4\pi \int_0^\infty p(r)\, \frac{\sin qr}{qr}\, \mathrm{d}r.} \tag{3.38}$$

The most general example that can be considered is the case of scattering from homogeneous spheres. In order to demonstrate the course of the previously introduced functions and the connections between those, this example will now be discussed.

3.2.1 Particles with spherical symmetry

The density distribution of a homogeneous sphere can be described as $\rho(r) = 1$ for $r \leq R$, $\rho(r) = 0$ for $r > R$, with R being the radius of the sphere. The calculations of $\gamma(r)$ and $p(r)$ can be made very easily as in this case a orientational averaging is not needed. Both functions read as [Glatter, 2002]

$$\gamma_0(r) = \left(1 - \frac{3}{4}\frac{r}{R} + \frac{1}{16}\frac{r^3}{R^3}\right) \tag{3.39}$$

and

$$p(r) = \frac{3}{4\pi}\frac{r^2}{R^2}\left(2 - \frac{3}{2}\frac{r}{R} + \frac{r^3}{8R^3}\right). \tag{3.40}$$

The functions are plotted for a sphere with radius $R = 5$ nm in fig. 3.6. As can be seen, the diameter of the scattering particle $d_{\max} = 10$ nm can easily be obtained from the course of $\gamma_0(r)$ and $p(r)$ as the value of r where both functions become equal to 0.

Furthermore, the scattering amplitude can directly be calculated in the considered case as:

$$\begin{aligned} F_{\text{sph}}(q) &= 4\pi \int_0^\infty \rho(r)\, r^2\, \frac{\sin(qr)}{qr}\, \mathrm{d}r \\ &= 4\pi\, \frac{1}{q} \int_0^R r \cdot \sin(qr)\, \mathrm{d}r \\ &= 4\pi\, \frac{1}{q} \left(-\frac{R}{q}\cos(qR) + \frac{1}{q^2}\sin(qR) \right) \\ &= \frac{4}{3}\pi R^3 \cdot \frac{3\left(\sin(qR) - qR\cos(qR)\right)}{(qR)^3} \\ &= V(R) \cdot F_0(q, R) \end{aligned} \tag{3.41}$$

The corresponding form factor of a sphere, $P(q) = |F(q)|^2$, is also shown in fig. 3.6. Sharp minima can be seen in the course of $P(q)$, which are typical for centro-symmetric particles. The radius of the scattering sphere is connected to the location of minima with $q \cdot R = 4.493, 7.725, \ldots$ [Glatter, 2002]. However, it is a difficult task to obtain structural information of the scattering object directly from the scattering intensity alone. Therefore, obtaining structural information of the scattering object via the calculation of the PDDF is an often used routine.

3.2.2 The pair distance distribution function

The form of the PDDF is a direct connection between the scattering information and the shape and dimension of the scattering particle. The example of the PDDF of a homogeneous sphere is shown in fig. 3.6 and fig. 3.7 (red), together with the PDDFs of some further, simple geometric bodies. The different shapes give rise to very different PDDFs, so that a rough determination of the particle's shape can be more easily gathered from the PDDF than the corresponding scattering function. For example, more elongated shapes (thin cylinder, green) can clearly be separated from the PDDF of a hollow sphere (blue) or a dumb bell (pink). Furthermore, the maximum diameter d_{max} of the object can directly be obtained as $p(r \geq d_{\text{max}}) = 0$.

As can be seen in eq. 3.38, the form factor is connected via a Fourier transform to the PDDF, so that theoretically the PDDF can be calculated from the scattering data as [Glatter, 2002]:

$$p(r) = \frac{1}{2\pi^2} \int_0^\infty I(q) \cdot qr \cdot \sin(qr)\, \mathrm{d}q. \tag{3.42}$$

However, this equation can not be used in practice, as $I(q)$ is not measured as a continuous function in the full regime of $0 < q < \infty$. This means, that in order to obtain real space information from the scattering data, different approaches have to be made.

A very common approach is the use of the so-called indirect Fourier transform [Glatter and Kratky, 1982]. Here the fact is used, that $p(r) = 0$, for $r > d_{\text{max}}$, with d_{max} being the diameter

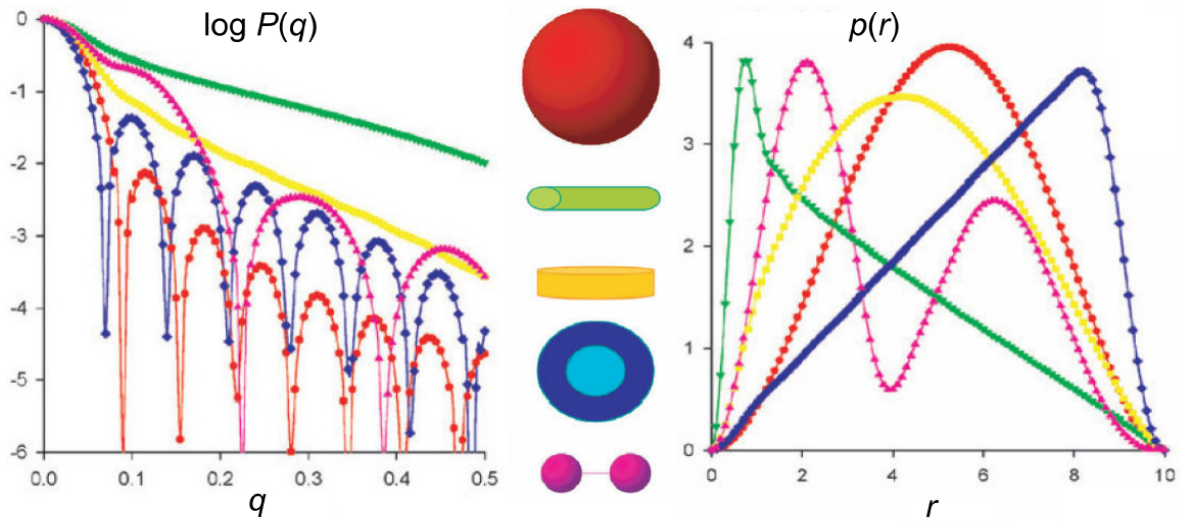

Figure 3.7: *Scattering intensities and pair distance distribution functions of various geometrical objects. Picture taken from [Svergun and Koch, 2003]*

of the scattering particle. Therefore, the PDDF is divided into a discrete set splines $p_A(r) = \sum c_i S_i(r)$, their weight is given by the coefficients c_i. The scattering intensity is calculated from $p_A(r)$ and refined to the measured intensity by varying the coefficients c_i. This procedure is implemented in the program GNOM [Svergun et al., 1988, Svergun, 1991, Svergun, 1992], which has been used in this thesis (see sec. 4.4). The advantage of this analysis method is that no model for the scattering object has to be chosen before the refinement. Only the maximum diameter of the object has to be estimated, in order to obtain reasonable results.

3.2.3 Modeling of form factors

As a consequence of the inability to obtain the shape of the considered particle directly from the scattering data, the approach of calculating the form factor from adjustable models is a further possibility. The form factor of a sample with known atomic structure can be calculated with the scattering formula of a set of discrete scatterers as [Debye, 1915]:

$$P(q) = \sum_j \sum_k f_j f_k \frac{\sin(q r_{jk})}{q r_{jk}}. \tag{3.43}$$

Here, r_{jk} is the distance between the two scatterers and f_j and f_k their scattering strength. The treatment of an averaged, homogeneous electron density inside the particle is sufficient for scattering at small angle in most cases, however. The scattering amplitude of simple geometrical bodies with a homogeneous density can often be calculated from an analytical form, the calculation for a homogeneous sphere has been shown as an example in eq. 3.41. Often, proteins or other macromolecules are modeled as simple geometrical objects and the dimensions are used as refinement parameter. Still, the decision of the best model has to be made carefully in order to obtain reasonable results.

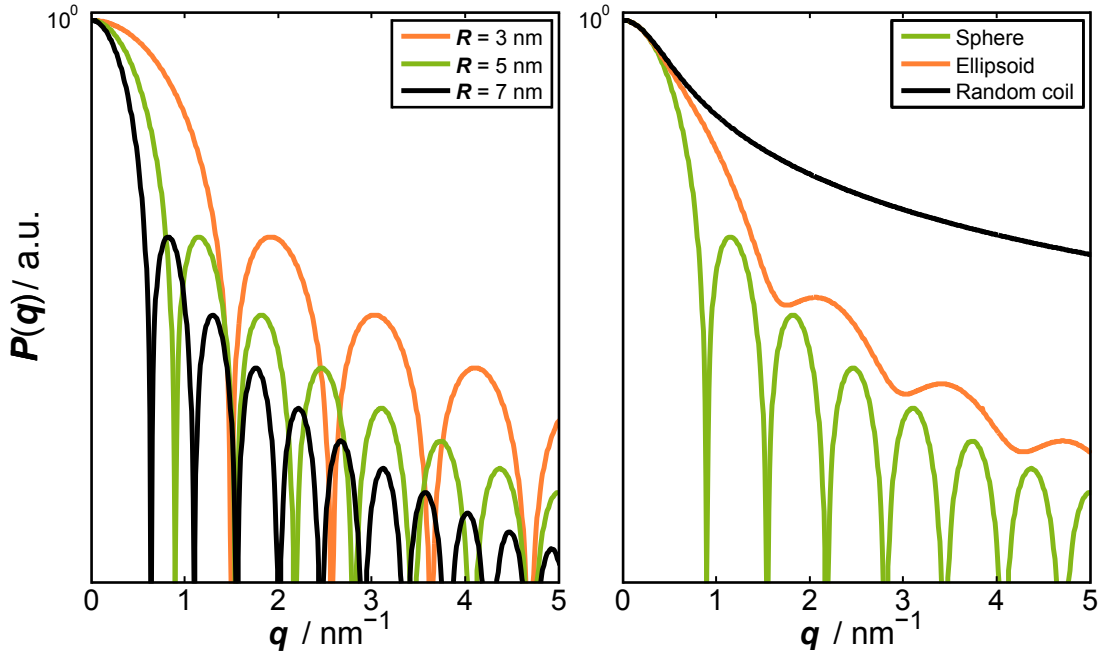

Figure 3.8: *The form factor for homogeneous spheres with radii of $R = 3$ nm, 5 nm, and 7 nm, respectively, and the form factor of a homogeneous sphere ($R = 5$ nm), an ellipsoid of revolution, and a random coil, all with the same radius of gyration $R_G = 3.88$ nm (see sec. 3.2.4).*

The form factors of some basic models are presented in the following:

- **Homogeneous sphere** (R: radius):

$$\begin{aligned} P(q) &= \left|F_{\text{sph}}(q,R)\right|^2 = V(R)^2 \cdot |F_0(q,R)|^2 \\ &= V(R)^2 \cdot \left(\frac{3\left(\sin(qR) - qR\cos(qR)\right)}{(qR)^3}\right)^2 \end{aligned} \tag{3.44}$$

- **Tri-axial ellipsoid** (a, b, c: semi-axes) [Mittelbach and Porod, 1962]:

$$P(q) = \int_0^1 \int_0^1 F_0^2(q \cdot r(x,y))\, \mathrm{d}x\, \mathrm{d}y \tag{3.45}$$

$$r(x,y) = \sqrt{\left(a^2\cos^2\left(\frac{\pi x}{2}\right) + b^2\sin^2\left(\frac{\pi x}{2}\right)\cdot(1-y^2) + c^2y^2\right)}$$

- **Ellipsoid of revolution** (a, b: semi-axes, j_1: first order Bessel function) [Guinier, 1939]:

$$\begin{aligned} P(q) &= \int_0^1 F_0^2(q\sqrt{a^2 + x^2(b^2-a^2)})\, \mathrm{d}x \\ &= \int_0^1 \frac{j_1(q\sqrt{a^2 + x^2(b^2-a^2)})^2}{(q\sqrt{a^2 + x^2(b^2-a^2)})^4}\, \mathrm{d}x \end{aligned} \tag{3.46}$$

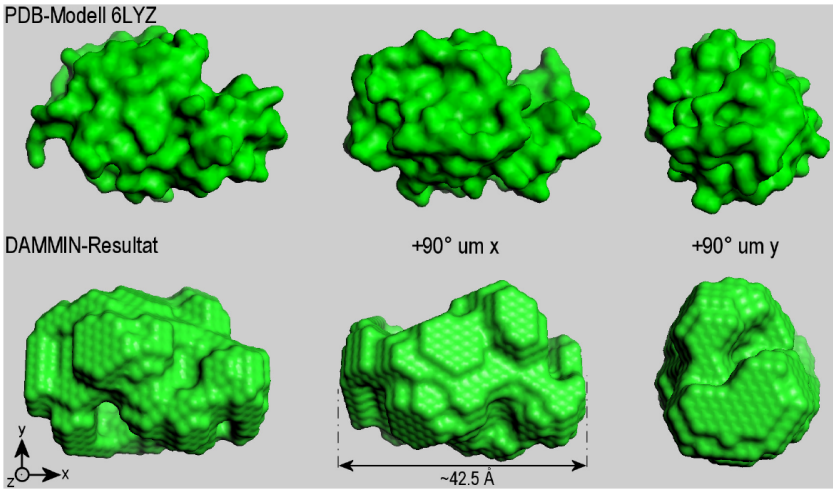

Figure 3.9: *Three dimensional representation of a lysozyme molecule calculated from the atomic coordinates deposited in the PDB and calculated by refining to SAXS data by using DAMMIN. Picture taken from [Krywka, 2008].*

- **Random coil** (R_G: radius of gyration (see sec. 3.2.4)) [Debye, 1947]:

$$P(q) = \frac{2\left(\exp(-q^2R_g^2) + q^2R_G^2 - 1\right)}{q^4R_G^4} \tag{3.47}$$

The SAXS curves for different geometrical particles are shown in figure 3.8. As can be seen, the scattering of centro-symmetric particles produces sharp minima in the SAXS curves. Furthermore, differences in the scattering curves can be seen, both for varying diameter and shape of the considered particles. This shows the sensitivity of the method on shape and size of the investigated particles.

It can be mentioned, that the structures of more complex particle surfaces can be obtained from SAXS data, too. The use of so-called dummy atom models has been proven to be successful in recent years. This approach is for example realized in the program DAMMIN [Svergun, 1999] (see fig. 3.9). Here, a search volume is completely filled with densely packed spheres of fixed position, which are either assigned to have the density of the solvent or the protein. The scattering signal of the configuration of the 'solute spheres' is then calculated. With certain stability mechanisms, which for example encounter for the connectivity of the solute dummy-atoms and the location of the model close to the center of the search volume, the configuration of 'protein spheres' is searched that minimizes the difference between measured and calculated SAXS curve. With this routine, a simple shape for the protein can be obtained. As an example, the refinement of a lysozyme molecule is shown in fig. 3.9.

In this work, which focuses on the intermolecular interactions of the proteins, the modeling of the from factor of lysozyme by refining the PDDF as well as the form factor of an ellipsoid of revolution was found to be completely sufficient. The modeling to the experimental scattering data is shown in sec. 4.4.

3.2.4 Asymptotic behaviour

The scattering from different geometrical objects produces scattering curves with very distinct differences. However, considering the asymptotic behavior of the form factor, some general descriptions can be formulated. A sketch of the considered q-range and the approximations made are shown in figure 3.10 for the case of a homogeneous sphere.
As indicated with a straight line in the double logarithmic plot, the high-q behavior follows a power-law behavior. For most proteins, the compact and only slightly anisotropic shape exhibits a so-called Porod q^{-4} behavior [Glatter, 2002], which is shown in fig. 3.10.
Furthermore, in the case of small wave vector transfers q, the form factor can be expanded and the first contribution reads as a Gaussian function [Guinier and Fournet, 1955]:

$$\boxed{I(q) \approx I(0) \cdot \exp(-q^2\ R_G^2/3).} \tag{3.48}$$

This formulation is known as the Guinier approximation, where the scattering of every object is only determined by its radius of gyration R_G. In particular, this means that the scattering of different shaped objects will be the same at very small q, if they all have the same R_G. The radius of gyration is a measure for the electronic extent of the scattering particle and is connected to the electron density distribution of a particle as:

$$R_G^2 = \frac{\int \Delta\rho(r)\ r^2\ \mathrm{d}V}{\int \Delta\rho(r)\ \mathrm{d}V} = \frac{\int p(r)\ r^2\ \mathrm{d}V}{2 \cdot \int p(r)\ \mathrm{d}V}. \tag{3.49}$$

In practice, R_G can be obtained by plotting $\ln I(q)$ vs. q^2, so that the scattering intensity describes a straight line. For data points where $R_G \cdot q \leq 1$ [Guinier and Fournet, 1955], R_G can be obtained from the slope of the scattering intensity. With eq. 3.49, the radius of gyration can also be determined from the pair distance distribution function. The calculated R_G for the previously discussed particle shapes are given in the following list:

- **Homogeneous sphere** (R: radius):

$$R_G = \sqrt{\frac{3}{5}} R \tag{3.50}$$

- **Ellipsoid of revolution** (a, b: semi-axes):

$$R_G = \sqrt{\frac{2a^2 + b^2}{5}} \tag{3.51}$$

- **Tri-axial ellipsoid** (a, b, c: semi-axes):

$$R_G = \sqrt{\frac{a^2 + b^2 + c^2}{5}} \tag{3.52}$$

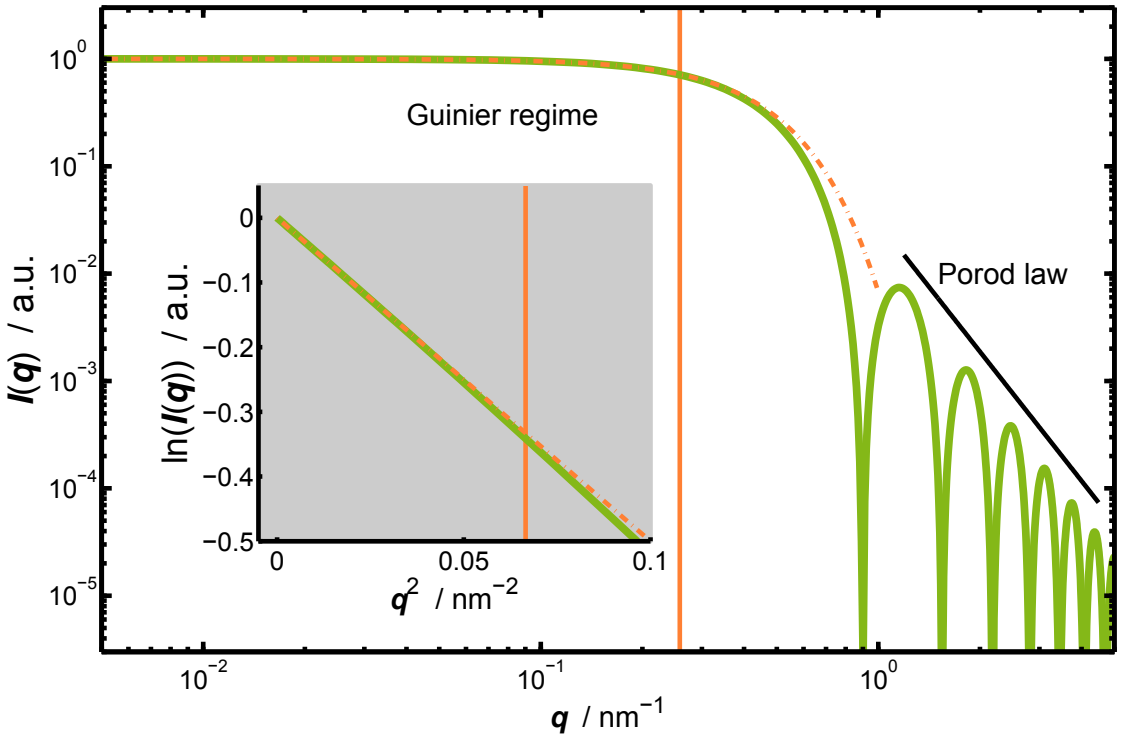

Figure 3.10: *Scattering intensity of a homogenous sphere with radius $R = 5$ nm. The Guinier regime is marked by $R_G \cdot q \leq 1$. The inset shows the Guinier fit in* $\ln(I)$ *vs.* q^2 *representation.*

- **Random coil** (N: number of elements of the chain, a: element length):

$$R_G = \sqrt{\frac{N}{6}}\, a \tag{3.53}$$

In the context of SAXS investigations on proteins, R_G is of special interest as an unfolding of proteins corresponds to a drastic change in their electronic extent [Panick et al., 1998, Panick et al., 1999, Schroer et al., 2010]. The increase of the radius of gyration can very easily be obtained from the scattering curve, so that denaturating solution conditions are recognized. This was used to assure non-denaturating solution conditions, see sec. 4.4.

3.3 Intermolecular interactions: The structure factor

From now on, the description will be expanded on the scattering of highly concentrated colloidal suspensions that includes the influence of the structure factor $S(q)$ (eq. 3.23). As previously discussed, this quantity depends on the radial pair correlation function $g(r)$, which describes the spatial particle-particle correlations [Hansen and McDonald, 1986]. The structure factor follows as

$$S(q) = 1 + 4\pi\ n \int_0^\infty r^2\ (g(r) - 1)\ \frac{\sin(qr)}{qr}\ \mathrm{d}r. \tag{3.54}$$

In the case of anisotropic or polydisperse particles, the decoupling approximation has to be considered additionally [Kotlarchyk and Chen, 1983], which has been discussed in sec. 3.1.3.
The calculation of the structure factor of concentrated protein solutions is outlined in the following, using the statistical mechanics description of simple liquids. In this concept, the solvent will be treated as a continuous background, characterized by its dielectric permittivity. Furthermore, the interacting macromolecules will be assumed as spherical particles, having a homogeneous surface net charge. Further details of this description can for example be found in [Hansen and McDonald, 1986, Klein, 2002, Nägele, 2008].

The challenging task is the calculation of $g(r)$ and $S(q)$ from a given pair potential [Nägele, 2008]. As mentioned before, $g(r)$ is defined as the probability of finding two particles separated by a distance r. The most simple case is the one of an ideal gas, where $g(r) = 1$. Here, the scattering particles are distributed randomly and therefore no interference occurs. In liquids however, a short ranged correlation between the particles exists, which gives $g(r) \neq 1$ for length scales smaller then the correlation length of the liquid, i.e. $r < \xi$. In case the liquid approaches near its critical point, this correlation length diverges. The implications for the structure factor will be discussed in sec. 3.3.5.

First, some general characteristics of structure factors will be discussed. The most simple example is the one of non-interacting, hard spheres, which is shown in fig. 3.11 for spheres with a diameter of 10 nm and volume fractions of 0.15 (orange) and 0.33 (green). The fact, that the spheres have a non-penetrable hard surfaces, results in an effective, short ranged repulsion. This gives a deviation of the $g(r)$ function from 1 at short distances (fig. 3.11 a)), which is more pronounced with increasing volume fraction. For larger distances, the particle are distributed randomly (fig. 3.11 b)). The corresponding particle-particle interaction potential has infinite height for distances smaller than the particle diameter, reflecting the not penetrable particle surface. For larger distances, the potential is equal to 0 (fig. 3.11 c)). The resulting structure factor modulates the scattering signal, which is given by a product of form and structure factor

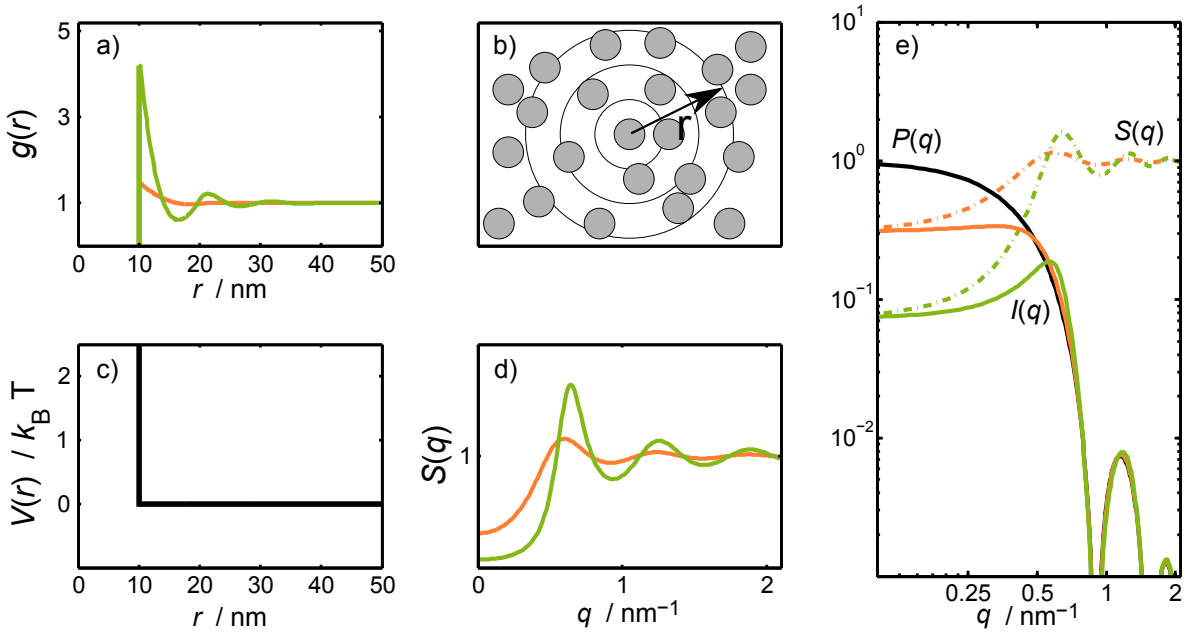

Figure 3.11: **a)** *Radial pair distance distribution function for a liquid of non interacting, hard spheres with a diameter of* 10 *nm and volume fractions of* 0.33 *(green) and* 0.15 *(orange), respectively.* **b)** *Representation of the spatial arrangement of hard spheres and their seperating distance r.* **c)** *Interaction potential of a hard sphere suspension. For distances smaller the diameter of the particles, the potential has infinite height, corresponding to the not penetrable particle surface. For larger distances, the potential is equal to* 0. **d)** *The resulting structure factor for the two volume fractions.* **e)** *The resulting scattering signal, which is given by the product of the form factor of a homogeneous sphere with diameter of* 10 *nm and the in d) shown structure factors.*

(fig. 3.11 d) and e)). For small q values, the structure factor converges to a certain value

$$\lim_{q \to 0} S(q) = n k_B T \kappa_T, \tag{3.55}$$

given by the isothermal compressibility of the suspension κ_T. For large q values however

$$S(q) \to 1$$

.

3.3.1 Ornstein-Zernicke equation

Connections between the presented functions can be calculated by using the Ornstein-Zernicke theory of simple liquids. In order to explain the opalescence of liquids close to the critical point (see also sec. 3.3.5), Ornstein and Zernicke introduced the following concept in 1914 [Ornstein and Zernike, 1914]. However, it has been proven to be suitable in many further applications.

The basic concept is that in a simple liquid the spatial correlations between two particles are not

only given by the direct interaction between them, but also by the indirect interactions involving additional particles.

In this context, the total correlation function

$$h(r) = g(r) - 1 \tag{3.56}$$

as well as the direct correlation function $c(r)$ are introduced. Both quantities are connected through the so-called Ornstein-Zernicke equation:

$$\boxed{h(r_{12}) = c(r_{12}) + n \int c(r_{13}) h(r_{23}) \, \mathrm{d}\vec{r}_3.} \tag{3.57}$$

The overall correlation between particle (1) and (2) is therefore described as the direct correlation between them ($c(r_{12})$) plus a further term. This term on the right hand side describes the before mentioned indirect correlations of the particles. A definition of $h(r)$ inserted iteratively into this term yields the correlation presented through direct correlation with a third particle, a fourth particle, and so on [Nägele, 2008]:

$$h(r_{12}) = c(r_{12}) + n \int c(r_{13}) c(r_{23}) \, \mathrm{d}\vec{r}_3 + n^2 \int c(r_{13}) c(r_{24}) c(r_{34}) \, \mathrm{d}\vec{r}_3 \, \mathrm{d}\vec{r}_4 + \mathcal{O}(c^4). \tag{3.58}$$

The OZ-equation presents the important link between particle correlations and the corresponding interaction potential. The direct correlation function can be connected to interaction potentials via suitable closure relations, which will be discussed in sec. 3.3.2. Furthermore, it can be connected to the structure factor. Rewriting eq. 3.57 by substituting $\vec{r} = \vec{r}_{12}$, $\vec{r}' = \vec{r}_{23}$ and consequently $|\vec{r} - \vec{r}'| = \vec{r}_{13}$ gives [Nägele, 2008]:

$$h(r) = c(r) + n \int c(|\vec{r} - \vec{r}'|) h(r') \, \mathrm{d}\vec{r}'. \tag{3.59}$$

The Fourier transform of this equation gives[2]

$$h(q) = c(q) + n \; c(q) \; h(q). \tag{3.60}$$

As $S(q) = 1 + n \; h(q)$, the general relation between the Fourier transform of the direct correlation function $c(q)$ and the structure factor $S(q)$ follows as

$$S(q) = \frac{1}{1 - nc(q)}. \tag{3.61}$$

In order to calculate the structure factor from a given interaction potential, so-called closure relations are needed that connect $c(r)$ with the interaction potential $V(r)$ of the proteins.

[2] Here, the convolution theorem for Fourier transformations is used: $\int \exp(i\vec{q}\vec{r})(f_1 * f_2)(\vec{r}) \, \mathrm{d}\vec{r} = f_1(\vec{q}) \; f_2(\vec{q})$ [Nägele, 2008]

3.3.2 Closure relations

The best choice of closure relations is dependent on the strength and range of the corresponding interaction potential as well as the particle density. Only for some closure relations in combination with certain interaction potentials, analytical solutions can be calculated. In the other cases, those solutions have to be calculated numerically.
In this thesis, two different closure relations were used. In the case of mainly repulsive proteins interactions, which are investigated in chapter 5, the mean-spherical approximation in combination with a 2-Yukawa potential was used. In chapter 6, where protein solution near phase boundaries, i.e. in highly attractive interaction regimes, were investigated, the Percus-Yevick closure relation with a sticky sphere potential was used. Explanations of the different interaction potentials will be given in the next section. The used relations are written as:

- **Mean-spherical approximation (MSA)** [Lebowitz and Percus, 1966]:

$$c_{MSA}(r) = -\beta V(r), r > \sigma \tag{3.62}$$

- **Percus-Yevick closure relation (PY)** [Percus and Yevick, 1958]:

$$c_{PY}(r) = (1 - \exp(\beta V(r)))\, g(r) \tag{3.63}$$

The PY approximation can be characterized as best suited for short-ranged interaction potentials [Nägele, 2008]. Additionally, analytical solutions exist for hard sphere [Percus and Yevick, 1958, Vrij, 1979] and sticky hard sphere potentials [Menon et al., 1991]. The MSA is better suited for midrange interaction potentials and moderate particle densities. Further closure relations are for example the hypernetted-chain approximation (HNC) [van Leeuwen et al., 1959] or the random phase approximation (RPA) [Nägele, 2008].

3.3.3 Interaction potentials

The previously presented closure relations can be used to connect the structure factor to a certain interaction potential. Different interaction potentials are presented in this section, which can be used to describe different protein solutions. The choice of the best model is dependent on the solution conditions of the investigated system, like for example the protein concentration or the ionic strength. The most relevant interaction potentials for this thesis are presented in the following.

- **hard sphere potential** (σ: diameter of particle):

$$V_{HS}(r) = \begin{cases} \infty, & 0 < r < \sigma \\ 0, & \sigma \leq r \end{cases} \tag{3.64}$$

- **attractive square well potential** (ϵ: depth of attractive potential; Δ: range of attractive

potential):

$$V_{SW}(r) = \begin{cases} \infty, & 0 < r < \sigma \\ -\epsilon, & \sigma \leq r \leq \sigma + \Delta \\ 0, & \sigma + \Delta \leq r \end{cases} \tag{3.65}$$

- **sticky hard sphere potential** (τ: sticking parameter, $\Delta \to 0$):

$$V_{SW}(r) = \begin{cases} \infty, & 0 < r < \sigma \\ \ln\left(12\tau\frac{\Delta}{\sigma+\Delta}\right), & \sigma \leq r \leq \sigma + \Delta \\ 0, & \sigma + \Delta \leq r \end{cases} \tag{3.66}$$

- **1-Yukawa-type potential** (J: strength of potential, d: range of potential):

$$V_{1Y}(r) = \begin{cases} \infty, & r < \sigma \\ J \cdot \sigma \cdot \frac{exp(-(r-\sigma)/d)}{r}, & \sigma \leq r \end{cases} \tag{3.67}$$

- **2-Yukawa-type potential** (J_a, d_a: strength and range of attractive potential, J_r, d_r: strength and range of repulsive potential):

$$V_{2Y}(r) = \begin{cases} \infty, & r < \sigma \\ J_r \cdot \sigma \cdot \frac{exp(-(r-\sigma)/d_r)}{r} - J_a \cdot \sigma \cdot \frac{exp(-(r-\sigma)/d_a)}{r}, & \sigma \leq r \end{cases} \tag{3.68}$$

The different interaction potentials presented are plotted in fig. 3.12. The most simple potential is the so-called hard sphere potential as it only regards the not penetrable particle surface. This hard sphere contribution is also present in all the other presented potentials. Most general for proteins in solution is the 2-Yukawa potential as it can be used to model the long-ranged repulsive Coulomb interaction as well as the a short ranged attractive interaction, which is mainly the van der Waals interaction potential. This potential was used in chapter 5 because varying ionic strengths of the solution can be implemented into the calculation of the potential. An increasing ionic strength in the solution decreases the strength of the repulsive coulomb interaction. The overall interaction potential for proteins in solutions of high ionic strength is more similar to the attractive 1-Yukawa potential shown in fig. 3.12. Additionally, the attractive square well potential is shown, with similar range and strength of the attractivity, which results in a nearly identical structure factor. A special case of this potential is the sticky hard sphere potential, which was used to refine the scattering from solution conditions of constant, high ionic strength (chapter 6). All three potentials shown, i.e. 1-Yukawa, square well, and sticky sphere, are sufficient to describe protein solutions where the repulsive coulomb potentials is strongly screened. However, the sticky hard sphere potential can analytically be solved using the Percus-Yevick relation [Menon et al., 1991], which strongly reduces the time needed to refine the model to the scattering curves.

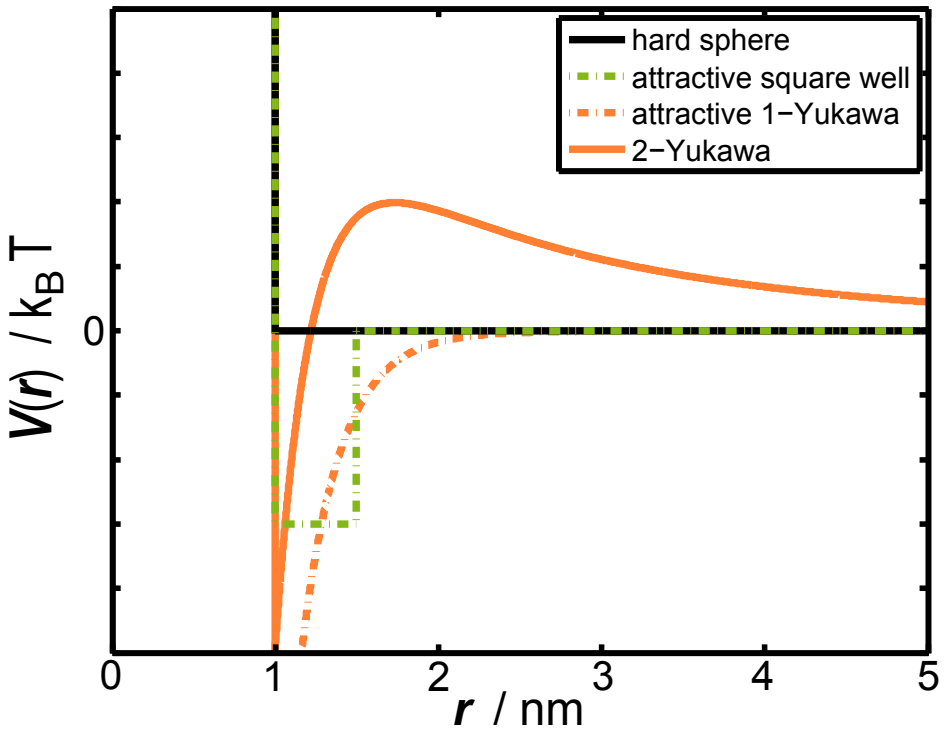

Figure 3.12: *The different used interaction potentials as a function of r/σ, with σ being the diameter of the considered particle.*

3.3.4 Second virial coefficient

The presented interaction potentials are functions of many various parameters. In order to compare solution conditions independent of the model used, one characteristic interaction parameter is needed. In this context, the second virial coefficient is introduced, which characterizes the strength of the interaction potential and is therefore often used to describe aggregation and crystallization phenomena.

It is defined as the second coefficient of the virial expansion of the osmotic pressure $\Pi(c)$:

$$\frac{\Pi(c)}{RT} = \frac{c}{M} + B_2 c^2 + B_3 c^3 + \ldots, \tag{3.69}$$

with M being the molecular weight, R the gas constant, T the temperature, and c the concentration. The classical virial expansion in thermodynamics describes the pressure of a many-body system as an expansion in density, where the virial coefficients B_i are characteristics for the interactions between the particles. For an ideal gas, the expansions ends after the first term, giving the ideal gas law. Therefore, the virial coefficients can be seen as a measure for a system's deviation from an ideal gas (see also sec. 2.3).

The second virial coefficient can directly be calculated from the protein-protein interaction potential as:

$$B_2 = 2\pi \int_0^\infty (1 - \exp(-V(r)/k_B T)) r^2 \, \mathrm{d}r. \tag{3.70}$$

It therefore describes the direct interaction strength between two proteins in solution.
In order to compare the virial coefficients for different proteins, the normalized second virial coefficient is introduced, which is independent of the protein's size. In the case of an 2-Yukawa interaction potential, it can be calculated as:

$$b_2 = \frac{B_2}{B_{HS}} = 1 + \frac{3}{8(R+\delta/2)} \int_{2R+\delta}^{\infty} (1 - \exp(V_{SC}(r) + V_Y(r)))r^2 \, \mathrm{d}r. \tag{3.71}$$

Here, δ is set to $\delta = 0.1437$ nm, in accordance to previous studies [Poon et al., 2000, Sedgwick et al., 2007], to suppress the divergence of the integral at $r = 2R$. In general, negative b_2 values correspond to mainly attractive interactions whereas positive values characterize repulsive interactions.
A special case is the calculation from the sticky sphere potential, as the normalized second virial coefficient is directly connected to the stickiness parameter with [Vliegenthart and Lekkerkerker, 2000]

$$b_2 = 1 - \frac{1}{4\tau}. \tag{3.72}$$

The benefit of b_2 has been shown in the case of protein crystallization, where solution conditions which foster proteins to crystallize are generally in certain range of b_2 values [George and Wilson, 1994]. Furthermore, it was shown that a value of $b_2 < -1.5$ is needed for proteins to undergo a liquid-liquid phase separation [Vliegenthart and Lekkerkerker, 2000, Noro and Frenkel, 2000].

3.3.5 Critical phenomena

Systems with short ranged attractive interactions, for example one component Lennard-Jones type systems like argon or suspensions of sticky colloidal spheres can bear a critical point of a liquid-gas-type demixing transition [Nägele, 2008]. In protein solutions, this phenomena is described as liquid-liquid phase separation, as here two proteins phases with differing concentrations form (see sec. 2.3).
To describe these phenomena in the formulation of scattering theory, the structure factor will be derived for large distances r and consequently small q. In the vicinity of the critical point, long-ranged spatial correlations between the particles occur, so that the volume integral over $h(r)$ and therefore $g(r)$ diverge in the limit of an infinite volume. The Fourier transform of the direct correlation function however, stays short ranged as [Nägele, 2008]

$$c(q \to 0) = 4\pi \int_0^{\infty} r^2 c(r) \, \mathrm{d}r \to \frac{1}{n}, \tag{3.73}$$

for $T \to T_c$. Therefore, $c(q)$ can be expanded in a Taylor series around $q = 0$, as [Nägele, 2008]

$$nc(q) = 4\pi n \int_0^{\infty} c(r) r^2 \frac{\sin(qr)}{qr} \, \mathrm{d}r = c_0 - c_2 q^2 + \mathcal{O}(q^4), \tag{3.74}$$

with the coefficients

$$c_0 = 4\pi n \int_0^\infty r^2 c(r)\, \mathrm{d}r \to 1 \tag{3.75}$$

$$c_2 = \frac{2\pi}{3} n \int_0^\infty r^4 c(r)\, \mathrm{d}r. \tag{3.76}$$

The substitution into eq. 3.61 gives the Ornstein-Zernicke relation for the near-critical structure factor for small q, i.e. $qR_U << 1$ with R_U being the range of the attractive potential [Ornstein and Zernike, 1914]

$$S(q) \approx \frac{1}{1 - c_0 - c_2 q^2} = \frac{1}{c_2} \frac{1}{\xi^{-2} + q^2} \tag{3.77}$$

with the correlation length

$$\xi = (c_2/(1 - c_0))^{1/2} = (c_2 S(0))^{1/2}. \tag{3.78}$$

In practice, the inverse of the scattering intensity plotted against q^2 gives a straight line in the so-called Ornstein-Zernicke plot:

$$1/I(q) \propto 1/S(q) = c_2 \left(\xi^{-2} + q^2\right). \tag{3.79}$$

The correlation length can thus be obtained experimentally from the constant slope c_2 and the intercept c_2/ξ^2. If the solution conditions come closer to the critical point, this value will diverge.

4 Experimental Setup & Data Treatment

The studies on concentrated protein solution were performed by high pressure small angle X-ray scattering experiments at different synchrotron light sources. In this chapter, the high pressure SAXS setup will be described. The SAXS experiments were performed with a custom built high pressure cell, which will be presented in sec. 4.1. The typical setup and implementation of a SAXS experiment will be shown in sec. 4.2, together with the description of the different SAXS beamlines at which the experiments were conducted. The sample preparation will be described in sec. 4.3. The principle data handling as well as the refinement routines used are introduced in sec. 4.4.

4.1 The high hydrostatic pressure setup

The main experimental parameter in this study is hydrostatic pressure. As the generation of hydrostatic pressure within a sample volume is much more challenging than for example the change of temperature or chemical composition, a special designed sample cell is needed. The employed sample cell was constructed, built, and previously used in the studies by C. Krywka [Krywka, 2008, Krywka et al., 2008]. In the following, only the main features of the cell and the adaptions that where made during this thesis will be presented. For a detailed description of the pressure cell, see [Krywka, 2008].

A sketch of the sample cell design is shown in figure 4.1. The sample cell consists of a compact body made from stainless steel (Inconel 718, 2.4668), in which the actual sample holder can be placed. Three orifices are inserted into the body. One is for placing the sample holder into the cell and two further for the entering and exit of the X-ray beam. The openings are sealed using O-rings and customized steel screws (1.6580). The orifices for the X-rays are additionally equipped with 1 mm thick diamond windows (type IIa, 6 mm diameter). The windows have a relatively small absorbance of X-rays compared to other materials, transmitting 60 % of the incoming photons[1], but are strong enough two withstand pressure of up to 7 kbar. The windows are glued onto special holders, to be fixed in position at low pressure. At increasing hydrostatic pressure, these so-called Poulter-type windows [Poulter, 1932] are fixed and sealed by the pressure.
Through the front opening, a fast exchange of the sample holder is possible. Furthermore, the change of a sample does not come along with moving of the diamond windows, which gives benefit in terms of background subtraction. A sketch of the sample carrier is shown in figure 4.1 c). The carrier can be filled through the filling channel with a thin needle and closed using

[1] Transmission for 2 mm diamond at a photon energy of 15 keV [Henke et al., 1991], the transmission is strongly energy dependent. The absorption of water has to be considered additionally.

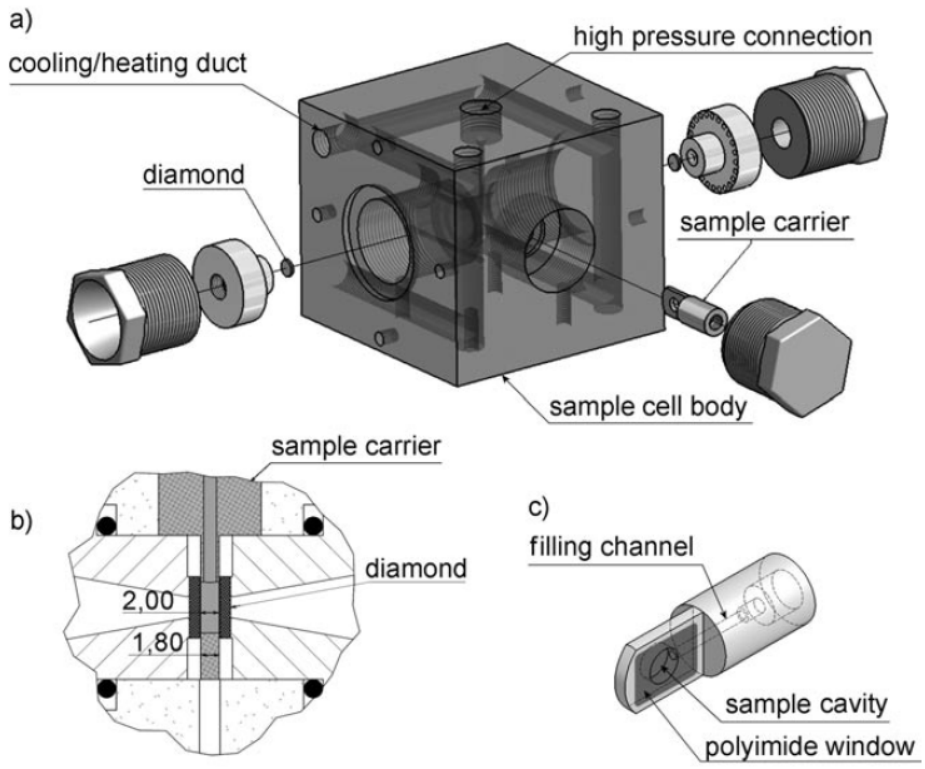

Figure 4.1: *Sketch of the high pressure cell [Krywka et al., 2008]. a) Cell body with steel screws and window holders. Beam passage happens through the two diamond windows. b) Blow-up sketch of the sample carrier (grey) placed into the sample cell between the two diamond windows (dark grey). c) Sketch of the sample carrier.*

a nylon screw (M 2.5). Water is used as pressure transmitting medium that can enter the cell through a high pressure connection on the top of the cell.

As the cell has already been used for several years, some small adjustments and renewals had to be made. First, the sample carriers were revised. Collapses of the polyimide foil windows of the sample carrier (fig. 4.2 c)) occurred from time to time when the pressure in the high pressure cell was increased from ambient conditions. Those malfunctions had their cause in small pressure differences between the pressure that pressed from outside onto the foil windows and the pressure that pressed onto the nylon screw. Small indentations were added into the sample carrier body to improve the passing of pressure transmitting water alongside the sample carrier. A picture of the new sample carrier is shown in fig. 4.2 a). Furthermore, the threads of the steel screws closing the pressure cell body were affected by corrosion as they had to withstand high pressure in constant contact with water. The front of the screw also presents the locating surface of the sealing O-ring, so that the increasing corrosion led to a leaking of the cell. Here, only the steel used for the screws (1.6580) was found to be affected by corrosion, not the one of the cell itself (2.4668). Therefore, the old screw design was changed to a two part design with a small plate as locating surface for the O-ring, made of the same material as the cell, and a slightly shorter screw made of the same material as before (see figure 4.2 b) and c)). Additionally, a small indentation was added into the plate, for better positioning of the O-ring and thus improved sealing. These

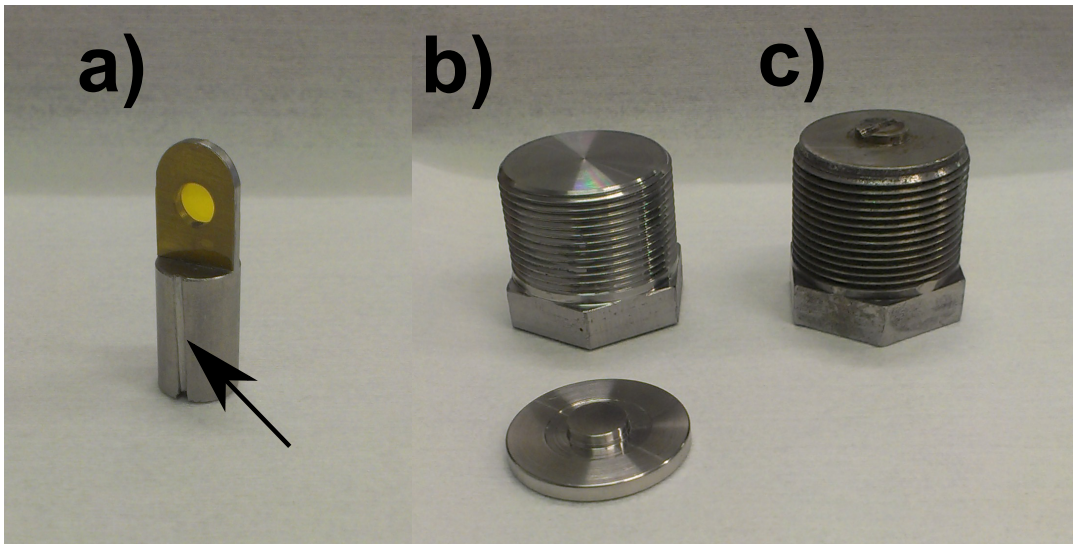

Figure 4.2: *Revised parts of the high pressure cell. a) Sample carrier with indentation at the front and back for improved passing of pressure increases alongside the sample carrier. b) & c) New and old version of the front screw. The front plate is made of steel (2.4668) instead of (1.6580) and has a gap for placing the O-ring.*

adjustments were made simultaneously with the design and construction of a new high pressure cell for X-ray reflectivity measurements at high hydrostatic pressure [Wirkert et al., 2014], which also has this adaptation.
The high pressure setup consists further of a hand spindle pump, a water reservoir, high pressure valves, and tubing, all purchased from NOVA Swiss. Additionally, the setup was equipped with two pressure detectors to measure the pressure in the cell and the pump separately.

4.2 Small angle X-ray scattering setups

A typical small angle X-ray scattering setup consists of several parts. First, the X-rays are generated at a source, which can be an X-ray tube or an insertion device in a storage ring. SAXS beamlines at storage rings have the advantage of using synchrotron radiation of high flux and tunable photon energy. The experiments in this work were performed at beamlines at different storage rings.

At synchrotron light sources the polychromatic X-ray beam is usually monochromatized by a double-crystal monochromator. The monochromatic X-ray beam is then passing through the X-ray optics. They can consist of various slits, attenuators, and focusing devices. The goal is to have a collimated, well defined X-ray beam profile. The actual design of the optics can vary from beamline to beamline. Usually, the beam is passing through a system of three slits that have the purpose of collimating the beam. The first slit is cutting of the side edges of the beam, which can originate from parasitic scattering at previous parts of the beam path. The second collimation slit is defining the beam. However, those slits can be the source of parasitic scattering themselves. Thus, a third set of slits located close to the sample is used to remove this kind of

scattering close to the primary beam.

The actual sample holder is positioned after the optics section. Here, various different sample environments exist, customized to the needs of the experiments. Besides the investigation of samples at high hydrostatic pressure, experimental setups for investigation of the influence of temperature, rheological parameters, mechanical stress, high magnetic fields, etc. have been built [Panine et al., 2003, Paulis et al., 2009, Davidson et al., 1997]. Also automated sample exchange systems have been employed at several SAXS beamlines, for high throughput studies mainly on biological samples [Hura et al., 2009, Martel et al., 2012, Pernot et al., 2013].

In the case of solution scattering of macromolecules or nanoparticles, the size of the sample container has to be considered. As proteins in solution only scatter a small portion of the incoming beam, one can increase the statistics of the measurement by increasing the thickness of the sample holder and therefore the number of particles in the beam. However, the thickness must not be too large as otherwise the approximation of a single scattering event loses its validity as well as the absorption of the X-rays increases. The optimum size of the sample container depends on the wavelength of the incoming beam as the transmitted intensity is proportional to

$$I \propto d \cdot \exp(-\mu d), \tag{4.1}$$

with d being the thickness of the sample and μ the wavelength dependent, linear attenuation coefficient. An optimum condition is reached for $d = 1/\mu$ [Lindner, 2002]. In case of protein solutions, the absorbance of water can be used as good approximation. For the resulting transmission in the experiment, the used sample cell has to be considered, too. This additionally adds two 1 mm thick diamond windows into the beam path. A higher transmission can be achieved by an increase of the photon energy. Furthermore, beam damages of the sample by the X-rays can be decreased with higher photon energy. Therefore, energies of 18 keV at beamline I22 (sec. 4.2.4) and 16 keV at ID02 (sec. 4.2.3) were used. At beamline BL9 and BW4, lower energies had to be used due to technical and spatial constrains, see sec. 4.2.1 & 4.2.2.

Subsequent to the sample cell, the SAXS setups consist of an evacuated flight path, which prevents signal loss due to air scattering of the transmitted primary beam and attenuation of the scattered X-rays, and a two-dimensional area detector. Using such a detector has the advantage of utilizing the complete isotropic scattering of the samples and the signal-to-noise ratio can be increased by performing an azimuthal averaging over the whole detector plane. Moreover, the complete q-range is measured in a single detector image, which also decreases the measurement time and sample exposure.

Since only a small portion of the incoming X-rays is scattered by the sample, the weak SAXS signal is overlaid by the primary beam. To prevent a damage of the detector due to the much stronger intensity of the direct beam, typically a beamstop in front of the detector is used. The beamstop can be equipped with a diode that measures the intensity of the transmitted, direct beam. With this, the normalization of the scattered intensity to the incoming beam intensity and sample transmission is possible, see also sec. 4.4.

The specific setups of the different SAXS beamlines will be presented in the following sections.

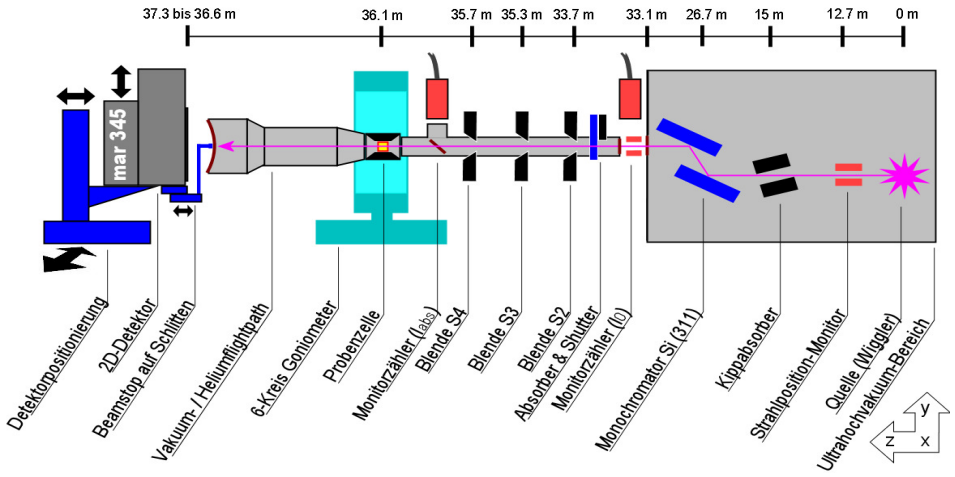

Figure 4.3: *The SAXS setup of beamline BL9, DELTA [Krywka, 2008].*

4.2.1 Beamline BL9, DELTA

The beamline BL9 is located at the electron storage ring DELTA (Dortmunder Elektronen-Speicherring-Anlage, Dortmund, Germany). DELTA is a synchrotron facility with an electron energy of 1.5 GeV and a maximum ring current of 130 mA. One wiggler, two undulators, and various bending magnets provide synchrotron radiation for several beamlines. BL9 is located alongside with the beamlines BL8 and BL10 at the superconducting asymmetric wiggler (SAW). The beamline is designed as a multi-purpose beamline, so that different setups for X-ray diffraction (XRD), gracing incident diffraction (GID), X-ray reflectivity (XRR), and SAXS exist [Krywka et al., 2006, Krywka et al., 2007, Paulus et al., 2008]. The SAXS setup is sketched in fig. 4.3. With a Si(311) double crystal monochromator, X-ray energies from 4 to 27 keV can be used in the experiments. The beam size is typically 1 mm in horizontal and 2 mm in vertical direction. At 10 keV, the flux is approximatly $5 \cdot 10^7 \frac{\text{photons}}{\text{s mm}^2 \text{ mA}}$ [Krywka et al., 2007]. Due to the small experimental hutch of BL9, only a maximal sample to detector distance $D \approx 1.33$ m for the SAXS setup is possible with a rigid vacuum flight path. The evacuated flight path has a maximum diameter of 200 mm. These constrains of the scattering geometry restrict the choice of the beam energy to 10 keV in order to take measurements on the needed q-range. The detector is a MAR345 image plate detector with a pixel size of 100x100 μm^2. A detailed description of the setup can be found in [Krywka et al., 2007, Krywka, 2008]. Typical exposure times for a single SAXS pattern were 20 minutes.

4.2.2 Beamline BW4, DORIS III

Beamline BW4 was located on the DESY campus (Hamburg, Germany) at the storage ring DORIS III, which was operating until October 2012. A picture of the experimental setup is shown in fig. 4.4. DORIS III was a positron storage ring with an energy of 4.5 GeV and a maximum ring current of 150 mA. Synchrotron radiation was used at 33 different beamlines. Beamline BW4 was served by a wiggler with hybrid magnet structure at a photon energy of

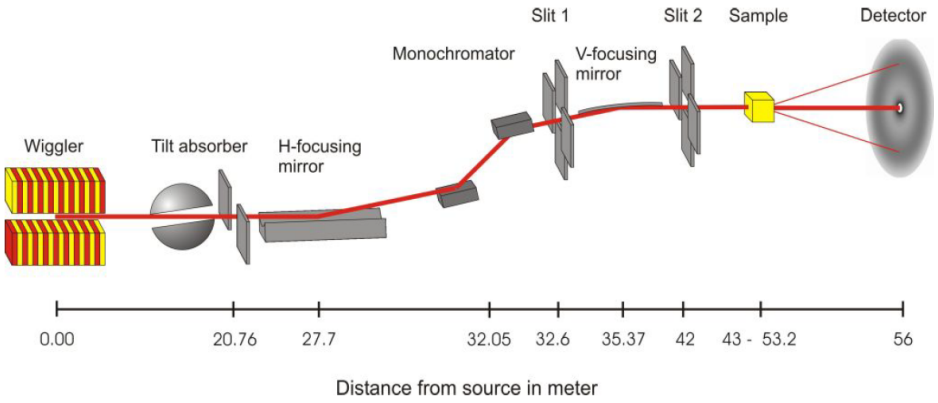

Figure 4.4: *Sketch of the experimental setup of beamline BW4, DORIS III [Beamline BW4, 2012].*

8.98 keV, using a Si(111) double crystal monochromator. The scattered intensity was recorded using a marCCD165 detector with 2048x2048 pixels and a pixel size of 79.1x79.1 μm^2. The focused beam size was 0.4 x 0.4 mm^2 [Roth et al., 2006]. SAXS patterns were taken with 20 minutes exposure time.

4.2.3 Beamline ID02, ESRF

The SAXS beamline ID02 is located at the European Synchrotron Radiation Facility (ESRF), Grenoble, France. The radiation is provided by three undulators (two U21.4, one U35) with high photon flux and low divergence. A cryogenic cooled Si(111) monochromator and a toroidal mirror are used in the beamline optics. A beam energy of 16 keV was used in the experiments, with a beam size of approximately 200 μm x 400 μm and a flux of the order of 10^{13} photons/sec [Narayanan et al., 2001]. This offered the possibility of taking a SAXS pattern with less than one second exposure time. The SAXS detector is mounted inside a 12 m detector tube and can

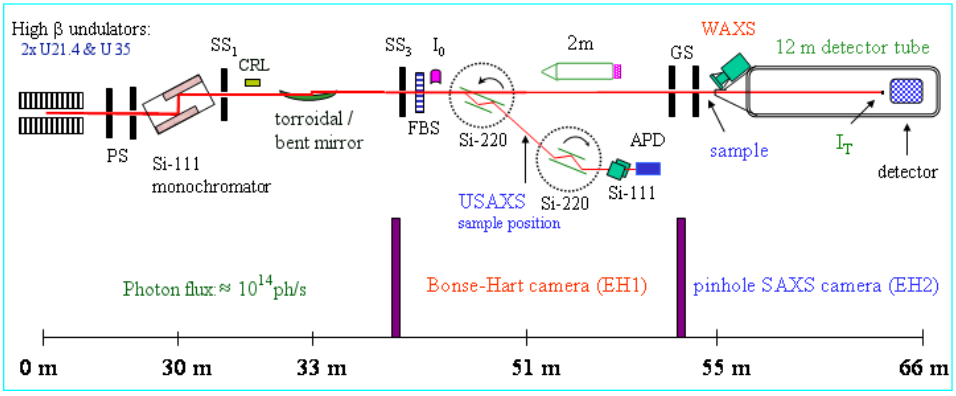

Figure 4.5: *Sketch of the experimental setup at beamline ID02 [Beamline ID02, 2014].*

be moved inside the tube from 1 to 10 m detector distances. The used detector was a FReLoN CCD detector with an active field of 100 mm x 100 mm and 2048 x 2048 pixels at a frame rate of 3 frames/second. The layout of the beamline is shown in fig. 4.5. In order to prevent beam damages due to the intense X-ray beam, different attenuator configurations were used. Exposure

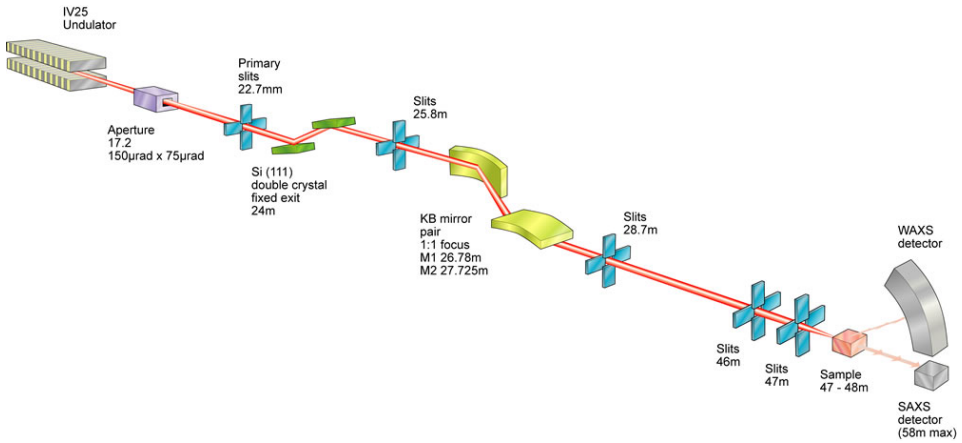

Figure 4.6: *Sketch of the experimental setup of beamline I22 [Beamline I22, 2014].*

times for one SAXS image were typically between 0.1 and 0.5 s.

4.2.4 Beamline I22, Diamond Light Source

Beamline I22 is situated at the synchrotron radiation source Diamond Light Source, Didcot, UK. It is served by an undulator equipped with a Si(111) monochromator, so that an energy range from 3.7 to 20 keV is accessible. A sketch of the beamline setup is depicted in fig. 4.6. For the

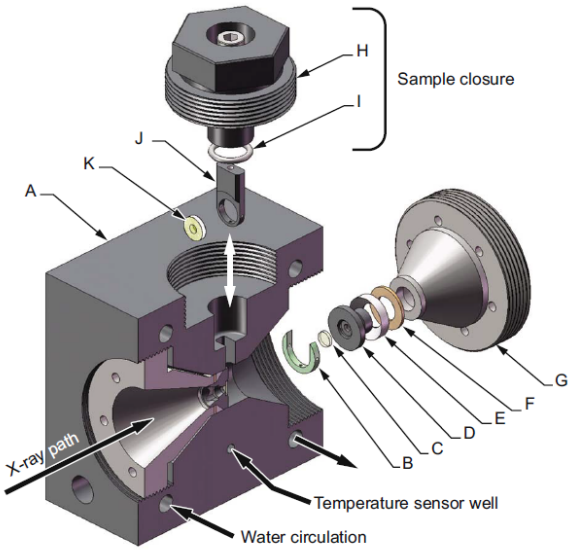

Figure 4.7: *Sketch of the high pressure cell used at beamline I22. Picture adapted from [Brooks et al., 2010].*

experiments, an energy of 18 keV with a sample to detector distance of 5.4 m was used. The SAXS patterns were recorded using a Pilatus 2M detector, the exposure time was 15 s.
In contrast to the experiments at the beamlines described before, an in-house high pressure sample cell was used at I22. A drawing of the sample cell is depicted in fig. 4.7.
The design of this cell is similar to the cell described before. Two openings of the cell are equipped with high pressure windows for the beam path through the cell. Here, sapphire windows were

used, which set the maximum pressure to 3 kbar. The samples were inserted into the cell through a third opening. The sample holder (J,K) has a different design as a small plastic spacer is used. Kapton foils were put on both sides of the spacer and sealed by using double faced adhesive tape. The sealing of the pressure cell is designed in a different way compared to the cell used before, for details see [Brooks et al., 2010].

4.3 Sample preparation

The protein lysozyme (14.3 kDa, pI 11, from hen egg white) was purchased from Roche GmbH, Mannheim, Germany, and used without further purification. As the pH value is an important parameter for studies on protein interactions, the buffer Bis-Tris was used for all samples. This buffer is capable of fixing the pH to 7 up to pressures of several kbar. A concentration of 25 mM was found to work well in the investigated pressure range [Schroer et al., 2011a, Schroer et al., 2011b].

Prior to the measurements, different buffer solutions were prepared, each with Bis-Tris and adjusted pH value. In the case of ionic strengths up to 100 mM, the proteins were freshly dissolved in the buffer solution before each measurement. For measurements with higher ionic strength as well as in the case of measurements as a function of salt type and concentration, the preparation of different stock solutions, either with protein or salt dissolved in buffer solution, makes the sample handling much easier during the beamtime. Therefore, stock solutions with varying salt type and salt concentration were prepared and mixed directly before use with a protein stock solution. Doing so, protein concentrations up to 10 wt.% at varying ionic strength could be reached (see chapter 5). The used salts were sodium sulfate (Na_2SO_4), sodium chloride (NaCl), and sodium phosphate (NaH_2PO_4, Na_2HPO_4), purchased from Sigma Aldrich Chemie GmbH, Steinheim, Germany. As the anions have different charges, the solutions were not prepared with the same concentrations but with matching ionic strengths. For the calculation of the ionic strength, see eq. 4.6. The phosphate samples were also prepared in the ration 0.39:0.61 (monobasic:dibasic), to obtain a pH of 7 already for the unbuffered solution.

Higher protein concentrations in solutions of high ionic strength were also investigated, described in chapter 6. A different preparation routine is needed, using dialysis cassettes. The cassettes (Slide-A-Lyzer, 2,000 MWCO, 15 mL, Thermo Scientific, Rockford, IL, USA) are constructed from two sheets of low-binding, regenerated-cellulose dialysis membranes that are permeable for water and buffer salts, but not for the proteins. After a short hydration of the membrane in millipore water, the cassettes were filled with lysozyme solution of 15 wt.% and placed in 1 L of 250 g/L polymer solution. The used polymer was Polyethylene glycol (PEG) with a molecular weight of 35000, purchased from Sigma Aldrich, Steinheim, Germany. The cassettes were kept in the polymer solution for 10-20 h at 30 °C under constant steering. As the membrane is permeable for the buffer, both, the protein as well as the polymer solution, consisted additionally of 25 mM Bis-Tris buffer adjusted to pH 7.

The final protein concentrations were determined by UV-Vis spectroscopy, using an extinction

coefficient of 2.64 mL/(mg cm) for lysozyme [Sophianopoulos et al., 1962] at a wavelength of 280 nm. A further protein free stock solution with 3 M NaCl and 25 mM Bis-Tris was prepared. Before each measurement, lysozyme and salt stock solutions were freshly mixed to obtain final protein concentrations of 18.5, 20.0, and 21.5 wt.% with 500 mM NaCl.

4.4 Data treatment and refinement

In the following, the principle data handling and reduction will be presented. The treatment of the raw data was different for every beamline, depending on the soft- and hardware available. The fundamental steps are the same, however, and will be described in this section.
The SAXS images were collected with different image plate detectors. The geometrical positioning of the experimental setup, e.g. the distance between the detector and the sample or the center of the scattering signal on the detector, were calibrated using a reference sample. The standard calibrant was silver behenate ($AgC_{22}H_{43}O_2$). Due to its large unit cell, silver behenate gives very well defined Bragg reflections at small angles.
After the calibration, the two-dimensional scattering pattern is azimuthaly averaged in order to obtain the scattering information as a function of wave vector transfer q, but different areas of the detector have to be excluded from the averaging first. For example, parts of the area detector are shadowed by the beamstop. Those areas are masked in the data processing routine, examples for used masks are shown in fig. 4.8.
Furthermore, the scattering from the diamond windows can give distinct scattering patterns on the detector. Those so-called Pseudo-Kossel lines emerge from reflections of the X-rays at lattice planes of the diamond and can cause higher or lower intensities at certain areas on the detector. In fig. 4.8 c), those emerging straight lines can be seen. In the processing, they are masked from the image (see fig. 4.8 f)). As the strength of this effect is strongly dependent on the orientation of the diamond windows, one can also try to minimize it by slightly rotating the sample cell with respect to the incoming beam. The best position was kept fixed for the complete experiment.

A huge portion of the scattered intensity can be treated as background of the measured SAXS signal. These scattering contributions originate from scattering of the diamond windows, the Kapton foil, and the solvent. In order to obtain the SAXS signal of the proteins, a background signal of the buffer filled sample cell is measured and can then be subtracted from the measured curve. To do so, the measured SAXS curve has to be normalized to the incoming flux of the X-ray beam and the transmission of the sample cell. Both values differ from measurement to measurement as the ring current of the storage ring changes as well as the transmission of the sample cell due to the increase of pressure. The normalized signal is calculated as

$$I_{\text{norm}}(q) = \frac{I_{\text{exp}}(q)}{I_0} \cdot \frac{1}{T} = \frac{I_{\text{exp}}(q)}{I_0} \cdot \frac{I_0}{I_{\text{T}}} = \frac{I_{exp}(q)}{I_{\text{T}}}, \tag{4.2}$$

with I_0 being the incoming intensity and T the transmission of the cell, which is the ratio of incoming and transmitted beam. At most beamlines, a diode in the beamstop measures a signal

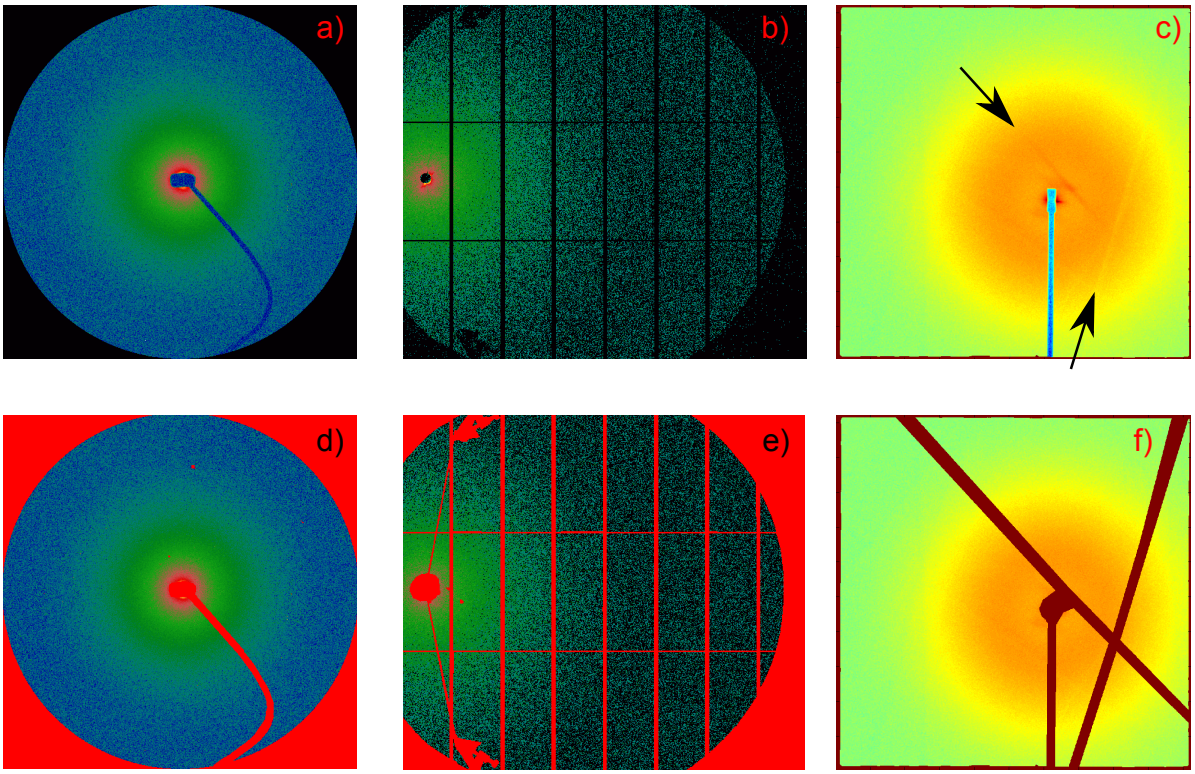

Figure 4.8: *a-c): Raw scattering images measured at beamline BW4 (a), I22 (b), and ID02 (c). d-f): The same images with the corresponding masks (red). Note the further masking in f) due to the Kossel lines on the detector.*

proportional to the transmitted intensity I_T. As can be seen, the incoming intensity is not needed for the normalization, but is often also measured and stored in the data files.

Further possibilities to normalize the scattering intensity are required, if for example the diode in the beamstop is missing or the normalization is not working accurately enough. In these cases, it is possible to calculate the overall scattering by integrating the scattering signal. A further method, which is used in this thesis, is to divide the scattering by the scattering intensity at high q-values, i.e. at the outer part of the detector. The scattering in this area is mainly caused by background contributions. Still, the normalization with the beamstop diode was found to be sufficient in most cases.

An exact background subtraction is not only defined by an accurate normalization of the scattering curves since the background curves have to be scaled by an additional factor α. The SAXS curve is then given as:

$$I(q) = \frac{I_{\text{exp}}(q)}{I_T^{(e)}} - \alpha \cdot \frac{I_{\text{buffer}}(q)}{I_T^{(b)}}. \tag{4.3}$$

The scaling factor is close to 1, but is deviating from this value with increasing protein concentration, i.e. less solvent scattering. An approximation for protein solutions is $\alpha = 1 - c_{\text{mg/ml}} \cdot 0.743/1000$. For lysozyme solutions, many prior measurements have been performed that can be used as validation for a good background subtraction. Furthermore, scattering contributions

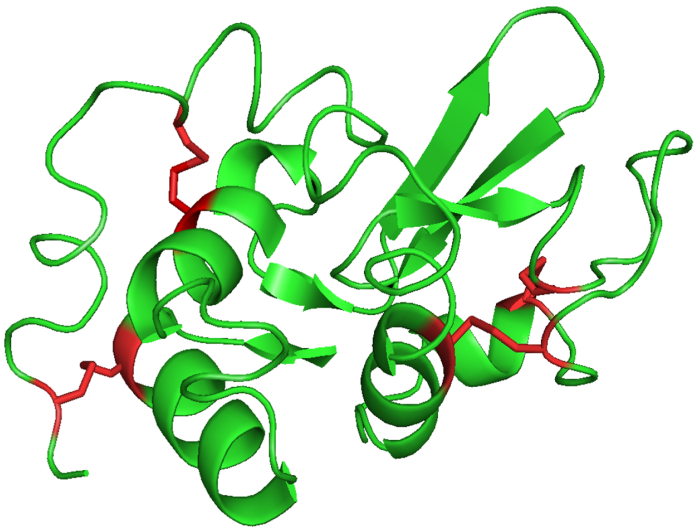

Figure 4.9: *Three dimensional structure of lysozyme, the four disulfide bonds are marked in red. The shape of lysozyme is roughly that of an ellipsoid with volume* $(\pi/6)$ 4.5 x 3 x 3 nm^3.

from the kapton foil ('Kapton peak') can be found at $q = 3.8$ nm^{-1}. After a proper background subtraction, this peak should not be visible in the scattering pattern. In any cases, a perfect background subtraction is a difficult task. However, it is more important that the background correction is made uniformly for all measured SAXS curves.
A special case is the measurement of highly concentrated lysozyme solutions as in this case the high-q region of the obtained structure factor can be used as criterion for a good background subtraction (see fig. 5.3). With this, a consistent background subtraction was additionally checked in this thesis.

The first step of the data refinement process was the modeling of the form factor of the lysozyme molecules. A three-dimensional representation of lysozyme is depicted in fig. 4.9. Lysozyme is a small, globular protein consisting of four α-helices and three β-sheets. Furthermore, four disulfide bonds are present in lysozyme, making it very stable against external perturbations (marked in red). It has a pI of 11 [Kuehner et al., 1999] and a molecular weight of 14.3 kDa, consisting of 129 amino acids. As it is a bactericidal enzyme, inducing an osmotic collapse of bacterial cells, it can be found in many secretions of vertebrates, like tears or saliva. In hen egg white, lysozyme occurs in very high concentrations. It can be extracted from the egg white in large amounts, making hen egg white (HEW)-lysozyme one of the most studied proteins.
The scattering of a diluted lysozyme solution together with the corresponding refinements is depicted in fig. 4.10 a) and b). The dashed line is calculated with the model free approach, by refining the pair distance distribution function $p(r)$ to the scattering curve. The $p(r)$-function is

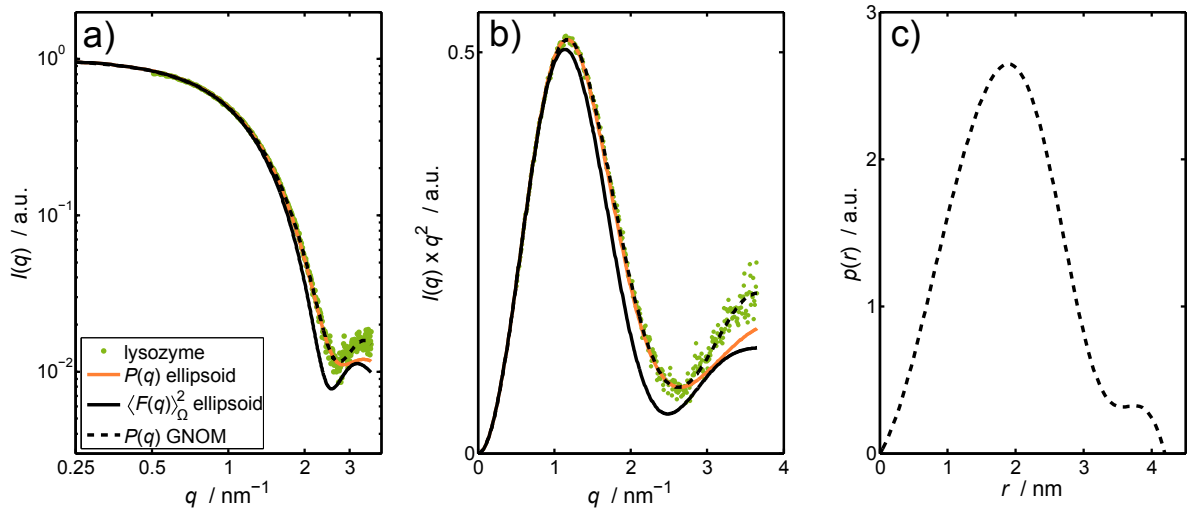

Figure 4.10: *a) SAXS curve obtained from a diluted lysozyme solution and refined by the form factor of an ellipsoid (orange) and by the calculation of the distance distribution function with the program GNOM (dashed black line). b) Corresponding scattering curve and refinements in a Kratky plot. c) Resulting partial distance distribution function $p(r)$. The calculated radius of gyration is $R_G = 1.45$ nm.*

plotted in fig. 4.10 c). As can be seen, the model can reproduce the scattering curve very well. The globular shape of the protein is reflected in the course of $p(r)$, giving a radius of gyration $R_G = 1.45$ nm (see eq. 3.49).

Since the proteins have no perfect spherical shape, the decoupling approximation is needed for the modeling of the effective structure factor (see eq. 3.25). Hence, the form factor has to be modeled by an analytical expression to obtain the scattering amplitude, too. The refinement of an ellipsoid of revolution to the scattering data is also displayed in fig. 4.10 a) and b) (orange). With $a = 1.52$ nm, $b = 2.42$ nm, and a constant $c = 0.0078$, the scattering signal was refined reasonably well. Notably, the model has the same radius of gyration $R_G = 1.45$ nm and follows the course of the scattering curve until the first minimum of the form factor. A small constant was added to $\langle F(q)\rangle^2_\Omega$ as well as $P(q)$, as $\langle F(q)\rangle^2_\Omega$ has very distinct minima, being 0 at certain q values that would result in an unphysical course of $\beta(q)$. To prevent these steep minima, $\langle F(q)\rangle^2_\Omega$ can for example be convoluted with a small dispersion, corresponding to the resolution of the experiment. A very similar effect has the addition of a constant, which was chosen so that $P(q)$ and the measured scattering intensity are matching in the best possible way. The same constant was then also added to $\langle F(q)\rangle^2_\Omega$.

In order to obtain the intermolecular interactions of proteins at several solution conditions from the SAXS data, an important assumption is that changes in the surrounding conditions do not affect the form factor of the proteins, i.e. no unfolding of the proteins happens. To validate this, the radius of gyration was measured in different solution conditions. Diluted lysozyme samples (5 mg/ml) were measured as a function of pressure in pure buffer solution as well as solutions with high ionic strength of $I = 1$ M. The used salts were sodium chloride, sodium phosphate, and sodium sulfate. The radius of gyration was obtained by refining eq. 3.48 to the scattering data,

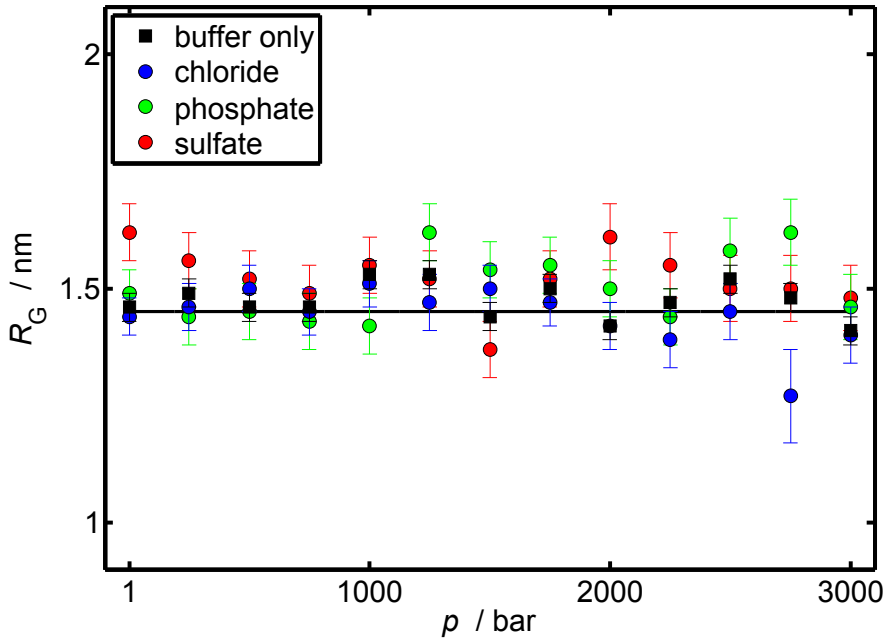

Figure 4.11: *Pressure dependence of the radius of gyration R_G of lysozyme in different solutions. The salt solutions contained sodium chloride, sodium sulfate, and sodium phosphate at an ionic strength of $I = 1$ M. The straight line marks the value of $R_G = 1.45$ nm, which was used to model the form factor of the proteins. No unfolding due to pressure or high ionic strength was observed.*

the results for R_G are shown in fig. 4.11. The addition of salt has no effect on the stability of the lysozyme molecules and no unfolding can be observed. Note that the scattering contrast of the proteins is reduced in the salt solution, as the solved ions increase the mean electron density of the solvent. Therefore, the scattering signal has lower statistics, which results in larger deviations in the obtained R_G values compared to the values measured in pure buffer solution.

The structure factors of the concentrated protein solutions were calculated by using two different models. In mainly repulsive solution conditions, the 2-Yukawa model was used (see eq. 3.68). Corresponding to the DLVO description of colloidal suspensions (see sec. 2.2), the two Yukawa terms can be written as

$$\begin{aligned} V_{DLVO} &= V_{SC} + V_Y \\ &= \frac{e^2}{4\pi\epsilon_0\epsilon_r} \frac{Z^2}{(1+0.5\sigma/\lambda_d)^2} \frac{\exp(-(r-\sigma)/\lambda_d)}{r} - J\cdot\sigma \frac{\exp(-(r-\sigma)/d)}{r}. \end{aligned} \tag{4.4}$$

The structure factor of this potential can be calculated with the MATLAB code by [Liu et al., 2005]. The effective hard sphere diameter of the proteins is $\sigma = 2.99$ nm and the volume fraction was calculated using the density of lysozyme $\rho = 1.351$ g cm^{-3} [Cardinaux et al., 2007]. At pH 7, the effective protein surface net charge has a value of $Z = 8$ [Kuehner et al., 1999], which was kept constant for all refinements. The further parameters of the repulsive interaction are the elementary charge e, the Boltzmann constant k_B, the temperature T, the Avogadro number

N_A, the vacuum dielectric constant ϵ_0, the dielectric permittivity of the solutions ϵ_r, and the reciprocal Debye-Hückel screening length κ. The temperature and pressure dependence of the dielectric permittivity of the solution was taken into account, following experimental values from [Floriano and Nascimento, 2004]. The screening length was calculated as

$$\lambda_d = \kappa^{-1} = \sqrt{\frac{\epsilon_0 \cdot \epsilon_r \cdot k_b \cdot T}{2 \cdot N_a \cdot e^2 \cdot I}}, \tag{4.5}$$

where

$$I = \frac{1}{2} \sum_{i=1}^{n} c_i z_i^2 \tag{4.6}$$

is the ionic strength of the salt solution with c_i the concentration and z_i the charge of the ion type i. The width of the attractive interaction was set to $d = 0.3$ nm and the strength J was used as the free parameter to model the measured SAXS curves.

For solution conditions near the LLPS phase boundary, the repulsive part of the interaction potential can be neglected as the high ionic strength I almost completely screens the surface net charge of the proteins. Hence, a simpler model was used, namely the sticky hard sphere potential (eq. 3.66). As the structure factor is calculated in the limit of the range of the attractive potential $\Delta \to 0$, no range for the attractive potential has to be set. In the limit of an infinitesimal small ranged and infinite deep potential, the free parameter to refine the model to the data is the sticky parameter τ. The resulting structure factor of this so-called Baxter model has an analytical solution in the Perkus-Yevick approximation [Menon et al., 1991]. The volume fraction was calculated as for the 2-Yukawa potential; a slightly smaller hard sphere diameter $\sigma = 2.9$ nm as global parameter for all curves was found to refine the curves better for this model.

A further issue in the data refinement was the pressure dependence of the volume fractions. Due to the different compressibilities of the bulk water, the hydration shell water, and the lysozyme molecules themselves, the correct calculation of the pressure effects on the volume fraction, especially at very high protein concentrations, is not an easy task. Basically, two options can be reviewed. In a first-order approximation, the compressibility data of the neat solvent can be used to calculate the resulting increase of the volume fraction, assuming the volume of the proteins to be constant. This certainly present an overestimation of the expected pressure effect. The other option is to keep the volume fraction constant as a function of pressure, i.e. assuming the same compressibility for water and proteins. As an example, the resulting b_2 values from the refinement to the scattering data with this two options are plotted in fig. 4.12 for a 21.5 wt.% lysozyme solution with 500 mM NaCl at different temperatures. The interaction potential used for the refinement is the sticky hard sphere model.
The colored data points correspond to a constant volume fraction of 0.154. The gray data points are the corresponding refinements using the slightly increasing volume fraction calculated from

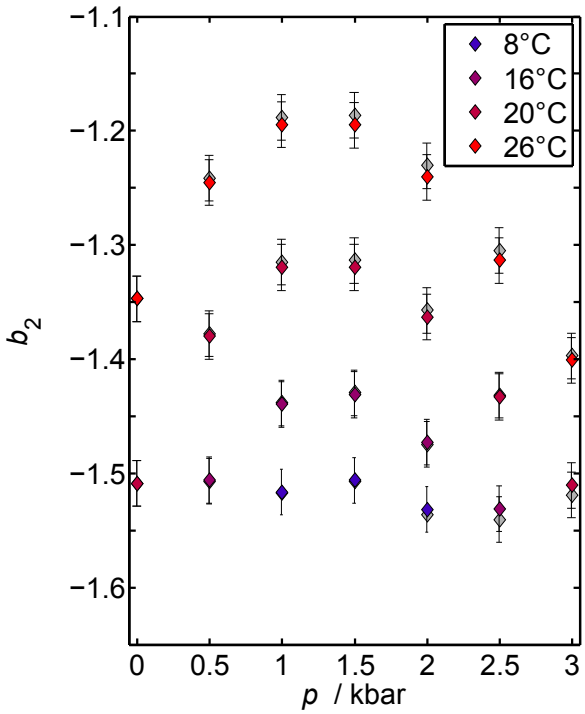

Figure 4.12: *Comparision of resulting b_2 values obtained from refinements to the scattering curves with a constant volume fraction (colored) and an increasing volume fraction calculated from bulk water compersibility data (gray). As can be seen, the effect on the results is small.*

the compressibility of bulk water that increases from 0.154 at 1 bar to a maximum value of 0.167 at 3 kbar, i.e. by about 6%. As can be clearly seen, the increasing volume fraction has only a small effect on the refinement results. Owing to the uncertainties in the compressibility data, the volume fraction is therefore kept constant in the fitting procedures in this thesis.

5 Protein-Protein Interactions

The phase behavior of a dense protein solution is governed by the underlying protein-protein interaction potential. In this chapter, results on the intermolecular interaction potential of lysozyme are presented, probed as a function of various parameters. This study has the purpose to quantitatively characterize the protein-protein interaction potential as a function of pressure and temperature as well as salt type and concentration. Information is obtained on how to manipulate protein interactions with pressure, e.g. for crystallization purposes, as well as on how various anions affect the pressure dependence. The protein-protein interactions are characterized in terms of the second virial coefficient $b_2(p, T, c_S)$ as a function of the before mentioned parameters. The results have been published in [Möller et al., 2012] and [Möller et al., 2014b].

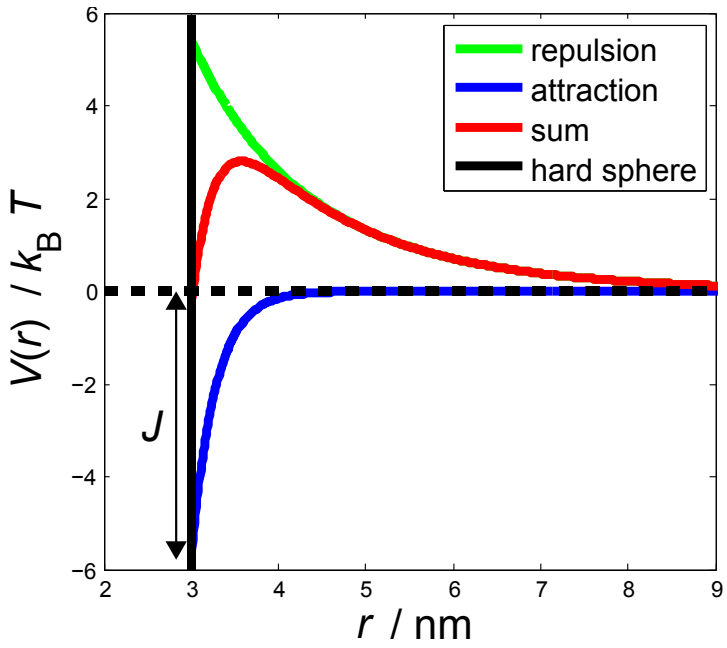

Figure 5.1: *Intermolecular interaction potential $V(r)$ modeled as a 2-Yukawa potential. The repulsive part is a screened Coulomb potential. The strength of the attractive interaction, J, was used as free parameter to model the calculated structure factor to the scattering data.*

The protein used in all investigations is lysozyme. Protein concentrations from 5 to 20 wt.% were studied on a temperature range from 8 to 45 °C and pressures from 1 bar to 3 kbar. Sodium chloride, sodium phosphate, and sodium sulfate solutions of varying ionic strength up to 400 mM were investigated.

The obtained SAXS curves are refined by calculating the structure factor from a 2-Yukawa interaction potential, presented in fig. 5.1. The strength of the attractive part of the interaction potential, J, is the free parameter to adjust the model to the data. The second virial coefficient

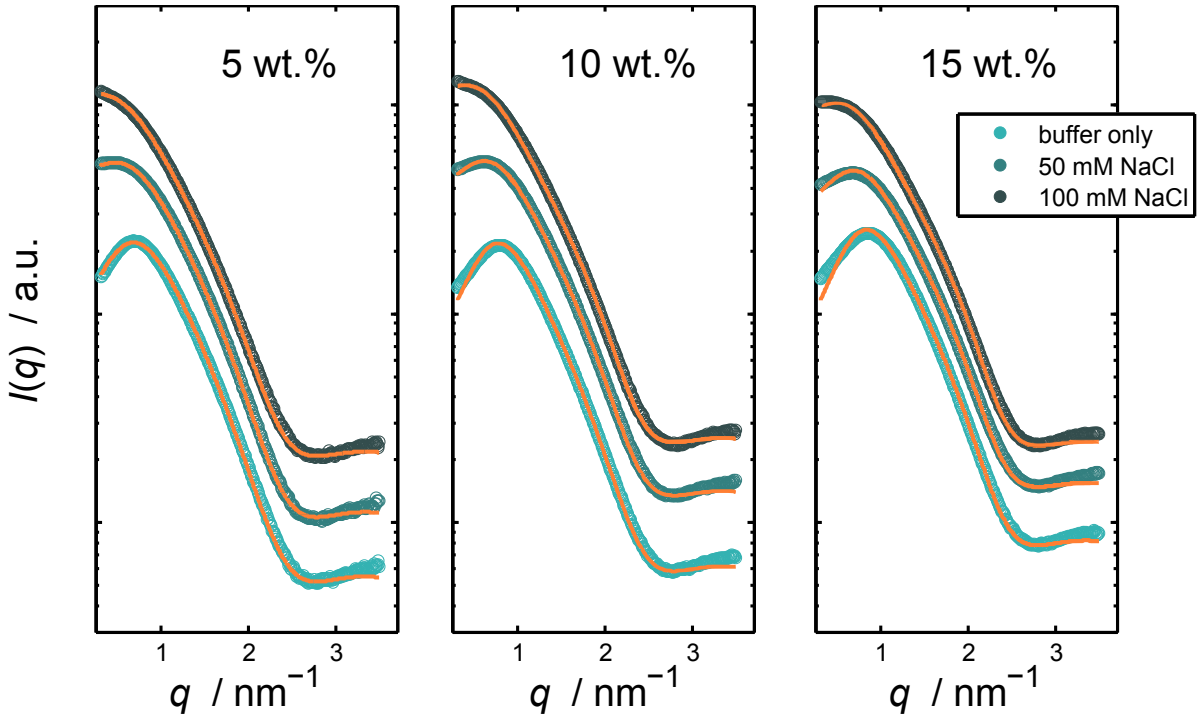

Figure 5.2: *Small angle X-ray scattering data of concentrated lysozyme solution in concentrations of* 5, 10, *and* 15 *wt.%. Electrostatic screening is induced due to the addition of* 50 *and* 100 *mM NaCl. The calculated SAXS curves are plotted in orange. The SAXS curves were shifted vertically for reasons of clarity. Data published in [Möller et al., 2012].*

$b_2(p, T, c_S)$ can be calculated with eq. 3.71 from the obtained potentials.

5.1 Increasing the ionic strength

In a first step, the SAXS intensities for various temperatures and ionic strengths at atmospheric pressure are discussed. The purpose of these first measurements is to find out how the increasing ionic strength is modulating the scattering signal and how the used model can adapt to these changes.

The influence of an increasing ionic strength on the SAXS data is shown in fig. 5.2 together with the refinements to the data. The scattering intensities of 5, 10, and 15 wt.% lysozyme are depicted, with sodium chloride concentrations of 0, 50, and 100 mM. The corresponding refinements are plotted in orange and calculated by fitting the function

$$I(q) = S_{\text{eff}}(q) \cdot P(q) + c \tag{5.1}$$

to the data. The form factor $P(q)$ is calculated as that of an ellipsoid of revolution, the effective structure factor $S_{\text{eff}}(q)$ is calculated as presented in sec. 4.4, c is a constant added.

A so-called correlation peak can be seen at low ionic strength, most pronounced in the absence of salt for all protein concentrations. This peak is characteristic for the structure factor of strongly repulsive systems. The 2-Yukawa model can successfully be applied for solutions of varying ionic

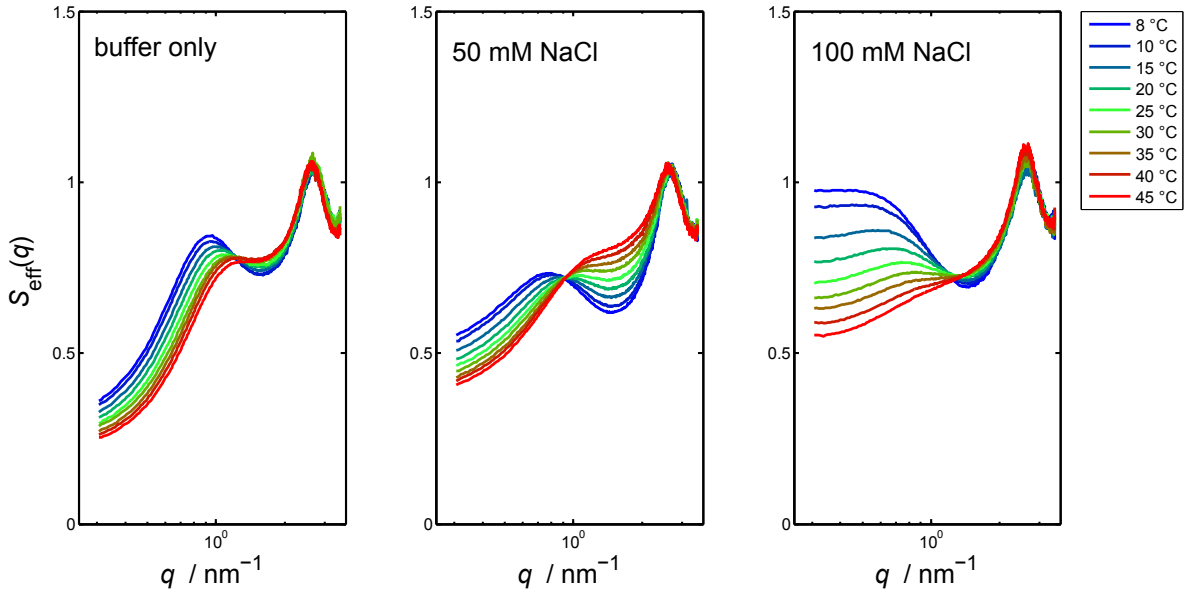

Figure 5.3: *Effective structure factors, $S_{eff}(q)$, at various salt concentrations and temperatures. The lysozyme concentration is 10 wt.%. Picture adapted from [Möller et al., 2012].*

strength and protein concentration, giving refinements with reasonable quality. In the high q-regime, the refinement follows the data points until the minimum in $I(q)$. For larger wave vector transfers q, the calculated curves are below the measured scattering intensities. This is caused by the deviations that have already be seen between the measured and calculated form factor, see fig. 4.10. Changes in the scattering curve due to varying protein or salt concentration are only seen at smaller q values. For this q-range, the model follows the measured data. Especially the position of the correlation peak can accurately be reproduced.

The effective structure factor, $S_{eff}(q)$, of the 10 wt.% lysozyme solution upon addition of different NaCl concentrations is presented in figure 5.3 at different temperatures. The scattering curves are divided by the form factor of lysozyme, calculated by fitting the scattering data of a 0.5 wt.% lysozyme solution with the program GNOM (see sec. 4.4).

Clearly, a drastic increase of attractive interaction between the proteins is seen with increasing ionic strength, indicated by a marked increase of the scattering intensity at small q-values. Furthermore, an increasing attractivity is observed upon a decrease of temperature from 45 to 8 °C. This also results in the disappearance of the well defined correlation peak at $q \approx 1.0$ nm^{-1}. This peak can be seen in the depicted scattering data (fig. 5.2) and the corresponding effective structure factor $S_{eff}(q)$ (fig. 5.3).

A second maximum of the effective structure factor can be seen at $q \approx 2.6$ nm^{-1} in accordance with previous studies. The origin of this maximum in the structure factor is heavily discussed in literature, interpreted as evidence for equilibrium clusters in lysozyme solution [Stradner et al., 2004]. Nevertheless, this interpretation has been strongly debated [Shukla et al., 2008a, Stradner et al., 2008, Shukla et al., 2008b]. Two conclusions can be made from the data in this thesis that disagree with the interpretation of equilibrium cluster. First, the high-q peak is unaffected by changes in temperature and pressure as well as the passing of phase boundaries in the protein sys-

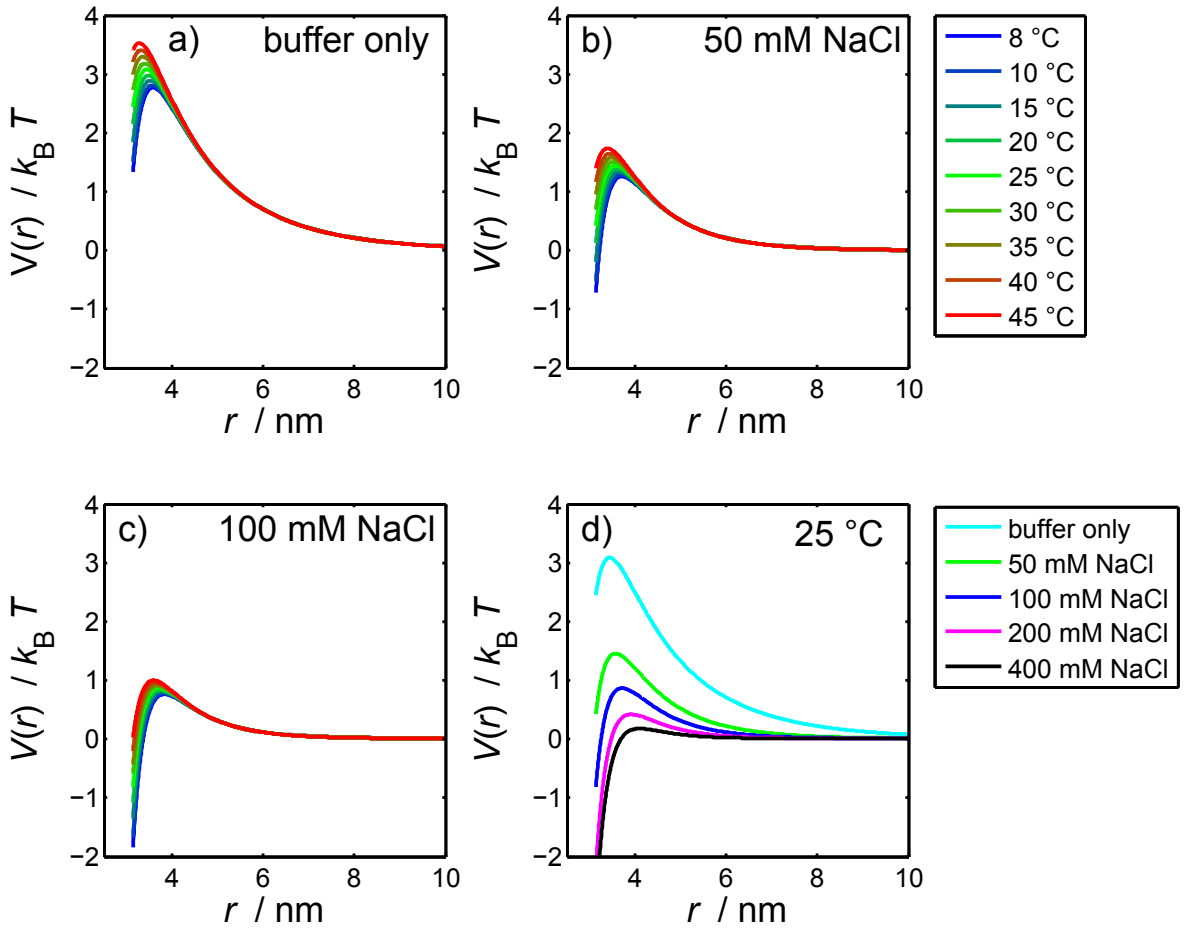

Figure 5.4: *a)-c) Intermolecular interaction potentials obtained from refining the SAXS curves of* 10 *wt.% lysozyme solution with varying NaCl concentration and temperature. d) Interaction potential of* 10 *wt.% lysozyme at* 25° *C with increasing ionic strength. The dominant repulsive interaction can strongly be screened with ions.*

tem (chapter 6), which is hardly to be expected for equilibrium cluster. Furthermore, the position of the peak is the same as the minimum in the form factor, implying that, for example, dividing a constant by the form factor also results in such a peak. Consequently, small differences between the two scattering curves that are divided, that is from diluted and concentrated solution, can result in such a peak. Notably, the scattering intensities of both curves are orders of magnitude smaller at this q-values, which increases the uncertainties in the measured values. Therefore, the occurrence of this peak can probably be explained with a slight mismatch between the scattering curves of diluted and concentrated solutions at those q-values. Also, changes in the effective structure factor are found for $q < 2$ nm^{-1} only, where the scattering can be described by the interactions of monomeric lysozyme molecules [Shukla et al., 2008a]. Those changes will be discussed in the following results of this thesis.

The intermolecular interaction potential $V(r)$ is calculated by refining the model described before to the experimental data with the strength of the attractive interaction, J, being the only free parameter. The resulting interaction potentials are illustrated in fig. 5.4. The protein-protein interaction potentials reflect the behavior of the structure factors, showing a lower repulsive in-

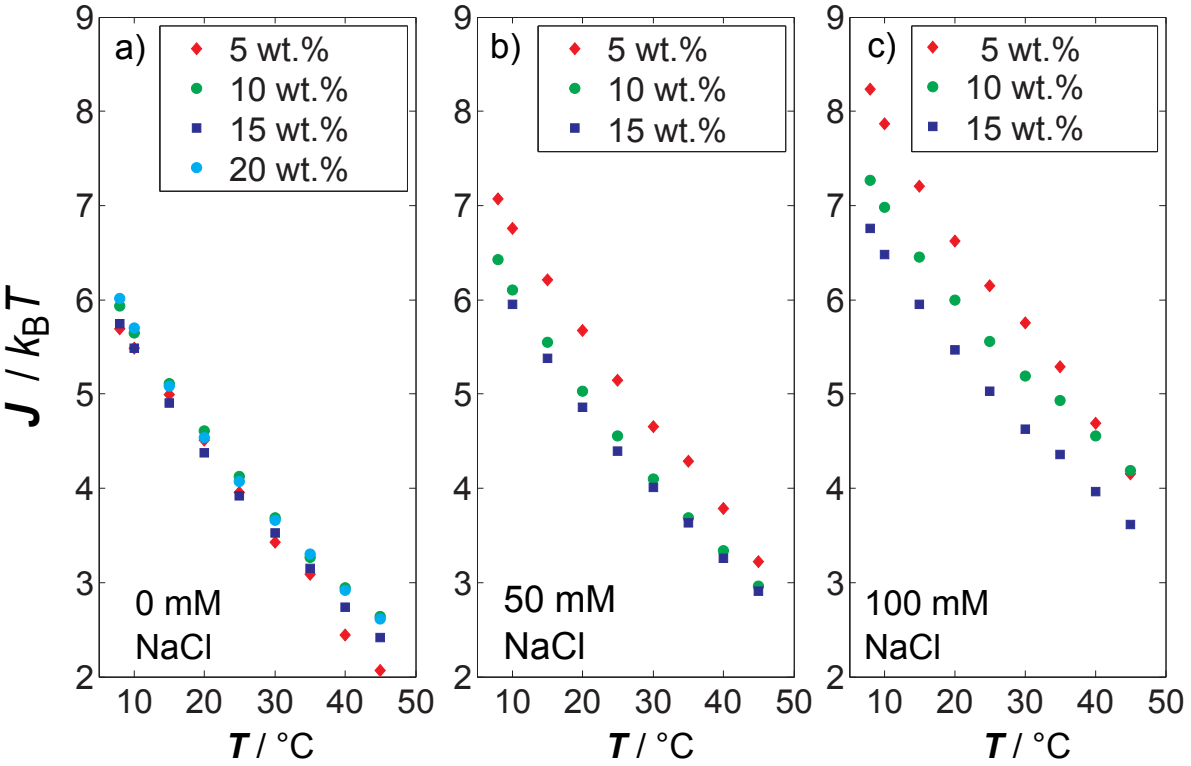

Figure 5.5: *Temperature dependence of the strength of the interprotein attractive interaction, J, as a function of NaCl and protein concentration. Picture published in [Möller et al., 2012].*

teraction for increasing salt concentration and decreasing temperature. Notably, the higher ionic strength influences the interaction potentials much stronger than changes in temperature. In fig. 5.4 d), the obtained interaction potentials are also presented for sodium chloride concentrations up to 400 mM so that the electrostatic repulsion is screened to a huge extent. It can thus be concluded that the increase in ionic strength for salt concentrations up to 100 mM already screens the main part of the repulsive interactions; above 400 mM the repulsive contributions of the Coulomb repulsion can in principle be neglected.

Despite the repulsive, screened Coulomb part of the potential, the attractive part was also found to be a function of salt concentration and temperature, which is presented in fig. 5.5. A clear temperature dependence of the attractive interaction is observed for all salt concentrations. Reducing the temperature leads to an increase of the attractive protein-protein interaction. This behavior is in agreement with the observation of a liquid-liquid phase separation or aggregation of potein solutions upon cooling (see sec. 2.3).

The attractive interaction is found to be independent of the protein concentration under salt-free conditions only. With increasing ionic strength of the solution, an increase of the protein concentration reduces the attractive interaction parameter, J. Furthermore, with higher protein concentrations, intermolecular distances decrease, thus, leading to a more pronounced effect of charge screening on $V(r)$ and hence J.

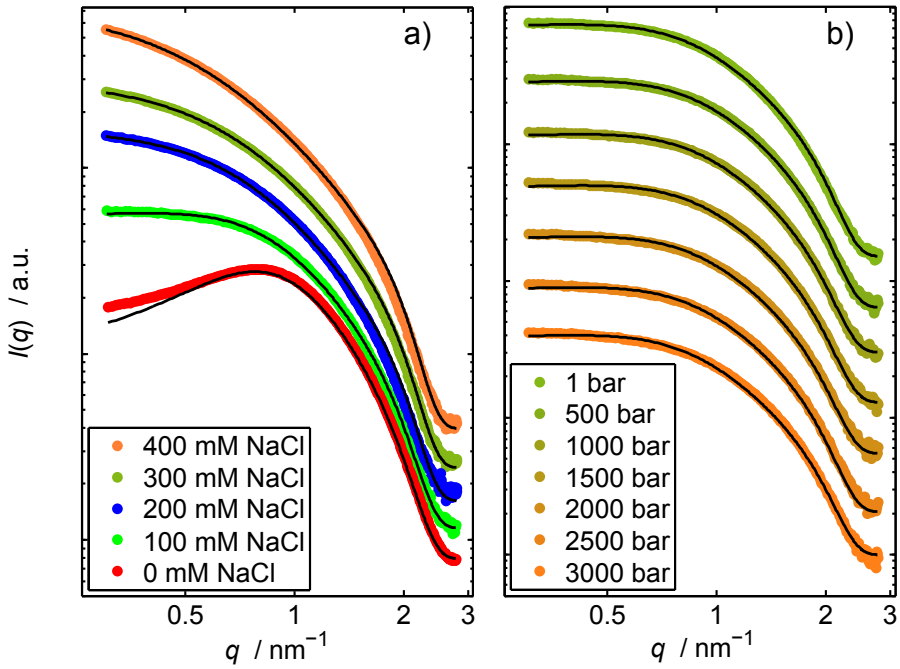

Figure 5.6: *Scattering curves of 10 wt.% lysozyme solution measured at different ionic strengths and hydrostatic pressures. Refinements to the data are plotted in black. The intensities are shifted vertically for reasons of clarity.*

5.2 Non-linear pressure dependence

As a next step, the effect of increasing pressure on the intermolecular interaction potentials is investigated. This has been analyzed before in solutions of very low ionic strength, i.e. buffer only [Schroer et al., 2011a]. In that work, a non-linear pressure dependence was found (see also sec. 2.5) that is probably governed by marked changes in the local water structure upon pressure increase (sec. 2.6). The influence of additional salt ions in the solution has never been considered yet. As different salts can strongly influence the local water structure (sec. 2.7), the pressure dependence of the interaction potential in solutions of high ionic strength is far from trivial. First, the salt sodium chloride is used because it is located in the middle of the Hofmeister series, having neither strong kosmotropic nor chaotropic properties. Specific ion effects will be discussed later on in sec. 5.4.

The measured SAXS curves for different ionic strengths at atmospheric pressure are illustrated in fig. 5.6 a) and for increasing pressure at an ionic strength of 100 mM in fig. 5.6 b). The refinement of the data with the structure factor of the 2-Yukawa interaction potential yields J. The pressure dependence of J for varying protein concentrations and temperatures is shown in fig. 5.7 a) and b). The influence of increasing ionic strength is depicted in fig 5.7 c). Clearly, the non-linear behavior of the interaction strength as a function of pressure is visible in all solution conditions studied. The interaction potentials become more repulsive with increasing pressure up to a pressure of $1.5-2$ kbar. From there on, the strength of the attractive interaction increases, causing a minimum of $J(p)$ at around $1.5-2$ kbar. This non-linear dependence of the attractive

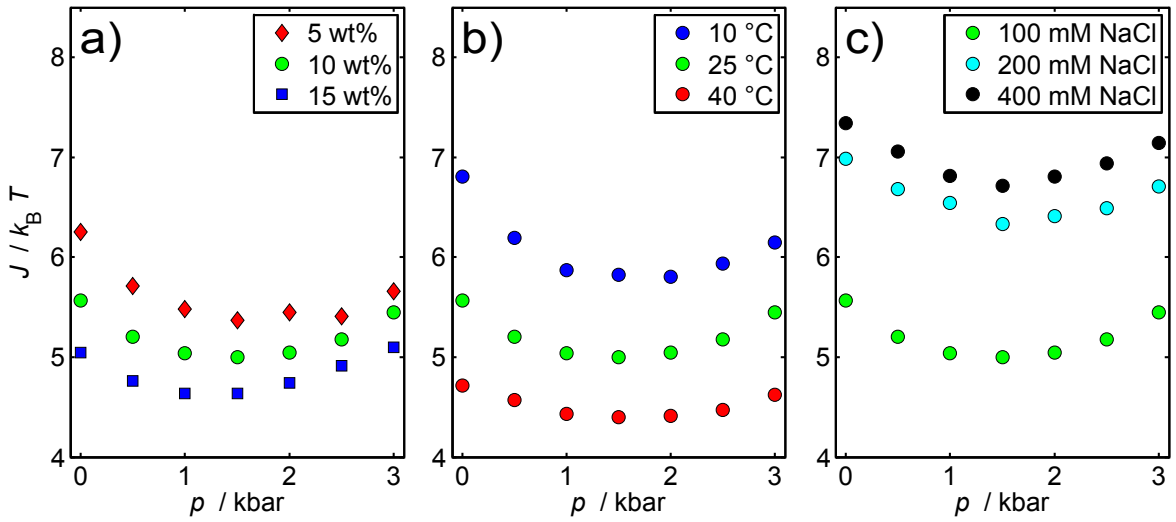

Figure 5.7: *Results of the refinement for $J(p)$ as a function protein concentration (25 °C, 100 mM NaCl) (a) and temperature (10 wt.% Lys, 100 mM NaCl) (b). (c) Strength of the attractive interaction, J, for different NaCl concentrations ranging from 100 mM (bottom) to 400 mM (top) NaCl (10 wt.% Lys, 25 °C). $J(p)$ for 10 wt.%, 25 °C, 100 mM NaCl, is plotted in a, b, and c (green). Data published in [Möller et al., 2012].*

interaction strength J on pressure is in agreement with the behavior found for salt free buffer solutions [Schroer et al., 2011a], displaying also a broad minimum around $1.5 - 2$ kbar. This behavior was attributed to changes in the local structure of water upon compression that changes alongside with different further properties of water in this pressure range. A short discussion is given in sec. 2.6. The hypothesis that structural changes in the aqueous solvent are responsible for this non-linear pressure dependence is supported by the fact that the position of the minimum can be influenced by water structuring cosolvents like TMAO [Schroer et al., 2011b].

Nevertheless, the increasing ionic strength was found to have no effect on the pressure dependence of J. Only an increase in attractivity is noted to higher salt concentrations, which has also been observed at atmospheric pressure conditions (fig. 5.5). Therefore, it can be stated that the influence of sodium chloride on the interactions under pressurized solution conditions is only due to charge screening and no influences on the water structure can be assumed. This finding is in line with the empirical Hofmeister series, locating sodium and chloride ions in the central part (fig. 2.15) with neither marked structure making nor breaking properties.

Small changes in the pressure dependence seem to occur as a function of protein concentration (fig. 5.7 a)), whereas the location of the minimum in $J(p)$ is independent of temperature (fig. 5.7 b)). J values decrease by $\sim 30\%$ upon an increase of temperature from 10 to 40 °C. Additionally, the pressure dependence is more pronounced at 10 °C compared to 40 °C. In order to quantitatively characterize the interaction strength, the second virial coefficient $b_2(p, T)$ is calculated from the obtained interaction potentials.

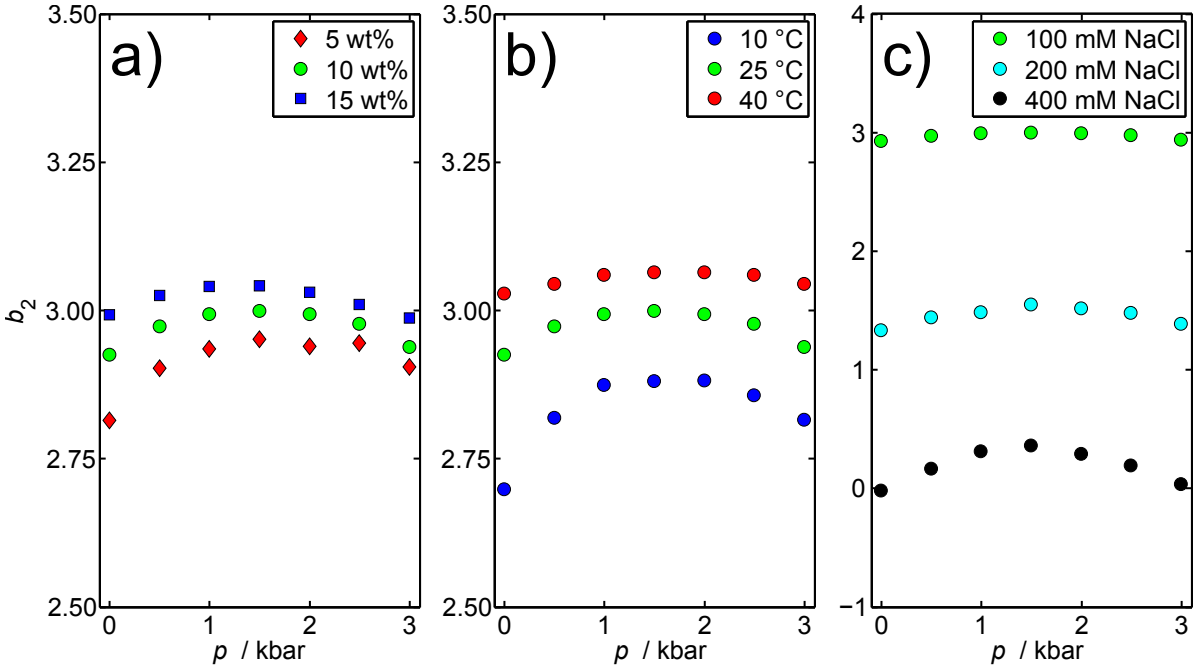

Figure 5.8: *Results of the refinement for b_2 as a function of protein concentration (25 °C, 100 mM NaCl) (a) and temperature (10 wt.% Lys, 100 mM NaCl) (b). (c) b_2 for different NaCl concentrations ranging from 100 mM (top) to 400 mM (bottom) NaCl (10 wt.% Lys, 25 °C). b_2 for 10 wt.%, 25 °C, 100 mM NaCl, is plotted in a, b, and c (green).*

5.3 Second virial coefficient

The pressure and temperature dependence of the normalized second virial coefficient $b_2(p, T)$ can be calculated from the measured interaction potentials. For details of the calculation, see sec. 4.4. In order to understand the occurrence of liquid-liquid phase separation areas in the phase diagram, the dependence of b_2 on external parameter is of strong interest. Furthermore, suitable crystallization slots lie in a narrow range of b_2 values [George and Wilson, 1994]. This slot appears for b_2 values typically between $\sim$ -0.85 and -3.2 [Poon et al., 2000].

In fig. 5.8 the obtained values for b_2 are shown. Note that the strength of the repulsive Coulomb interactions is included in the calculation of b_2, so that the increasing ionic strength has the strongest impact on the absolute values of b_2. Nevertheless, the contribution of the non-linear pressure dependence to J can clearly be seen in b_2. To compare the combined influence of temperature and pressure, $b_2(p, T)$ is plotted for a salt concentration of 100 mM NaCl in fig. 5.9. The $b_2(p, T)$ values rise monotonically with higher temperature, but display a maximum at a pressure of $\sim$ 2 kbar. As expected, the non-linear pressure dependence of $V(r)$ is also reflected in $b_2(p, T)$: At pressures up to 2 kbar, an increase of pressure results in an increase of b_2, meaning the interaction between the molecules becomes less attractive. For pressures higher than $\sim$ 2 kbar, b_2 decreases again. Additionally, the change of b_2 with increasing pressure is much stronger at low temperatures, resulting in a more pronounced maximum of $b_2(p)$ compared to temperatures as high as 40 °C at which a broad maximum is observed. This temperature and pressure dependence is fundamental for the resulting phase behavior of the protein solution. A

monotonically decreasing temperature results in a liquid-liquid phase separation below a certain temperature, which is in line with observed phase diagrams, see fig. 2.7. The influence of pressure has a non-linear effect, the resulting phase diagram will be studied in chapter 6.

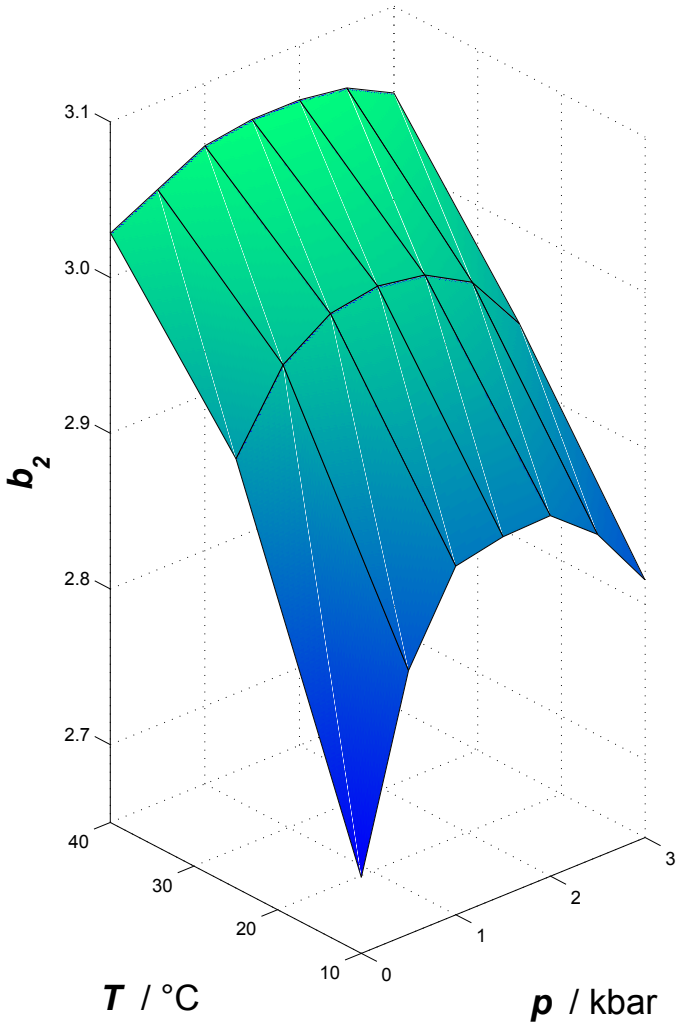

Figure 5.9: *Normalized second virial coefficient, $b_2(p, T)$, for 10 wt.% lysozyme in 100 mM NaCl solution. Picture published in [Möller et al., 2012].*

The observed pressure dependence of the second virial coefficient is in good agreement with recent observations by Crisman and Randolph [Crisman and Randolph, 2010]. They studied the crystallization behavior of recombinant human growth hormone at elevated pressure and found a higher virial coefficient at a pressure of 2500 bar compared to atmospheric pressure. Consequently, they observed crystal growth under high pressure at solution conditions that formed amorphous precipitates at atmospheric pressure only, and detected no crystal growth under high pressure at solution conditions that produced crystals at 1 bar. In that study, poly(ethylene glycol) was applied as crystallization agent. In agreement with the results presented in this chapter,

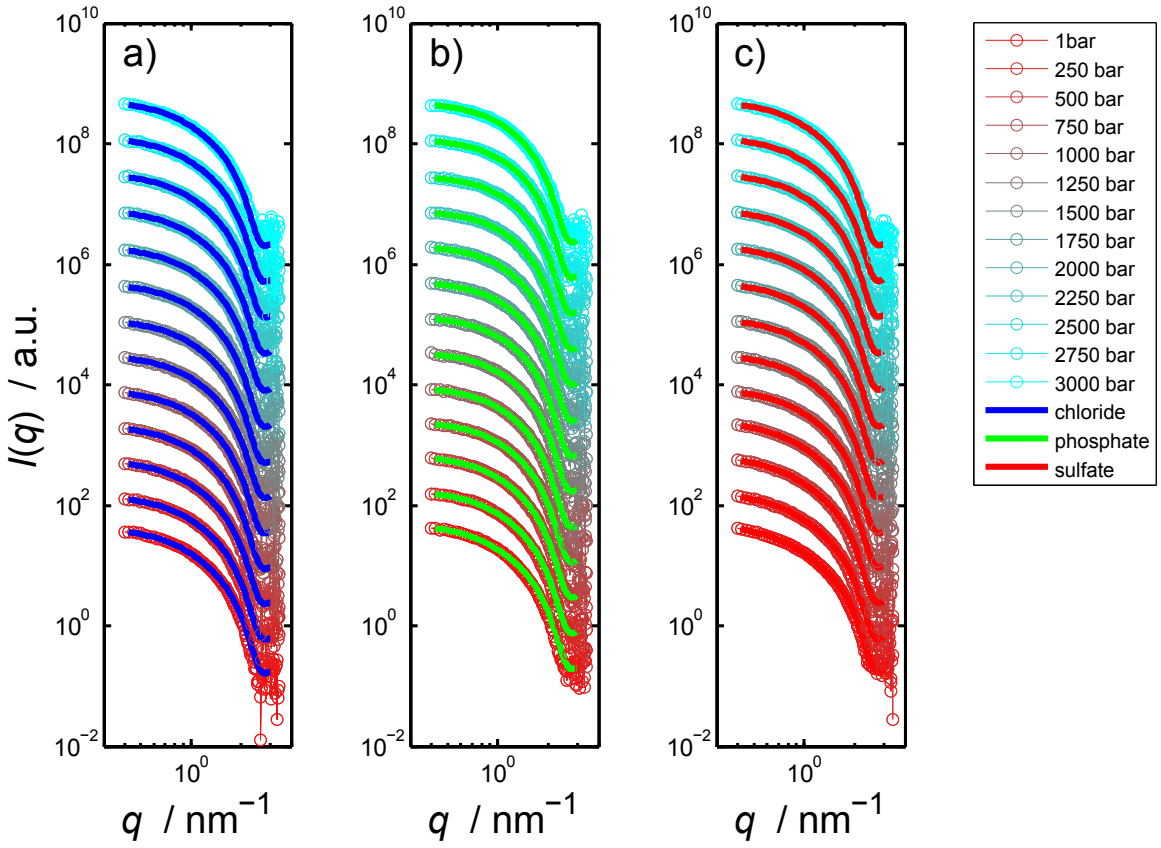

Figure 5.10: *Scattering data for a 5 wt.% lysozyme solution at $T = 25\,°C$ as a function of pressure and salt anion type: a) chloride, b) phosphate, and c) sulfate. The ionic strength of all samples is 250 mM. The blue, green, and red lines present the refinements of the data. Picture published in [Möller et al., 2014b].*

an increase of the second virial coefficient was found from 1 bar to 2500 bar in this study.

5.4 Specific anion effects

So far, the protein interactions in solutions of high ionic strength were found to have the same principle pressure dependence as in pure buffer solution, and the influence of the added ions was reduced to the Debye-Hückel charge screening effect. The observed effect of sodium chloride is in line with its location in the middle of the Hoffmeister series. Nevertheless, besides screening effects, the interactions have been shown to depend on water structure changes. Therefore, the influence of kosmoptropic ions on the protein-protein interactions at elevated pressure will be discussed in the following.

The pressure dependent scattering data for a 5 wt.% lysozyme solution at an ionic strength of $I = 250$ mM are depicted together with the refinement of the data in fig. 5.10, with a) chloride, b) phosphate, and c) sulfate being the added anions, and sodium the corresponding cation. As the anions have different charges, the ion concentration for sulphate and phosphate differs from the ionic strength of the salt solution. The investigated salts are compared at matching ionic

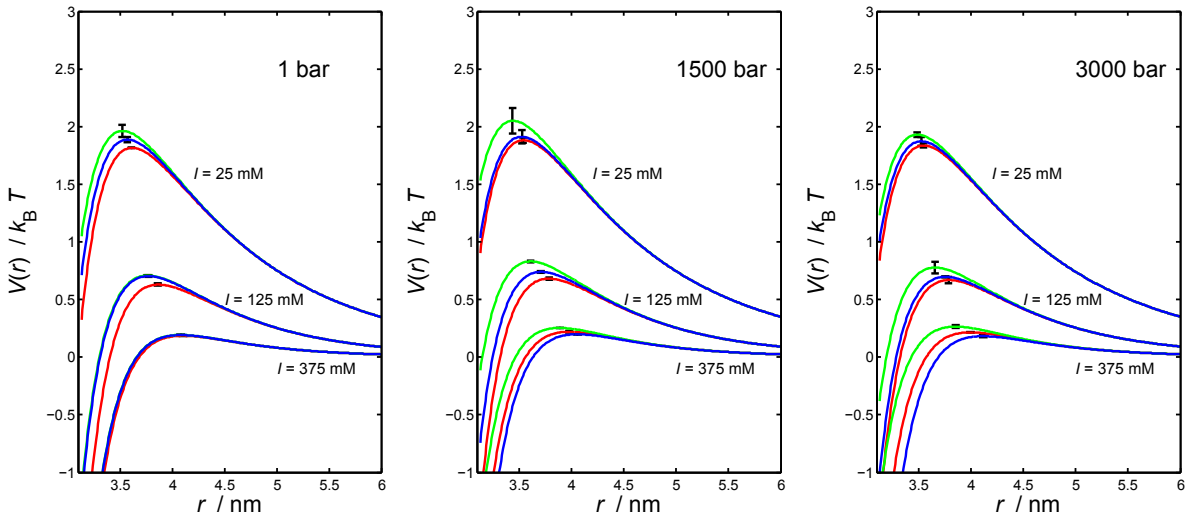

Figure 5.11: *Intermolecular interaction potentials for* 5 *wt.% lysozyme under pressures of* 1, 1500, *and* 3000 *bar at different salt types and concentrations(blue: chloride, green: phosphate, red: sulfate). Picture published in [Möller et al., 2014b].*

strengths in the following to have the same screening contributions (see sec. 4.4). The interaction potentials are calculated from the refinements to the data.

In fig. 5.11, the overall protein-protein interaction potentials $V(r)$ are plotted for ambient and elevated pressure. The data have been obtained by averaging over the results measured at two different beamlines, namely I22 and ID02. At the maximum value of each $V(r)$ curve, the calculated standard deviations are also shown as representative error bars. For low ionic strengths, at which small differences in the salt concentrations can have a strong effect on $V(r)$ (compare fig. 5.4 d)), error bars are slightly larger. The different colors correspond to the different anions and are marked as before.

The obtained changes in the interaction potentials reflect the increasing electrostatic screening at higher salt concentrations. At low ionic strengths, a distinct maximum of $V(r)$ appears at ~ 3.8 nm. At an ionic strength of $I = 375$ mM, the strong repulsive part has almost completely vanished due to the strong screening of the surfaces charges. These observations are in good agreement with the measurements presented in sec. 5.2. However, differences between the salt types can be identified, being more pronounced at higher pressure. For low ionic strength, no drastic differences in the pressure dependence between the three salt solution are visible. Minor deviations may be within the range of experimental error and are also independent of the increasing pressure.

Marked differences in the pressure dependence between sulfate and phosphate ions on the one hand, and chloride ions on the other hand can be identified at higher ionic strengths. This effect is most pronounced at an ionic strength of $I = 375$ mM. At this ionic strength, the interaction potentials are similar at ambient pressure for all three anions, but differ strongly at high hydrostatic pressure.

The influence of salt type and pressure on the interaction potentials can also be noted in fig. 5.12. The b_2 values for the three different anions types are depicted as a function of ionic strength at

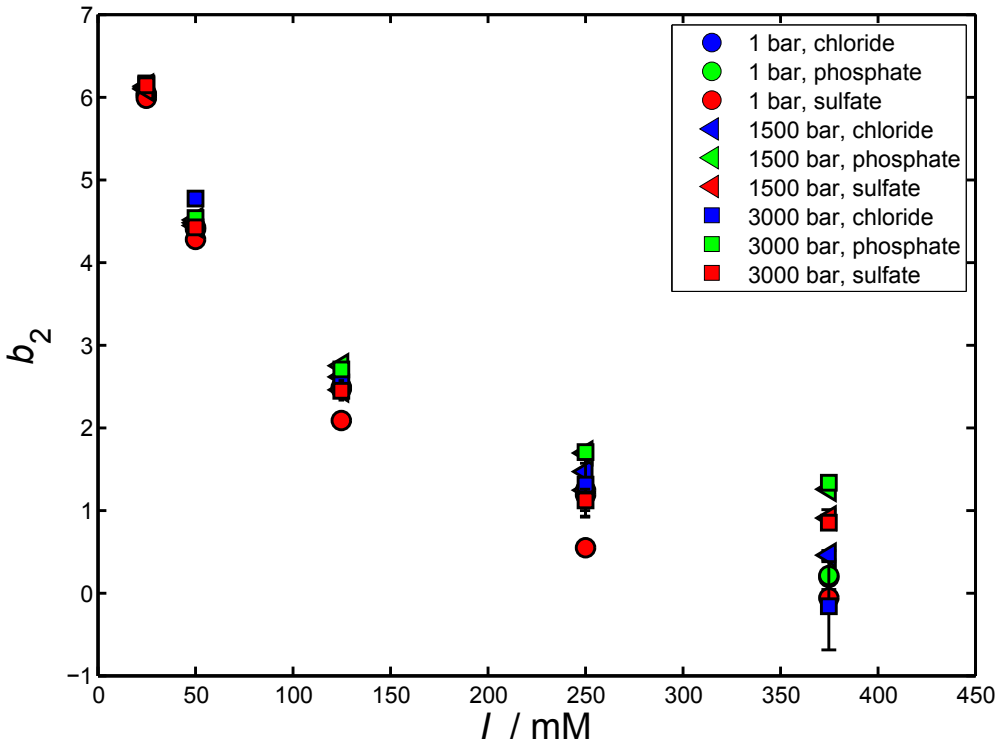

Figure 5.12: *Normalized second virial coefficient b_2 as a function of ionic strength. As illustrated, the influence of pressure and salt type becomes more pronounced with increasing pressure. Picture published in [Möller et al., 2014b].*

pressures of 1, 1500, and 3000 bar. Generally, the strength of the repulsive interaction between the proteins and hence b_2 decreases with increasing salt concentration. At low ionic strengths of $I = 25$ mM, variations of the salt type and higher pressure have only a minor effect on the interaction potential. Conversely, at high ionic strength, differences in the b_2 values increase, owing to a strong dependence of the protein-protein interaction potentials on the anion type.

In order to analyze the pure pressure dependence in more detail, only the strength of the attractive part of the interaction potential, $J(p)$, is presented in fig. 5.13. Here, the differences between the J-value at pressure p and the value at 1 bar are plotted, thus omitting differences in J-values at ambient pressures.

The exact course of the protein-protein interaction strength as a function of pressure is strongly influenced by the type of anion in the solution. Compared to the salt free (pure buffer) solution, small deviations in $J(p)$ can be found for NaCl only at very high ionic strengths. Here, the pressure dependence tends to be less pronounced. Nevertheless, the position of the minimum of $J(p)$ stays essentially constant over the entire salt concentration range. This finding supports the interpretation that the addition of sodium chloride only results in a screening of the repulsive part of the interaction potential, but the pressure dependence stays basically unaffected (sec. 5.2).

In contrast, an increasing influence on the protein-protein interaction potential is observed in the presence of the multivalent ions. While sulfate and phosphate have a similarly small impact on the interaction potential at ionic strengths of $I = 25$ and 50 mM, their influence increases at higher concentrations. The minimum in $J(p)$ is shifted to higher pressures for both kosmotropic anions,

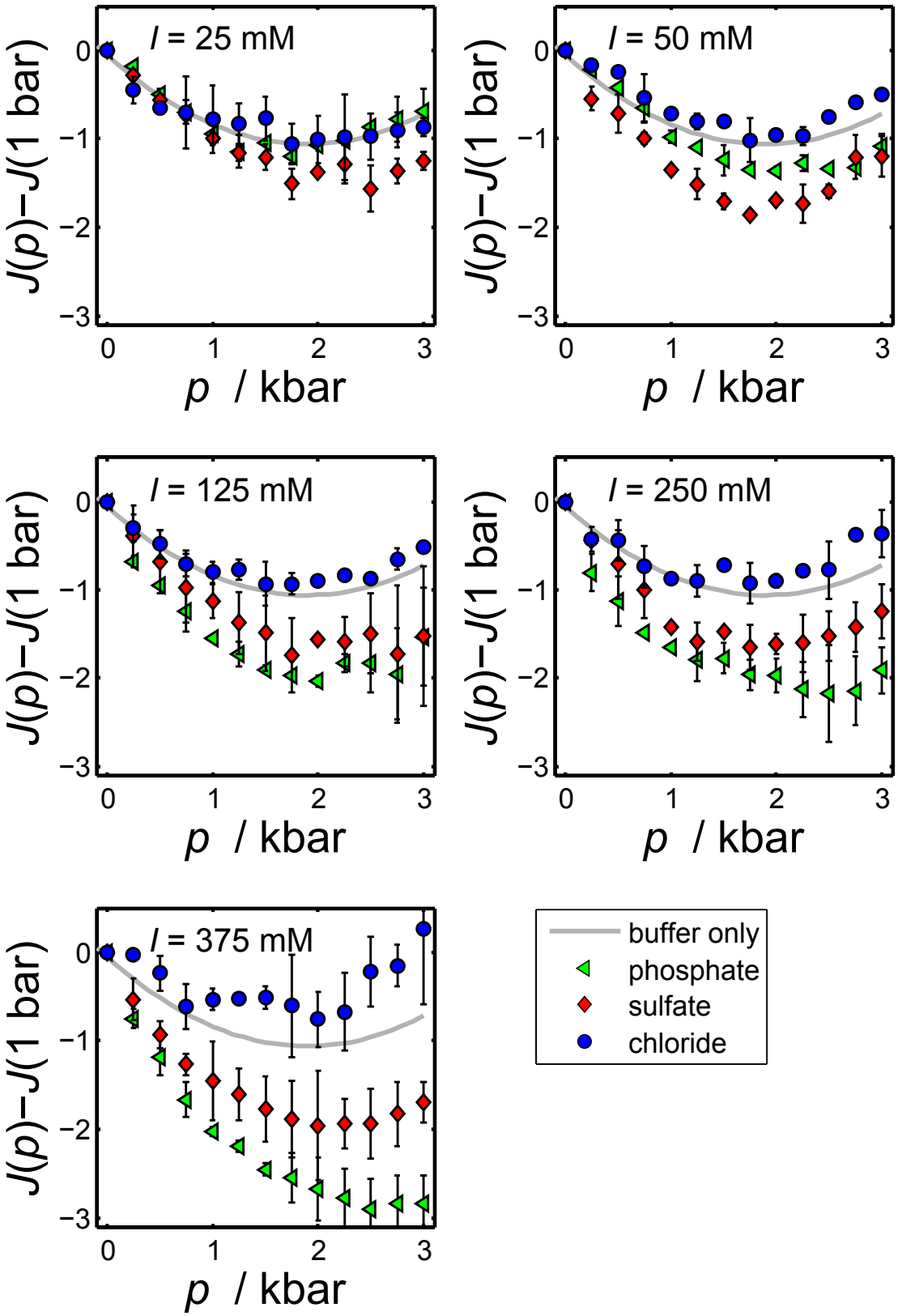

Figure 5.13: *Pressure dependence of the attractive strength, $J(p)$, of the protein-protein interaction potential. The pressure dependence of $J(p)$ of salt free (buffer only) lysozyme solutions is shown in gray. Picture published in [Möller et al., 2014b].*

owing to a counteraction effect of the kosmoptropic anions on the pressure perturbation of the water structure. This finding is congruent with the observed influence of TMAO on the pressure dependent protein interactions [Schroer et al., 2011b], but with the addition of the electrostatic screening.

Because the intermolecular protein-protein interaction potential is expected to be strongly influenced by the solution conditions, the cause for the ions' effects on the interactions should be founded in the combined influences of ions and pressure on the local water structure. An experimental measure for the strength of ion-water interactions[1] is the Jones-Doyle viscosity coefficient, B, with $B > 0$ displaying an increase in viscosity due to a strong hydration of the ions [Marcus, 2009]. Consequently, values with $B < 0$ correspond to weakly hydrated ions that result in a decreased viscosity. Regarding the studied anions, the strongest effect is expected for phosphate (PO_4^{3-}: B = 0.590, HPO_4^{2-}: B = 0.382, SO_4^{2-}: B = 0.206, Cl : B = -0.005, Na^+: B = 0.085) [Jenkins and Marcus, 1995]. Several theoretical studies addressed the solvation of different anions and their influence on the local water structure. For example, it has been shown that the PO_4^{-3} anion is strongly hydrated, with each oxygen of the phosphate forming on average three hydrogen bond to different solvent molecules, leading to a first hydration shell with about 13 water molecules [Pribil et al., 2008]. In general, kosmotropic ions are found to be strongly hydrated [Ohtaki and Radnai, 1993, Marcus, 2009, Collins, 2004], in resemblance for example to TMAO [Zou et al., 2002, Bennion and Daggett, 2004, Street et al., 2006].

Experimental or theoretical studies on the combined influence of ions and pressure on the water structure in the investigated pressure range are rarely found, however. In the case of SO_4^{2-}, an enhancement of the hydrogen bonding network was found [Mantegazzi et al., 2012], in agreement with theoretical results from *ab initio* quantum mechanical charge field molecular dynamics simulations [Vchirawongkwin et al., 2007]. This is in line with the effect found for sulfate ions on the pressure dependence of $J(p)$, i.e. counteracting the effect of pressure and therefore shifting the minimum in $J(p)$ to higher pressures. Further experimental or theoretical works concerning pressure effects on ion hydration and the local water structure are studying either very specific ions or pressure and temperature ranges beyond bio-physiological relevance [Filipponi et al., 2003, Galamba, 2013, Migliorati et al., 2013]. In this framework, further studies are needed that address ion solvation under high pressure conditions.

5.5 Summary

The presented high pressure SAXS studies on concentrated lysozyme solutions reveal the dependence of the protein-protein interaction potential on temperature and pressure as well as concentration and type of salt added. Systematic investigations were conducted on a wide range of different parameters, determining the second virial coefficient $b_2(p, T, c_S)$ extracted from modeling the SAXS data with a liquid state theoretical approach. A systematic representation of the results is depicted in fig. 5.14.

[1] Normalized on the strength of water-water interactions in bulk solution.

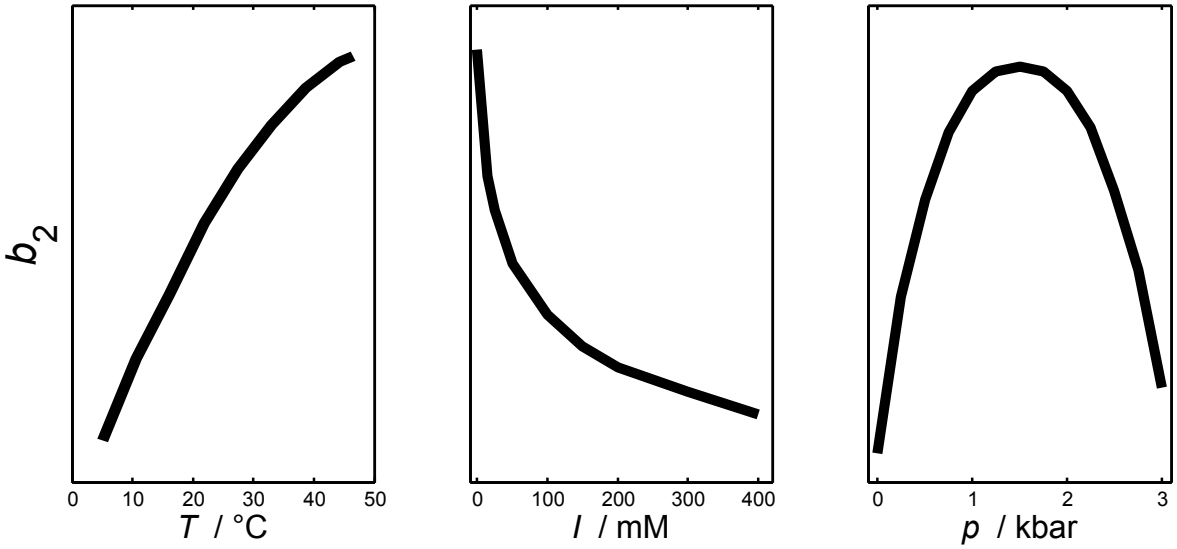

Figure 5.14: *Principle dependence of b_2 on temperature, ionic strength, and pressure as revealed by the SAXS analysis.*

A monotonic dependence on temperature and ionic strength was found in accordance to previous studies [Bonneté et al., 1999, Sedgwick et al., 2007, Gögelein et al., 2012, Chinchalikar et al., 2013] and the phase diagram for concentrated protein solutions.

The non-linear pressure dependence found in pure buffer solution is also present in solutions of high ionic strength, showing that the presence of ions does not in general change the pressure dependent behavior. A specific ion effect was found, however, which can significantly influence this pressure dependence, depending on the type of ion. The markedly different b_2 dependence on the investigated parameters can be used to precisely tune the intermolecular interaction potentials and therefore the resulting phase behavior. Notably, the absolute changes in b_2 are only small as a function of pressure, especially compared to the effect of increasing ionic strength. This can be explained with the strong influence of the Coulomb repulsion on the intermolecular interaction potential, which is screened by ions but has hardly any dependence on pressure. However, it was shown that at higher ionic strength, the effect of high pressure becomes considerably stronger. This fact can be used to fine tune intermolecular interaction potentials of proteins by pressure modulation.

Furthermore, the specific anion effect on the observed non-linear pressure dependence may serve as a next step to explain this striking pressure dependence of $J(p)$. It can be concluded that the kosmotropic osmolyte TMAO [Schroer et al., 2011b] and the kosmotropic anions sulfate and phosphate similarly shift the minimum in $J(p)$ to higher pressures. In contrast, chloride anions and the chaotropic osmolyte urea [Schroer et al., 2011b] are found to have negligible influence on the pressure dependence. Further studies are needed to understand the molecular mechanism that govern this marked pressure dependence.

6 High Pressure Liquid-Liquid Phase Separation

The phenomenon of liquid-liquid phase separation (LLPS) in protein solutions will be discussed in this chapter. A short introduction to LLPS can be found in sec. 2.3. Characteristic for solution conditions that promote protein crystallization is their close location to the phase boundary of the LLPS region in the phase diagram of dense protein solutions. Therefore, knowledge on the exact shape of the separating phase boundary between LLPS phase and homogeneous phase is desired.

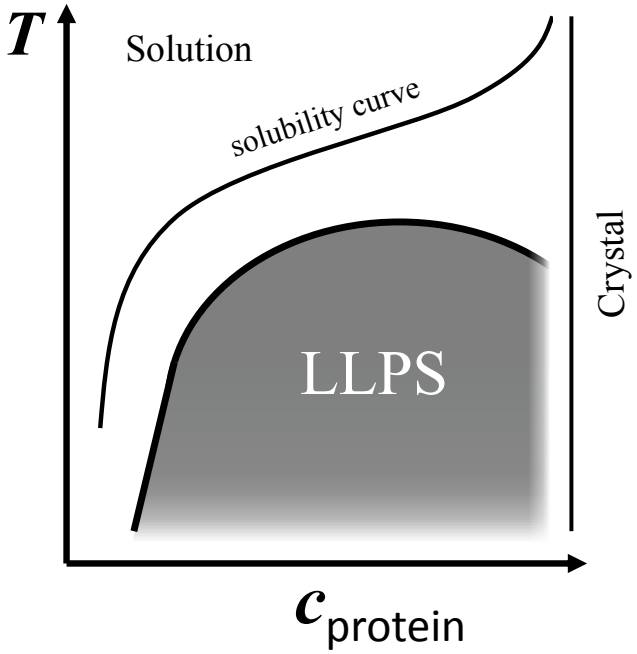

Figure 6.1: *Schematic temperature-concentration phase diagram of dense protein solution. A transition to a (metastable) liquid-liquid phase separation region (LLPS) occurs at lower temperatures than the separation between the solution and solid (crystal) phase. The picture is published in [Möller et al., 2014a].*

The temperature-concentration phase diagram of dense protein solution is depicted in fig. 6.1. A metastable LLPS phase forms for temperatures below the binodal line (area marked in gray), making the solution opaque for visible light. The exact location of the binodal is a function of salt concentration [Broide et al., 1996] as an increasing salt concentration lowers b_2. Many studies have addressed the location of the binodal line, investigating the impact of salt type and con-

centration or additional crowders [Broide et al., 1996, Muschol and Rosenberger, 1997, Zhang et al., 2012b]. However, nothing is known about pressure effects on the LLPS of dense proteins solutions so far.

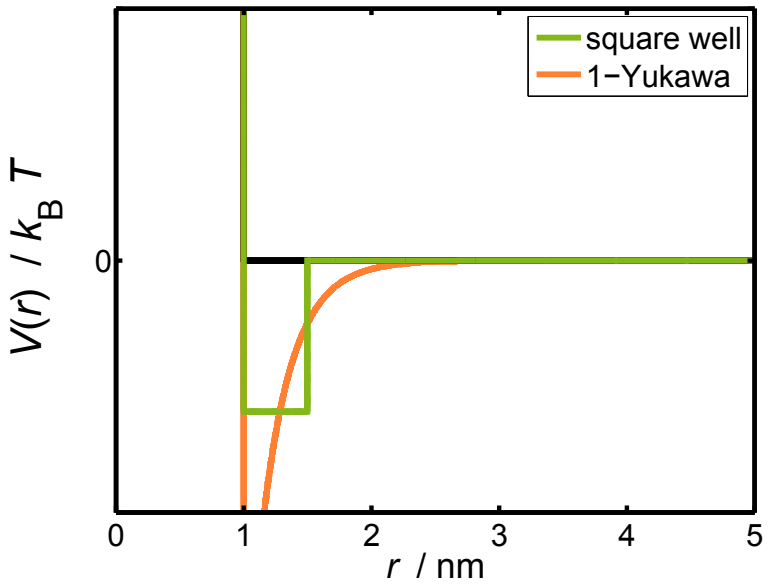

Figure 6.2: *Comparision of the attractive 1-Yukawa potential and the square well potential. The sticky hard sphere potential used is an adapted square well potential. The refinement is described in sec. 4.4.*

As described before, a value of the second virial coefficient $b_2(p,T) \lesssim -1.5$ is considered as prerequisite for a solution to form a LLPS phase [Vliegenthart and Lekkerkerker, 2000, Noro and Frenkel, 2000]. Considering the monotonic temperature dependence of b_2, which was presented in chapter 5, a certain phase separation temperature for a dense protein concentration can exist. Below this temperature, $b_2 < -1.5$ and the LLPS phase forms, for higher temperatures, the solution is in the homogeneous phase. Additionally, hydrostatic pressure has also been found to influence the second virial coefficient b_2.

The experiments presented in this chapter aim to investigate the combined influence of temperature and pressure on the phase diagram of dense lysozyme solution. All investigated samples consist of buffer solution with 500 mM NaCl and lysozyme in concentrations of 18.5, 20.0, and 21.5 wt.%. The sample preparation is described in sec. 4.3. The samples were cooled to different temperatures in the range from 5 to 26 °C and pressure was increased from 1 bar up to 3 kbar. Data were taken in steps of 100 or 250 bar. The presented results were published in [Möller et al., 2014a].

Two different models are used to refine and analyze the data. An Ornstein-Zernicke analysis of the scattering data has been carried out, to investigate, if a phase boundary of the liquid-liquid phase separated state was crossed. In order to investigate the behavior of the second virial coefficient as a function of the applied thermodynamic parameters, the scattering data was also refined using a sticky hard sphere potential to model the intermolecular interaction potential. A sketch of an attractive square well potential is given in fig. 6.2. The sticky hard sphere potential results as

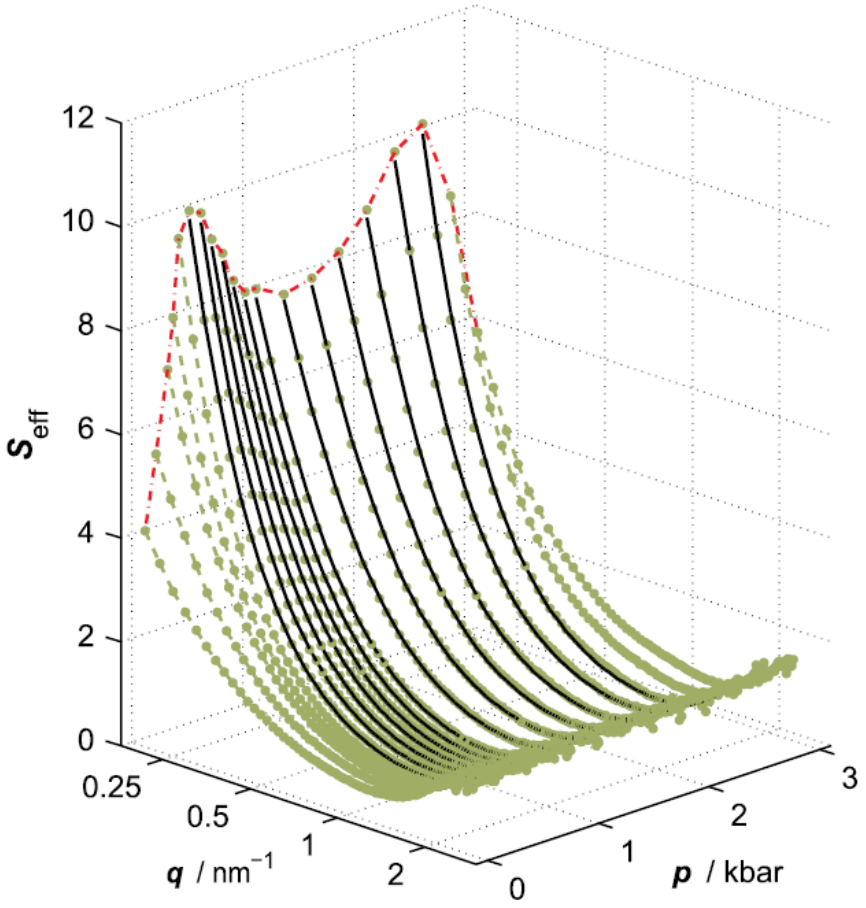

Figure 6.3: *Effective structure factor $S_{eff}(q)$ at a 20 wt.% lysozyme solution as a function of pressure at $T = 16°C$. Black lines display the refinement of the data using the sticky hard sphere model, the red line shows the scattering intensity at $q = 0.2$ nm^{-1}. The picture is published in [Möller et al., 2014a].*

limit for an infinitesimal short ranged and infinite deep potential. The corresponding refinement parameter is the stickiness parameter τ, from which the normalized second virial coefficient b_2 can be calculated (see sec. 4.4).

6.1 Reentrant LLPS at elevated pressure

The effective structure factors obtained from the measurements as a function of increasing pressure are shown in fig. 6.3 for a sample that contained 20 wt.% lysozyme at a temperature of $T = 16\,°C$. Note that the sample is in the phase separated state at 1 bar. The highest scattering intensities at small q are observed at pressures of 400 and 2500 bar, respectively, where the sample crosses the phase boundary out of the LLPS into the homogeneous one-phase region and vice versa at higher pressures. The black lines are the refinements made with the sticky sphere model, discussed in sec. 6.2.

The pressure dependence of the scattering intensity at small q is indicated by a red line in fig. 6.3, located at $q = 0.2$ nm^{-1}. The values for $S_{eff}(q = 0.2\text{ nm}^{-1})$ are additionally depicted in

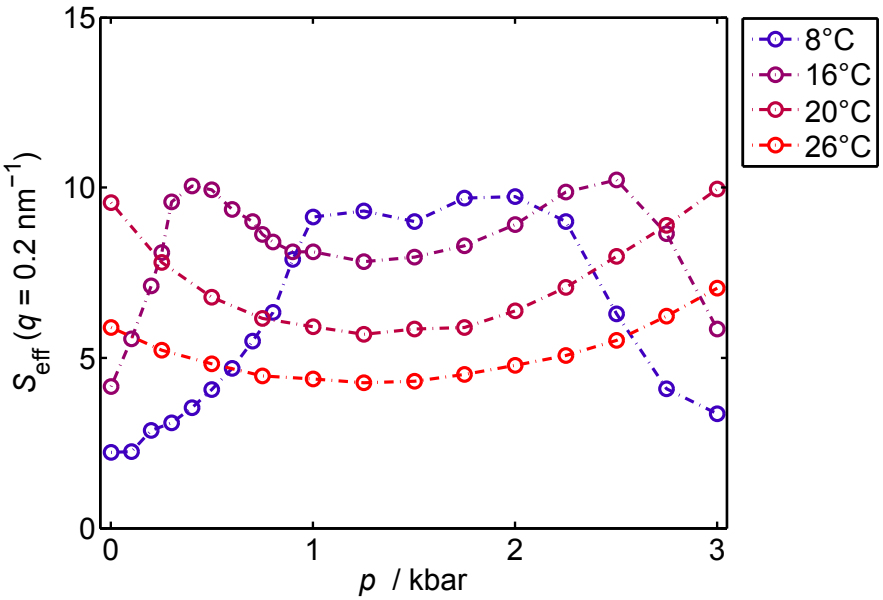

Figure 6.4: *Pressure dependence of the effective structure factor $S_{\text{eff}}(q)$ at $q = 0.2$ nm^{-1} for 8, 16, 20, and 26 °C. Figure adapted from [Möller et al., 2014a].*

fig. 6.4, together with plots for $T = 8$ °C, 20 °C, and 26 °C. SAXS measurements were taken in 2 °C steps, for reasons of clarity only selected temperatures are presented.

In concentrated protein solution, the forward scattering $S(0)$ is an indicator for the type and strength of the intermolecular interactions. As the forward scattering is not accessible in the experiment, the values of $S_{\text{eff}}(q = 0.2\ \text{nm}^{-1})$ are used. With this, two different types of pressure dependences can be distinguished in the depicted case. At 20 and 26 °C , the samples are above the phase separation area marked in fig. 6.1. The forward scattering is a non-linear function of pressure, in line with the observations described in chapter 5. Furthermore, the samples stay in the homogenous, one-phase state over the entire pressure range.

A different pressure dependence is observed for samples that are in the phase separated state at 1 bar. This is the case for temperatures of $T = 8$ and 16 °C. Distinct maxima can be found in $S_{\text{eff}}(q = 0.2\ \text{nm}^{-1})$ as a function of pressure, which indicate the transition from one phase state into another. Passing of the phase boundary is indicated by an increase in forward scattering until a certain maximum value is reached (400 bar at 16 °C, 1000 bar at 8 °C). From there on, the samples are in the homogeneous, one-phase state and show the same non-linear pressure dependence as the samples at 20 °C and 26 °C. At higher pressures, a second maximum in $S_{\text{eff}}(q = 0.2\ \text{nm}^{-1})$ can be found that indicates the reentrance into the LLPS phase.

Keeping in mind the pressure dependence of the protein interaction potential discussed in chapter 5, increasing the hydrostatic pressure from atmospheric conditions should result in an increased repulsive protein-protein interaction and therefore tuning the protein solution out of the liquid-liquid phase separated state. The reversed effect of pressure on the protein-protein interaction potential found at higher pressures should consequently tune the sample back into the LLPS region. The observed phase behavior is consistent with these observations.

To verify the repeated crossing of the phase boundary of the liquid-liquid phase transition, an

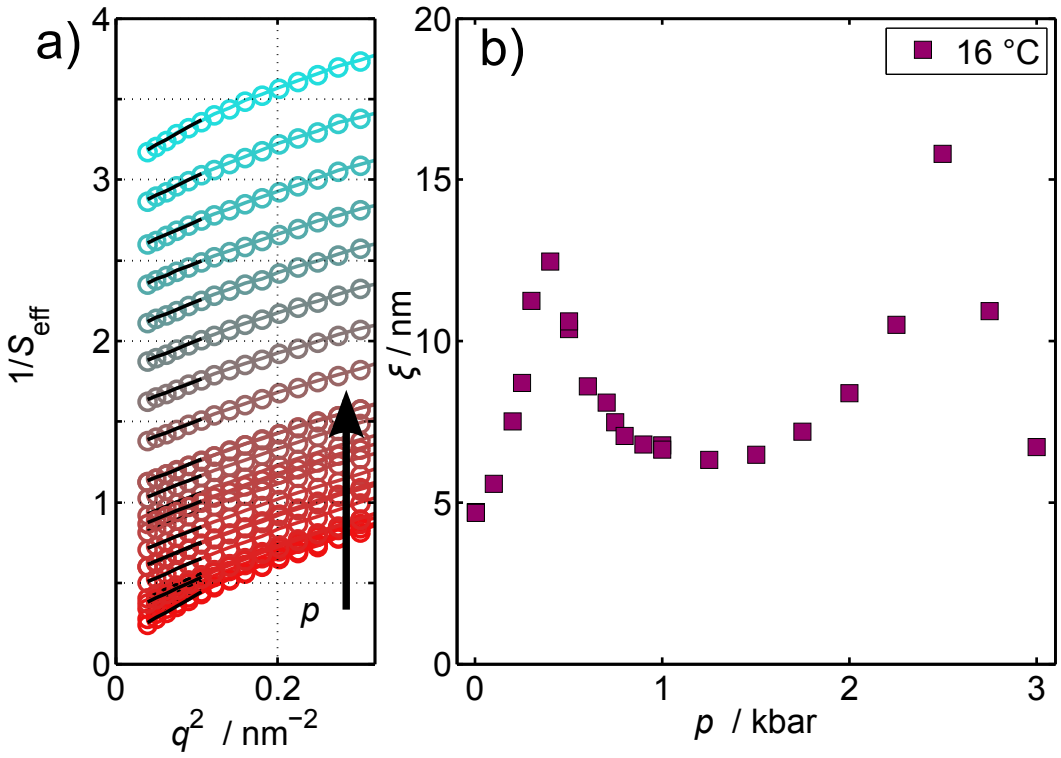

Figure 6.5: *a) Ornstein-Zernike plot of the scattering data for a 20 wt.% lysozyme solution at 16 °C together with refinement to the data. For reasons of clarity, the data are shifted proportional to the pressure applied. b) Pressure dependence of the correlation length, ξ, for the 20.0 wt.% lysozyme solution at 16 °C. Figures published in [Möller et al., 2014a].*

Ornstein-Zernike analysis of the scattering data is performed. At near critical conditions (see sec. 3.3.5), the scattering data should approximately vary as

$$S(q) = \frac{S(0)}{1 + \xi^2 q^2}, \tag{6.1}$$

with ξ being the correlation length of density or concentration fluctuations. The refinement to the scattering data is depicted in fig. 6.5 a), the pressure dependence of ξ in b). As an example for the analysis, the same sample as in fig. 6.3 (20 wt.% lysozyme, $T = 16$ °C) is presented. A drastic increase of the correlation length is clearly visible when the system passes the LLPS boundary at 400 and 2500 bar, respectively. This behavior was found for all samples that are in the LLPS phase at atmospheric pressure.

Therefore it can be stated that the increase in pressure from atmospheric conditions to 1.5 kbar has a suppressing effect on the liquid-liquid phase separation in dense protein solution. For all protein concentrations and temperatures studied, a pressure rise between 250 bar up to 1250 bar was found to tune the protein solution out of the phase separated state. Furthermore, a reentrance behavior is observed for pressures above 2 kbar. In order to connect the phase behavior with the underlying intermolecular interaction potential, further data evaluations are presented in the following section.

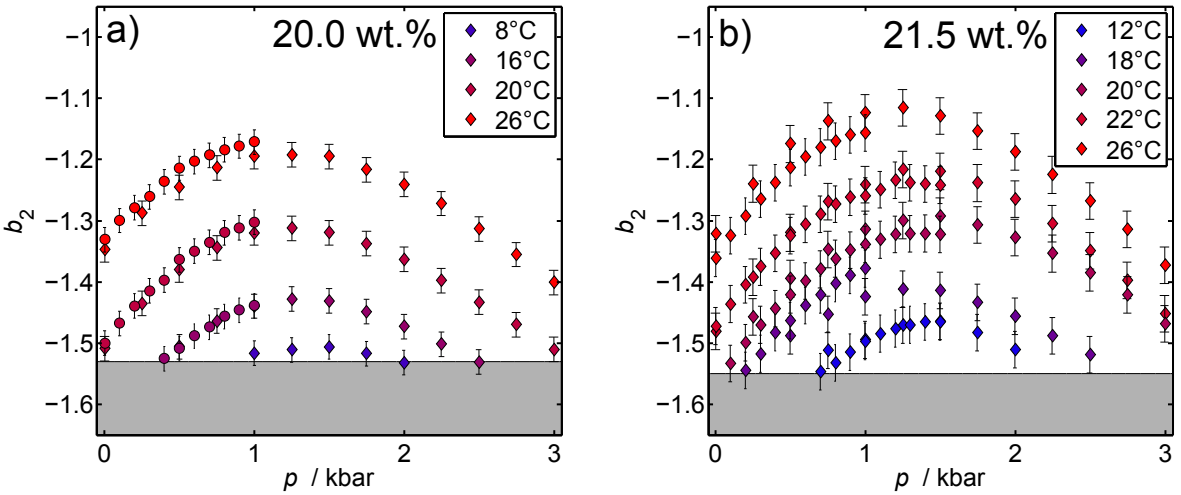

Figure 6.6: *Pressure dependence of the reduced second virial coefficient b_2 obtained from the refinement to the SAXS data measured at a)* 8, 16, 20, *and* 26 °*C (bottom to top) for a protein concentration of* 20.0 *wt.% and b)* 12, 18, 20, 22, *and* 26 °*C for a protein concentration of* 21.5 *wt.%. Figures published in [Möller et al., 2014a].*

6.2 Protein interactions near to the phase boundaries

A detailed analysis of the intermolecular interactions is performed by refining the before described sticky sphere model to the measured effective structure factors. For solution conditions where the protein solutions are in the homogenous one-phase region, numerical values for the second virial coefficient b_2 are extracted from the refinements. The refined SAXS curves are shown in fig. 6.3. With this, the reduced second virial coefficient b_2 can be determined for various highly concentrated lysozyme solutions as a function of temperature and pressure. As an example, fig. 6.6 a) displays b_2 for a 20 wt.% lysozyme solution for the same temperatures and pressures as presented in sec. 6.1. Fig. 6.6 b) shows the corresponding values with a lysozyme concentration of 21.5 wt.% at selected temperatures.

The obtained $b_2(p)$ values nicely reflect the non-linear pressure dependence of $S_{\text{eff}}(q)$, exhibiting a maximum between 1 and 1.5 kbar. Interestingly, when the protein interactions start to become more attractive again at higher pressures, the system is able to reenter the LLPS regime, which was already indicated by a second maximum in $S_{\text{eff}}(q = 0.2\,\text{nm}^{-2})$ at 2.5 kbar for $T = 16\,°\text{C}$ (fig. 6.4). The gathered b_2 values confirm this observation. The values are in good agreement with theoretical considerations, predicting the LLPS to occur at approximately $b_2 = -1.5$ [Vliegenthart and Lekkerkerker, 2000, Noro and Frenkel, 2000]. At both phase transitions (out of the LLPS at lower pressures and into the LLPS at higher pressures), b_2 is only slightly smaller. In fig. 6.6, the phase boundary is marked (gray area: LLPS) at $b_2 = -1.53$ for 20 wt.% lysozyme. Protein samples of 21.5 and 18.5 wt.% show the same behavior, with similar values for b_2 and slightly different values for the $p - T$ phase boundary for the LLPS (for 21.5 wt.% lysozyme, the phase boundary is found at $b_2 = -1.55$, for 18.5 wt.% at $b_2 = -1.53$). It can be stated that the obtained b_2 values from this study agree well with reported values of protein-protein interaction potentials near the LLPS phase boundary of $b_2 = -1.5$.

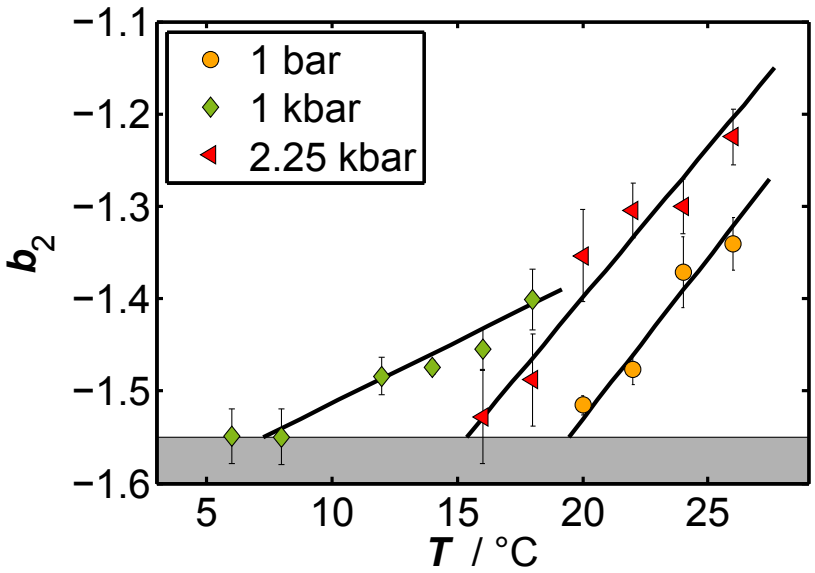

Figure 6.7: *Temperature dependence of the reduced second virial coefficent b_2 at pressures of 1 bar, 1 kbar, and 2.25 kbar. The protein concentration is 21.5 wt.%. Black lines indicate a linear fit to assess the LLPS boundary. Picture taken from [Möller et al., 2014a].*

In addition, the temperature dependence of b_2 at selected pressures can be determined from the measured data set. In fig. 6.7, b_2 is plotted as a function of temperature at pressures of 1 bar, 1 kbar, and 2.25 kbar, respectively. The data exhibit a linear temperature dependence near the phase boundary for all concentrations and pressures studied. Notably, the temperature dependence is much stronger for the samples at 1 bar and 2.25 kbar. The monotonic dependence of b_2 on temperatures matches the dependence found in mostly repulsive interaction potentials (see chapter 5). The linear trend was used to determine the phase separation temperature at the selected pressures by interpolating the measured values to $b_2(p, T) = -1.55$ or -1.53, respectively. The linear refinements to the data are also depicted in fig. 6.7.

6.3 The p-T phase diagram

From the combined $b_2(p, T)$ data, a p-T phase diagram can be constructed for the LLPS region of lysozyme, which is displayed in fig. 6.8 for protein concentrations of 18.5, 20.0, and 21.5 wt.%. The data points mark the phase boundary and are obtained from the pressure (diamonds) and temperature (circles) dependent b_2 data interpolated to the phase boundary.
The data points in the phase diagram are fitted by a Gaussian curve, centered at 1.45 kbar for all protein concentrations. Solution conditions, at which the samples undergo LLPS are marked in gray. Notably, the phase boundary of the LLPS curve obtained at 1 bar is in good agreement with data from literature [Cardinaux et al., 2007].
The LLPS phase formed at atmospheric conditions can be suppressed with relatively modest hydrostatic pressure. A pressure below 1 kbar was found for most solution conditions to tune the

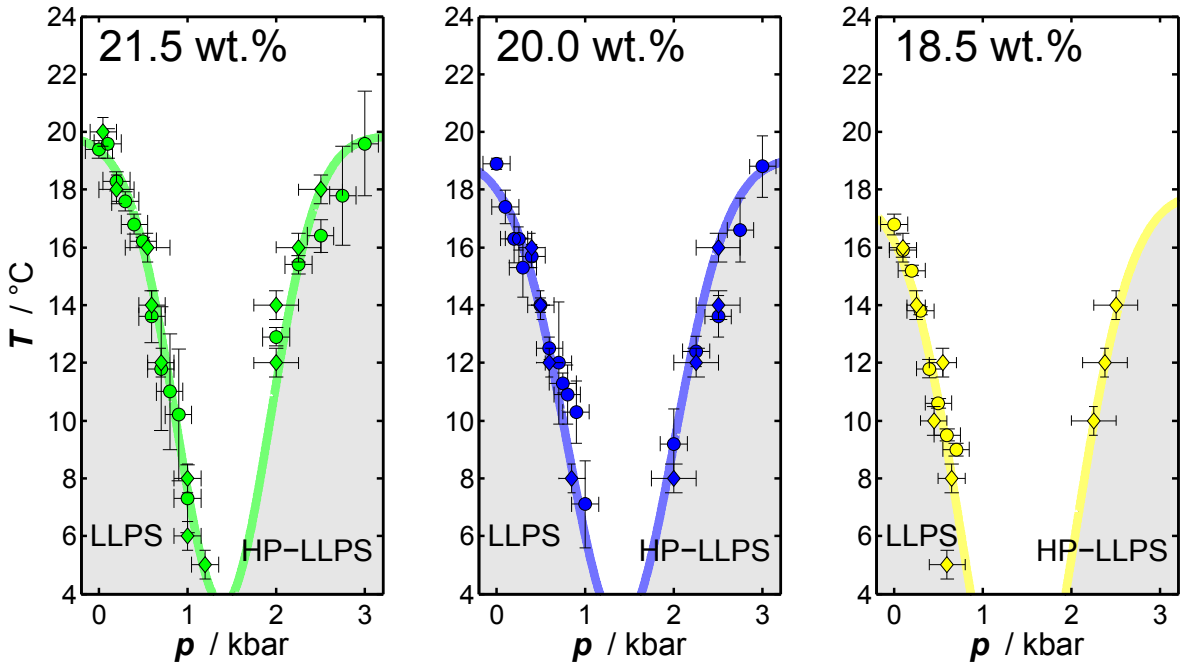

Figure 6.8: *p-T phase diagram of the LLPS of lysozyme for concentrations of* 21.5, 20.0, *and* 18.5 *wt.%. Low and high pressure (HP) areas of the LLPS are marked in gray. The phase boundaries are refined using a Gaussian function with a center at* 1.45 *kabr. Picture taken from [Möller et al., 2014a].*

protein solution out of the phase separated state. A higher protein concentration results in a shift of the phase boundary to higher temperatures[1]. A correlation between the phase separation temperature and pressure is found; lower temperatures move the phase boundary to higher pressures and vice versa. For higher pressures, a reentrant phase separation behavior is noted. Here, the combined influence of pressure and temperature has a reversed effect: An increase in temperature shifts the phase separation boundary to higher pressures. Higher protein concentrations have the same LLPS-promoting effect as at lower pressures.

The observed reentrant liquid-liquid phase separation behavior is consistent with the increasing attractivity of the interaction potential $V(r)$ at kbar pressure, which was described in the previous chapter. Caused by the non-linear pressure dependence of b_2, a reentrant LLPS is found at high pressures (HP-LLPS) for all protein concentrations studied. At lower pressures, the rising b_2 values with increasing pressure results in a suppression of the LLPS.

The occurrence of a reentrant phase separation as a function of an external parameter is rarely observed in protein solutions. A so-called reentrant condensation was observed as a function of concentration for trivalent ions (e.g. Y^{3+}) [Zhang et al., 2008, Zhang et al., 2012b]. In this case, the addition of the ions results in a charge inversion of the protein surface due to a strong binding of the multivalent counterions with the acidic surface residues. With this, the proteins can be tuned inside the LLPS phase with increasing salt concentration and out of the phase again at higher salt concentration. Even though this effect seems to be similar, the underlying working

[1] For protein concentrations below the critical concentration (≈ 25 wt.% [Cardinaux et al., 2007]), which is the case for the studied samples.

mechanism is markedly different. Due to the high ionic strength of 500 mM NaCl in the solutions studied in this thesis, the surface charge of the proteins is largely screened and no surface charge effect on the intermolecular interaction potential is expected. Furthermore, a pressure-stable buffer (Bis-Tris) is used.

A similar observation to the observed suppression of the LLPS with increasing pressure up to 2 kbar was found by [Gebhardt et al., 2012], reporting a pressure induced dissociation of protein oligomers in this pressure range. An increased hydration of the subunit interface is used to explain this behavior. However, no similar reversed behavior at high pressures has been reported for protein solutions so far.

In this chapter, the first ever investigation on the phenomenon of protein liquid-liquid phase separation (LLPS) influenced by increasing hydrostatic pressure was presented. An increase of pressure from atmospheric conditions is found to suppress the phase separation of the protein solution, similar to an increase in temperature. However, at pressures in the kbar range, a reentrant liquid-liquid phase separation happens, which is in striking contrast to the temperature dependence of the system.

7 Summary and outlook

In this thesis, the combined influence of temperature and pressure, alongside with salt concentration and type, on the intermolecular interaction potential of proteins in aqueous solution was investigated by small angle X-ray scattering experiments. A reentrant liquid-liquid phase separation behavior has been discovered in dense protein solutions, which is governed by the pressure dependence of the underlying intermolecular interaction potential. This study presents the first investigation on the phenomenon of liquid-liquid phase separation at elevated pressures so far. An unusual, V-shaped temperature-pressure phase diagram was established, which could be ascribed to the non-linear pressure dependence of the intermolecular interaction potential reported before. This non-monotonic behavior of the protein-protein interactions was assigned to distinct changes in the local water structure upon compression. A further observation was made in this thesis that supports this interpretation: A specific anion effect is found in the pressure dependence of the intermolecular interactions. Kosmotropic anions, namely phosphate and sulfate, to which water structuring properties are assigned, strongly influence the pressure dependence of the interaction potential, whereas sodium ions do not. This result may not only serve as a next step to explain this unusual pressure dependence, but also to shed light on the long discussed explanations of the Hofmeister effect on molecular level.

It was shown in this thesis that the intermolecular interaction potential and thereby the phase behavior of dense protein solutions can accurately be tuned by pressure modulation. With increasing attractivity of the intermolecular interaction potential due to a higher ionic strength, the influence of various external parameters like temperature, pressure, and salt type becomes considerably stronger. In this context, pressure can be a tool to tune nucleation rates and hence protein crystallization, or to prevent protein aggregation, which might be of practical importance for long-term storage of concentrated protein solutions. To this purpose, exact knowledge of the effect of different thermodynamical parameters on the intermolecular interaction potential of proteins is needed. The results underline the considerable advantage of the combined use of temperature and pressure to tune protein systems. This study may have relevance for different fields, like protein crystallization, protein purification, deep sea biology, or food processing.

The here presented results establish a systematic view on the intermolecular interactions and resulting phase behavior of proteins under high pressure conditions. However, further question may be raised. A task for future investigation could be to extend the investigation of this unusual phase behavior on a wider concentration range. The nucleation and growth behavior in protein crystallization is not only dependent on the influence of external parameters but does also strongly depend on the concentration of the protein. Further measurements may help to

extent the pressure-temperature-protein concentration phases diagram of the liquid-liquid phase separation. Moreover, the influence of particular ions on the pressure dependence of the protein-protein interactions has been demonstrated in this thesis. However, the influence of kosmotropic and chaotropic ions or crowding polymers on the p-T-ρ phase diagram remains unknown.

The described specific anion effect was found to strongly influence the pressure dependence of $V(r)$. The origin of the marked non-linear pressure dependence as well as the ability of different ions and osmolytes to strongly alter it are still not completely understood yet. Relatively little is known on the combined solvation behavior of macromolecules and ions and the consequent intermolecular interactions in the investigated pressure range. Further experimental and modeling approaches are needed to understand the processes involved on the molecular level. Computational studies such as molecular dynamics simulations may help to reveal the complex interplay between macromolecules, water molecules, and ions. The reported pressure dependence of the intermolecular interactions and the LLPS phase behavior can serve as a test for any theoretical modeling of protein solutions.

Further experimental work may also aim to directly probe the solvation behavior at elevated pressure. For example, X-ray absorption spectroscopy measurements on solvated ions under high pressure conditions may help to understand the influence of increased pressure on the solvation properties of ions. Furthermore, the local structure of water, which is the subject of ongoing research and scientific discussion, can directly be investigated by X-ray and neutron scattering techniques under high pressure conditions. Combining high pressure effects and the different properties of various ions may help to gain new insights into the molecular structure and dynamics of water. Very little work has been done with a focus on bio-physiological relevant solution conditions so far. Further studies using high hydrostatic pressure may provide fundamental insights into the molecular solvation properties of proteins and protein solutions.

The results described here demonstrate that pressure presents a precise tool to tune phase behavior and intermolecular interactions in dense protein solutions. Furthermore, this study shows that pressure serves as an excellent perturbation agent to gain insights into the fundamental molecular processes that govern protein solutions.

Publications

Publications related to this thesis:

- Möller, J., Schroer, M. A., Erlkamp, M., Grobelny, S., Paulus, M., Tiemeyer, S., Wirkert, F. J., Tolan, M., and Winter, R. (2012). The Effect of Ionic Strength, Temperature, and Pressure on the Interaction Potential of Dense Protein Solutions: From Nonlinear Pressure Response to Protein Crystallization. *Biophysical Journal*, 102(11): 2641-2648.
- Möller, J., Grobelny, S., Schulze, J., Bieder, S., Steffen, A., Erlkamp, M., Paulus, M., Tolan, M., and Winter, R. (2014). Reentrant Liquid-Liquid Phase Separation in Protein Solutions at Elevated Hydrostatic Pressures. *Physical Review Letters*, 112(2): 28101.
- Möller, J., Grobelny, S., Schulze, J., Steffen, A., Bieder, S., Paulus, M., Tolan, M., and Winter, R. (2014). Specifc anion effects on the pressure dependence of the protein-protein interaction potential. *Physical Chemistry Chemical Physics*, 16: 7423 – 7429.

Talks:

- Möller, J. Exploring the intermolecular interactions and phase behavior of dense protein solution: High pressure SAXS studies, *SAS*2012*: International Small-Angle Scattering Conference*, November 2012, Sydney, Australia.

Further publications:

- Möller, J., Cebi, M., Schroer, M. A., Paulus, M., Degen, P., Sahle, C. J., Wieland, D. C. F., Leick, S., Nyrow, A., Rehage, H., and Tolan, M. (2011). Dissolution of iron oxide nanoparticles inside polymer nanocapsules. *Physical Chemistry Chemical Physics*, 13: 20354 – 20360.
- Schroer, M. A., Markgraf, J., Wieland, D. C. F., Sahle, C. J., Möller, J., Paulus, M., Tolan, M., and Winter, R. (2011). Nonlinear Pressure Dependence of the Interaction Potential of Dense Protein Solutions. *Physical Review Letters*, 106(17): 178102.
- Brenner, T., Paulus, M., Schroer, M. A., Tiemeyer, S., Sternemann, C., Möller, J., Tolan, M., Degen, P., and Rehage, H. (2012). Adsorption of nanoparticles at the solid-liquid interface. *Journal of Colloid and Interface Science*, 374: 287 – 290.
- Tillmann, W., Ferreira, M., Steffen, A., Rüster, K., Möller, J., Bieder, S., Paulus, M., Tolan, M. (2013). Carbon reactivity of binder metals in diamond-metal composites - characterization by scanning electron microscopy and X-ray diffraction. *Diamond & Related Materials*, 38: 118 – 123.

- Wieland, D. C. F., Degen, P., Paulus, M., Schroer, M. A., Bieder, S., Sahle, C. J., Möller, J., Leick, S., Chen, Z., Struth, B., Rehage, H., and Tolan, M. (2013). Formation of iron containing aggregates at the liquid-air interface. *Colloids and Surfaces B: Biointerfaces*, 109: 74 – 81.

- Wirkert, F. J., Paulus, M., Nase, J., Möller, J., Kujawski, S., Sternemann, C., and Tolan, M. (2014). X-ray reflectivity measurements of liquid/solid interfaces under high hydrostatic pressure conditions. *Journal of Synchrotron Radiation*, 21: 76 – 81.

Bibliography

[Als-Nielsen and McMorrow, 2001] Als-Nielsen, J. and McMorrow, D. (2001). *Elements of Modern X-Ray Physics*. WILEY-VCH Verlag, New York, 1st edition.

[Ball, 2008] Ball, P. (2008). Water - an enduring mystery. *Nature*, 452(7185):291–292.

[Batchelor et al., 2004] Batchelor, J. D., Olteanu, A., Tripathy, A., and Pielak, G. J. (2004). Impact of Protein Denaturants and Stabilizers on Water Structure. *Journal of the American Chemical Society*, 126(7):1958–1961.

[Beamline BW4, 2012] Beamline BW4 (2012). http://hasylab.desy.de/facilities/doris_iii/beamlines/bw4/experimental_station/index_eng.html.

[Beamline I22, 2014] Beamline I22 (2014). http://www.diamond.ac.uk/Beamlines/Soft-Condensed-Matter/small-angle/I22.html.

[Beamline ID02, 2014] Beamline ID02 (2014). http://www.esrf.eu/UsersAndScience/Experiments/SoftMatter/ID02.

[Bénas et al., 2002] Bénas, P., Legrand, L., and Riès-Kautt, M. (2002). Strong and specific effects of cations on lysozyme chloride solubility. *Acta Crystallographica Section D*, 58(10 Part 1):1582–1587.

[Bennion and Daggett, 2004] Bennion, B. J. and Daggett, V. (2004). Counteraction of urea-induced protein denaturation by trimethylamine N-oxide: A chemical chaperone at atomic resolution. *Proceedings of the National Academy of Sciences of the United States of America*, 101(17):6433–6438.

[Bianchi et al., 2011] Bianchi, E., Blaak, R., and Likos, C. N. (2011). Patchy colloids: state of the art and perspectives. *Physical Chemistry Chemical Physics*, 13(14):6397–6410.

[Bonneté et al., 1999] Bonneté, F., Finet, S., and Tardieu, A. (1999). Second virial coefficient: variations with lysozyme crystallization conditions. *Journal of Crystal Growth*, 196(2-4):403–414.

[Boonyaratanakornkit et al., 2002] Boonyaratanakornkit, B. B., Park, C. B., and Clark, D. S. (2002). Pressure effects on intra- and intermolecular interactions within proteins. *Biochimica et Biophysica Acta (BBA) - Protein Structure and Molecular Enzymology*, 1595(1-2):235–249.

[Boström et al., 2006] Boström, M., Deniz, V., Franks, G. V., and Ninham, B. W. (2006). Extended DLVO theory: Electrostatic and non-electrostatic forces in oxide suspensions. *Advances in Colloid and Interface Science*, 123-126:5–15.

[Boström et al., 2001] Boström, M., Williams, D. R. M., and Ninham, B. W. (2001). Specific Ion Effects: Why DLVO Theory Fails for Biology and Colloid Systems. *Physical Review Letters*, 87(16):168103.

[Brandts and Hunt, 1967] Brandts, J. F. and Hunt, L. (1967). Thermodynamics of protein denaturation. III. Denaturation of ribonuclease in water and in aqueous urea and aqueous ethanol mixtures. *Journal of the American Chemical Society*, 89(19):4826–4838.

[Broide et al., 1996] Broide, M. L., Tominc, T. M., and Saxowsky, M. D. (1996). Using phase transitions to investigate the effect of salts on protein interactions. *Physical Review E*, 53(6):6325–6335.

[Brooks et al., 2010] Brooks, N. J., Gauthe, B. L. L. E., Terrill, N. J., Rogers, S. E., Templer, R. H., Ces, O., and Seddon, J. M. (2010). Automated high pressure cell for pressure jump x-ray diffraction. *Review of Scientific Instruments*, 81(6):64103.

[Bryngelson et al., 1995] Bryngelson, J. D., Onuchic, J. N., Socci, N. D., and Wolynes, P. G. (1995). Funnels, pathways, and the energy landscape of protein folding: A synthesis. *Proteins: Structure, Function, and Bioinformatics*, 21(3):167–195.

[Canfield and Liu, 1965] Canfield, R. E. and Liu, A. K. (1965). The disulfide bonds of egg white lysozyme (muramidase). *Journal of Biological Chemistry*, 240(5):1997–2002.

[Cardinaux et al., 2007] Cardinaux, F., Gibaud, T., Stradner, A., and Schurtenberger, P. (2007). Interplay between Spinodal Decomposition and Glass Formation in Proteins Exhibiting Short-Range Attractions. *Physical Review Letters*, 99(11):118301.

[Carlsson et al., 2001] Carlsson, F., Malmsten, M., and Linse, P. (2001). Monte Carlo Simulations of Lysozyme Self-Association in Aqueous Solution. *The Journal of Physical Chemistry B*, 105(48):12189–12195.

[Chayen and Saridakis, 2008] Chayen, N. E. and Saridakis, E. (2008). Protein crystallization: from purified protein to diffraction-quality crystal. *Nature Methods*, 5(2):147–153.

[Chen et al., 2004] Chen, Q., Vekilov, P. G., Nagel, R. L., and Hirsch, R. E. (2004). Liquid-Liquid Phase Separation in Hemoglobins: Distinct Aggregation Mechanisms of the β6 Mutants. *Biophysical Journal*, 86(3):1702–1712.

[Chinchalikar et al., 2013] Chinchalikar, A. J., Aswal, V. K., Kohlbrecher, J., and Wagh, A. G. (2013). Small-angle neutron scattering study of structure and interaction during salt-induced liquid-liquid phase transition in protein solutions. *Phys. Rev. E*, 87(6):62708.

[Collins, 2004] Collins, K. D. (2004). Ions from the Hofmeister series and osmolytes: effects on proteins in solution and in the crystallization process. *Methods*, 34(3):300–311.

[Crisman and Randolph, 2010] Crisman, R. L. and Randolph, T. W. (2010). Crystallization of recombinant human growth hormone at elevated pressures: Pressure effects on PEG-induced volume exclusion interactions. *Biotechnology and Bioengineering*, 107(4):663–672.

[Curtis and Lue, 2006] Curtis, R. and Lue, L. (2006). A molecular approach to bioseparations: Protein-protein and protein-salt interactions. *Chemical Engineering Science*, 61(3):907–923.

[Dahirel and Jardat, 2010] Dahirel, V. and Jardat, M. (2010). Effective interactions between charged nanoparticles in water: What is left from the DLVO theory? *Current Opinion in Colloid & Interface Science*, 15(1-2):2–7.

[Daniel et al., 2006] Daniel, I., Oger, P., and Winter, R. (2006). Origins of life and biochemistry under high-pressure conditions. *Chemical Society Reviews*, 35(10):858–875.

[Davidson et al., 1997] Davidson, P., Bourgaux, C., Sergot, P., and Livage, J. (1997). A Small-Angle X-ray Scattering Study of the Lyotropic Nematic Phase of Vanadium Pentoxide Gels. *Journal of Applied Crystallography*, 30(5 Part 2):727–732.

[Debenedetti, 2003] Debenedetti, P. G. (2003). Supercooled and glassy water. *Journal of Physics: Condensed Matter*, 15(45):R1669.

[Debye, 1915] Debye, P. (1915). Zerstreuung von Röntgenstrahlen. *Annalen der Physik*, 351(6):809–823.

[Debye, 1947] Debye, P. (1947). Molecular-weight Determination by Light Scattering. *The Journal of Physical and Colloid Chemistry*, 51(1):18–32.

[Debye and Bueche, 1949] Debye, P. and Bueche, A. M. (1949). Scattering by an Inhomogeneous Solid. *Journal of Applied Physics*, 20(6):518–525.

[Derjaguin and Landau, 1941] Derjaguin, B. and Landau, L. (1941). Theory of the stability of strongly charged lyophobic sols and of the adhesion of strongly charged particles in solutions of electrolytes. *Acta Physico Chemica URSS1*, 14:633.

[Dhont et al., 2008] Dhont, J. K., Gompper, G., Nägele, G., Richter, R., and Winkler, R. G., editors (2008). *Soft Matter - From Synthetic to Biological Materials: Lecture Notes of the 39th Spring School 2008*. Forschungszentrum Jülich, Jülich.

[Dill, 1990] Dill, K. A. (1990). Dominant forces in protein folding. *Biochemistry*, 29(31):7133–7155.

[Dill and Chan, 1997] Dill, K. A. and Chan, H. S. (1997). From Levinthal to pathways to funnels. *Nature Stuctural Biology*, 4(1):10–19.

[Dumetz et al., 2008] Dumetz, A. C., Chockla, A. M., Kaler, E. W., and Lenhoff, A. M. (2008). Protein Phase Behavior in Aqueous Solutions: Crystallization, Liquid-Liquid Phase Separation, Gels, and Aggregates. *Biophysical Journal*, 94(2):570–583.

[Feigin and Svergun, 1987] Feigin, L. A. and Svergun, D. I. (1987). *Structure Analysis by Small-Angle X-Ray and Neutron Scattering*. Plenum Press, Princeton, New Jersey.

[Filipponi et al., 2003] Filipponi, A., de Panfilis, S., Oliva, C., Ricci, M. A., D'Angelo, P., and Bowron, D. T. (2003). Ion Hydration under Pressure. *Physical Review Letters*, 91(16):165505.

[Floriano and Nascimento, 2004] Floriano, W. B. and Nascimento, M. A. C. (2004). Dielectric Constant and Density of Water as a Function of Pressure at Constant Temperature. *Brazilian Journal of Physics*, 34(1):38–41.

[Foguel et al., 1999] Foguel, D., Robinson, C. R., de Sousa, P. C., Silva, J. L., and Robinson, A. S. (1999). Hydrostatic pressure rescues native protein from aggregates. *Biotechnology and Bioengineering*, 63(5):552–558.

[Frye et al., 1996] Frye, K. J., Perman, C. S., and Royer, C. A. (1996). Testing the Correlation between ΔA and ΔV of Protein Unfolding Using m Value Mutants of Staphylococcal Nuclease. *Biochemistry*, 35(31):10234–10239.

[Galamba, 2013] Galamba, N. (2013). On the Effects of Temperature, Pressure, and Dissolved Salts on the Hydrogen-Bond Network of Water. *The Journal of Physical Chemistry B*, 117(2):589–601.

[Galkin et al., 2002] Galkin, O., Chen, K., Nagel, R. L., Hirsch, R. E., and Vekilov, P. G. (2002). Liquid-liquid separation in solutions of normal and sickle cell hemoglobin. *Proceedings of the National Academy of Sciences*, 99(13):8479–8483.

[Gebhardt et al., 2012] Gebhardt, R., Toro-Sierra, J., and Kulozik, U. (2012). Pressure dissociation of β-lactoglobulin oligomers near their isoelectric point. *Soft Matter*, 8(46):11654–11660.

[George and Wilson, 1994] George, A. and Wilson, W. W. (1994). Predicting protein crystallization from a dilute solution property. *Acta Crystallographica Section D*, 50(4):361–365.

[Ghosh et al., 2001] Ghosh, T., García, A. E., and Garde, S. (2001). Molecular Dynamics Simulations of Pressure Effects on Hydrophobic Interactions. *Journal of the American Chemical Society*, 123(44):10997–11003.

[Giegé, 2013] Giegé, R. (2013). A historical perspective on protein crystallization from 1840 to the present day. *FEBS Journal*, 280(24):6456–6497.

[Glatter, 2002] Glatter, O. (2002). The Inverse Scattering Problem in Small-Angle Scattering. In Lindner, P. and Zemb, T., editors, *Neutrons, X-ray and Light: Scattering Methods Applied to Soft Condensed Matter*, chapter 4, pages 73–102. Elsevier, Amsterdam, first edition.

[Glatter and Kratky, 1982] Glatter, O. and Kratky, O. (1982). *Small Angle X-ray Scattering*. Academic Press.

[Gögelein et al., 2012] Gögelein, C., Wagner, D., Cardinaux, F., Nägele, G., and Egelhaaf, S. U. (2012). Effect of glycerol and dimethyl sulfoxide on the phase behavior of lysozyme: Theory and experiments. *The Journal of Chemical Physics*, 136(1):–.

[Gorovits and Horowitz, 1998] Gorovits, B. M. and Horowitz, P. M. (1998). High Hydrostatic Pressure Can Reverse Aggregation of Protein Folding Intermediates and Facilitate Acquisition of Native Structure. *Biochemistry*, 37(17):6132–6135.

[Grigsby et al., 2001] Grigsby, J. J., Blanch, H. W., and Prausnitz, J. M. (2001). Cloud-point temperatures for lysozyme in electrolyte solutions: effect of salt type, salt concentration and pH. *Biophysical Chemistry*, 91(3):231–243.

[Gross and Jaenicke, 1991] Gross, M. and Jaenicke, R. (1991). Growth inhibition of lysozyme crystals at high hydrostatic pressure. *FEBS Letters*, 284(1):87–90.

[Gross and Jaenicke, 1993] Gross, M. and Jaenicke, R. (1993). A kinetic model explaining the effects of hydrostatic pressure on nucleation and growth of lysozyme crystals. *Biophysical Chemistry*, 45(3):245–252.

[Grudzielanek et al., 2006] Grudzielanek, S., Smirnovas, V., and Winter, R. (2006). Solvation-assisted Pressure Tuning of Insulin Fibrillation: From Novel Aggregation Pathways to Biotechnological Applications. *Journal of Molecular Biology*, 356(2):497–509.

[Guinier, 1939] Guinier, A. (1939). La diffraction des rayons X aux tres petits angles: applications a l'etude de phenomenes ultramicroscopiques. *Annales de physique*, 12:161–237.

[Guinier and Fournet, 1955] Guinier, A. and Fournet, G. (1955). *Small-angle Scattering of X-rays*. John Wiley & Sons, Inc., New York.

[Haas and Drenth, 1999] Haas, C. and Drenth, J. (1999). Understanding protein crystallization on the basis of the phase diagram. *Journal of Crystal Growth*, 196(2-4):388–394.

[Hansen and McDonald, 1986] Hansen, J. P. and McDonald, I. R. (1986). *Theory of Simple Liquids*. Academic Press, London, second edi edition.

[Hawley, 1971] Hawley, S. A. (1971). Reversible pressure-temperature denaturation of chymotrypsinogen. *Biochemistry*, 10(13):2436–2442.

[Henke et al., 1991] Henke, B. L., Gullikson, E. M., and Davis, J. C. (1991). X-ray interactions: photoabsorption, scattering, transmission, and reflection at E=50-30000 eV, Z=1-92. *Atomic Data and Nuclear Data Tables*, pages 181–342.

[Heremans and Smeller, 1998] Heremans, K. and Smeller, L. (1998). Protein structure and dynamics at high pressure. *Biochimica et Biophysica Acta (BBA) - Protein Structure and Molecular Enzymology*, 1386(2):353–370.

[Hofmeister, 1888] Hofmeister, F. (1888). Zur Lehre von der Wirkung der Salze. *Archiv für experimentelle Pathologie und Pharmakologie*, 25(1):1–30.

[Huang, 1987] Huang, K. (1987). *Statistical Mechanics*. John Wiley & Sons, Inc., New York, 2nd edition.

[Hummer et al., 1998] Hummer, G., Garde, S., García, A. E., Paulaitis, M. E., and Pratt, L. R. (1998). The pressure dependence of hydrophobic interactions is consistent with the observed pressure denaturation of proteins. *Proceedings of the National Academy of Sciences*, 95(4):1552–1555.

[Hura et al., 2009] Hura, G. L., Menon, A. L., Hammel, M., Rambo, R. P., Poole II, F. L., Tsutakawa, S. E., Jenney Jr, F. E., Classen, S., Frankel, K. A., Hopkins, R. C., Yang, S.-j., Scott, J. W., Dillard, B. D., Adams, M. W. W., and Tainer, J. A. (2009). Robust, high-throughput solution structural analyses by small angle X-ray scattering (SAXS). *Nature Methods*, 6(8):606–612.

[Jakubowski, 2014] Jakubowski, H. (2014). http://employees.csbsju.edu/hjakubowski/classes/ch331/protstructure/hofmeister.gif.

[James, 1967] James, R. W. (1967). *Optical Principles of the Diffraction of X-Rays*. G. Bell and Sons Limited, London.

[Javid et al., 2007a] Javid, N., Vogtt, K., Krywka, C., Tolan, M., and Winter, R. (2007a). Capturing the Interaction Potential of Amyloidogenic Proteins. *Physical Review Letters*, 99(2):28101.

[Javid et al., 2007b] Javid, N., Vogtt, K., Krywka, C., Tolan, M., and Winter, R. (2007b). Protein-Protein Interactions in Complex Cosolvent Solutions. *ChemPhysChem*, 8(5):679–689.

[Jenkins and Marcus, 1995] Jenkins, H. D. B. and Marcus, Y. (1995). Viscosity B-Coefficients of Ions in Solution. *Chemical Reviews*, 95(8):2695–2724.

[Kadri et al., 2003] Kadri, A., Damak, M., Jenner, G., Lorber, B., and Giegé, R. (2003). Investigating the nucleation of protein crystals with hydrostatic pressure. *Journal of Physics: Condensed Matter*, 15(49):8253.

[Kadri et al., 2005] Kadri, A., Lorber, B., Charron, C., Robert, M.-C., Capelle, B., Damak, M., Jenner, G., and Giegé, R. (2005). Crystal quality and differential crystal-growth behaviour of three proteins crystallized in gel at high hydrostatic pressure. *Acta Crystallographica Section D*, 61(6):784–788.

[Klein, 2002] Klein, R. (2002). Interaction Colloidal Suspensions. In Lindner, P. and Zemb, T., editors, *Neutrons, X-ray and Light: Scattering Methods Applied to Soft Condensed Matter*, chapter 14, pages 351–389. Elsevier, Amsterdam, first edition.

[Koizumi et al., 2007] Koizumi, M., Hirai, H., Onai, T., Inoue, K., and Hirai, M. (2007). Collapse of the hydration shell of a protein prior to thermal unfolding. *Journal of Applied Crystallography*, 40(s1):s175—-s178.

[Kotlarchyk and Chen, 1983] Kotlarchyk, M. and Chen, S.-H. (1983). Analysis of small angle neutron scattering spectra from polydisperse interacting colloids. *The Journal of Chemical Physics*, 79(5).

[Krywka, 2008] Krywka, C. (2008). *Ein Aufbau für Röntgenkleinwinkelstreuung an Protein-Lösungen an der Synchrotronstrahlungsquelle DELTA*. PhD thesis, TU Dortmund.

[Krywka et al., 2006] Krywka, C., Paulus, M., Sternemann, C., Volmer, M., Remhof, A., Nowak, G., Nefedov, A., Pöter, B., Spiegel, M., and Tolan, M. (2006). The new diffractometer for surface X-ray diffraction at beamline BL9 of DELTA. *Journal of Synchrotron Radiation*, 13(1):8–13.

[Krywka et al., 2007] Krywka, C., Sternemann, C., Paulus, M., Javid, N., Winter, R., Al-Sawalmih, A., Yi, S., Raabe, D., and Tolan, M. (2007). The small-angle and wide-angle X-ray scattering set-up at beamline BL9 of DELTA. *Journal of Synchrotron Radiation*, 14(3):244–251.

[Krywka et al., 2008] Krywka, C., Sternemann, C., Paulus, M., Tolan, M., Royer, C. A., and Winter, R. (2008). Effect of Osmolytes on Pressure-Induced Unfolding of Proteins: A High-Pressure SAXS Study. *ChemPhysChem*, 9(18):2809–2815.

[Kuehner et al., 1999] Kuehner, D. E., Engmann, J., Fergg, F., Wernick, M., Blanch, H. W., and Prausnitz, J. M. (1999). Lysozyme Net Charge and Ion Binding in Concentrated Aqueous Electrolyte Solutions. *The Journal of Physical Chemistry B*, 103(8):1368–1374.

[Kunz et al., 2004] Kunz, W., Henle, J., and Ninham, B. W. (2004). 'Zur Lehre von der Wirkung der Salze'(about the science of the effect of salts): Franz Hofmeister's historical papers. *Current Opinion in Colloid & Interface Science*, 9(1-2):19–37.

[Lebowitz and Percus, 1966] Lebowitz, J. L. and Percus, J. K. (1966). Mean Spherical Model for Lattice Gases with Extended Hard Cores and Continuum Fluids. *Physical Review*, 144(1):251–258.

[Lindner, 2002] Lindner, P. (2002). Scattering Experiments: Experimental Aspects, Initial Data Reduction and Absolute Calibration. In Linder, P. and Zemb, T., editors, *Neutrons, X-ray and Light: Scattering Methods Applied to Soft Condensed Matter*, chapter 2, pages 23–48. Elsevier, Amsterdam, first edition.

[Lindner and Zemb, 2002] Lindner, P. and Zemb, T., editors (2002). *Neutrons, X-ray and Light: Scattering Methods Applied to Soft Condensed Matter*. Elsevier Science B.V., Amsterdam, first edition.

[Liu et al., 2005] Liu, Y., Chen, W.-R., and Chen, S.-H. (2005). Cluster formation in two-Yukawa fluids. *The Journal of Chemical Physics*, 122(4):044507.

[Löffler et al., 2007] Löffler, G., Petrides, P. E., and Heinrich, P. C. (2007). *Biochemie & Pathobiochemie*. Springer-Verlag.

[Lorber et al., 1996] Lorber, B., Jenner, G., and Giegé, R. (1996). Effect of high hydrostatic pressure on nucleation and growth of protein crystals. *Journal of Crystal Growth*, 158(1-2):103–117.

[Ludwig, 2001] Ludwig, R. (2001). Water: From Clusters to the Bulk. *Angewandte Chemie International Edition*, 40(10):1808–1827.

[Malfois et al., 1996] Malfois, M., Bonneté, F., Belloni, L., and Tardieu, A. (1996). A model of attractive interactions to account for fluid-fluid phase separation of protein solutions. *The Journal of Chemical Physics*, 105(8):3290–3300.

[Mantegazzi et al., 2012] Mantegazzi, D., Sanchez-Valle, C., Reusser, E., and Driesner, T. (2012). Thermodynamic properties of aqueous sodium sulfate solutions to 773 K and 3 GPa derived from acoustic velocity measurements in the diamond anvil cell. *The Journal of Chemical Physics*, 137(22):224501.

[Marcus, 2009] Marcus, Y. (2009). Effect of Ions on the Structure of Water: Structure Making and Breaking. *Chemical Reviews*, 109(3):1346–1370.

[Martel et al., 2012] Martel, A., Liu, P., Weiss, T. M., Niebuhr, M., and Tsuruta, H. (2012). An integrated high-throughput data acquisition system for biological solution X-ray scattering studies. *Journal of Synchrotron Radiation*, 19(3):431–434.

[Meersman et al., 2013] Meersman, F., Daniel, I., Bartlett, D. H., Winter, R., Hazael, R., and McMillan, P. F. (2013). High-Pressure Biochemistry and Biophysics. *Reviews in Mineralogy and Geochemistry*, 75(1):607–648.

[Meersman et al., 2006] Meersman, F., Dobson, C. M., and Heremans, K. (2006). Protein unfolding, amyloid fibril formation and configurational energy landscapes under high pressure conditions. *Chemical Society Reviews*, 35(10):908–917.

[Menon et al., 1991] Menon, S. V. G., Kelkar, V. K., and Manohar, C. (1991). Application of Baxter's model to the theory of cloud points of nonionic surfactant solutions. *Physical Review A*, 43(2):1130–1133.

[Merzel and Smith, 2002] Merzel, F. and Smith, J. C. (2002). Is the first hydration shell of lysozyme of higher density than bulk water? *Proceedings of the National Academy of Sciences*, 99(8):5378–5383.

[Migliorati et al., 2013] Migliorati, V., Mancini, G., Tatoli, S., Zitolo, A., Filipponi, A., de Panfilis, S., di Cicco, A., and D'Angelo, P. (2013). Hydration Properties of the Zn2+ Ion in Water at High Pressure. *Inorganic Chemistry*, 52(2):1141–1150.

[Miller et al., 2013] Miller, J., Usselman, A., Anthony, R., Kortshagen, U. R., Wagner, A. J., Denton, A., and Hobbie, E. K. (2013). Phase separation and the 'coffee-ring' effect in polymer-nanocrystal mixtures. *Soft Matter*, 10(11):1665–1675.

[Mishra and Winter, 2008] Mishra, R. and Winter, R. (2008). Cold- and Pressure-Induced Dissociation of Protein Aggregates and Amyloid Fibrils. *Angewandte Chemie International Edition*, 47(35):6518–6521.

[Mitra et al., 2006] Mitra, L., Smolin, N., Ravindra, R., Royer, C. A., and Winter, R. (2006). Pressure perturbation calorimetric studies of the solvation properties and the thermal unfolding of proteins in solution-experiments and theoretical interpretation. *Physical Chemistry Chemical Physics*, 8(11):1249–1265.

[Mittelbach and Porod, 1962] Mittelbach, P. and Porod, G. (1962). Zur Röntgenkleinwinkelstreuung verdünnter kolloider Systeme VII. Die Berechnung der Streukurven von dreiachsigen Ellipsoiden. *Acta Phys. Austriaca*, 15:122–147.

[Möller, 2010] Möller, J. (2010). *Strukturelle Untersuchung von Eisenoxid-Nanopartikeln mittels Röntgenkleinwinkelstreuung*. diploma thesis (unpublished), TU Dortmund.

[Möller et al., 2014a] Möller, J., Grobelny, S., Schulze, J., Bieder, S., Steffen, A., Erlkamp, M., Paulus, M., Tolan, M., and Winter, R. (2014a). Reentrant Liquid-Liquid Phase Separation in Protein Solutions at Elevated Hydrostatic Pressures. *Physical Review Letters*, 112(2):28101.

[Möller et al., 2014b] Möller, J., Grobelny, S., Schulze, J., Steffen, A., Bieder, S., Paulus, M., Tolan, M., and Winter, R. (2014b). Specific anion effects on the pressure dependence of the protein-protein interaction potential. *Phys. Chem. Chem. Phys.*, 16:7423–7429.

[Möller et al., 2012] Möller, J., Schroer, M. A., Erlkamp, M., Grobelny, S., Paulus, M., Tiemeyer, S., Wirkert, F. J., Tolan, M., and Winter, R. (2012). The Effect of Ionic Strength, Temperature, and Pressure on the Interaction Potential of Dense Protein Solutions: From Nonlinear Pressure Response to Protein Crystallization. *Biophysical Journal*, 102(11):2641–2648.

[Mueller et al., 2007] Mueller, M., Jenni, S., and Ban, N. (2007). Strategies for crystallization and structure determination of very large macromolecular assemblies. *Current Opinion in Structural Biology*, 17(5):572–579.

[Muschol and Rosenberger, 1997] Muschol, M. and Rosenberger, F. (1997). Liquid-liquid phase separation in supersaturated lysozyme solutions and associated precipitate formation/crystallization. *The Journal of Chemical Physics*, 107(6):1953–1962.

[Nagatoshi et al., 2003] Nagatoshi, Y., Sazaki, G., Suzuki, Y., Miyashita, S., Matsui, T., Ujihara, T., Fujiwara, K., Usami, N., and Nakajima, K. (2003). Effects of high pressure on the growth kinetics of orthorhombic lysozyme crystals. *Journal of Crystal Growth*, 254(1-2):188–195.

[Nägele, 2008] Nägele, G. (2008). Theories of Fluid Microstructures. In Dhont, J. K., Gompper, G., Nägele, G., Richter, D., and Winkler, R. G., editors, *Soft Matter - From Synthetic to Biological Materials : Lecture Notes of the 39th Spring School 2008*, chapter B2. Forschungszentrum Jülich, Jülich.

[Narayanan and Liu, 2003] Narayanan, J. and Liu, X. Y. (2003). Protein Interactions in Undersaturated and Supersaturated Solutions: A Study Using Light and X-Ray Scattering. *Biophysical Journal*, 84(1):523–532.

[Narayanan et al., 2001] Narayanan, T., Diat, O., and Bösecke, P. (2001). SAXS and USAXS on the high brilliance beamline at the ESRF. *Nuclear Instruments and Methods in Physics Research Section A: Accelerators, Spectrometers, Detectors and Associated Equipment*, 467-468, P(0):1005–1009.

[Niebuhr and Koch, 2005] Niebuhr, M. and Koch, M. H. J. (2005). Effects of Urea and Trimethylamine-N-Oxide (TMAO) on the Interactions of Lysozyme in Solution. *Biophysical Journal*, 89(3):1978–1983.

[Nilsson and Pettersson, 2011] Nilsson, A. and Pettersson, L. G. M. (2011). Perspective on the structure of liquid water. *Chemical Physics*, 389(1-3):1–34.

[Ninham, 1999] Ninham, B. W. (1999). On progress in forces since the DLVO theory. *Advances in Colloid and Interface Science*, 83(1-3):1–17.

[Noro and Frenkel, 2000] Noro, M. G. and Frenkel, D. (2000). Extended corresponding-states behavior for particles with variable range attractions. *The Journal of Chemical Physics*, 113(8):2941–2944.

[Ohtaki and Radnai, 1993] Ohtaki, H. and Radnai, T. (1993). Structure and dynamics of hydrated ions. *Chemical Reviews*, 93(3):1157–1204.

[Okhulkov et al., 1994] Okhulkov, A. V., Demianets, Y. N., and Gorbaty, Y. E. (1994). X-ray scattering in liquid water at pressures of up to 7.7 kbar: Test of a fluctuation model. *The Journal of Chemical Physics*, 100(2):1578–1588.

[Omta et al., 2003] Omta, A. W., Kropman, M. F., Woutersen, S., and Bakker, H. J. (2003). Negligible Effect of Ions on the Hydrogen-Bond Structure in Liquid Water. *Science*, 301(5631):347–349.

[Oregon State University, 2008] Oregon State University (2008). http://cropandsoil.oregonstate.edu/classes/css430/lecture%209-07/figure-09-03.jpg.

[Ornstein and Zernike, 1914] Ornstein, L. S. and Zernike, F. (1914). Accidental deviations of density and opalescence at the critical point of a single substance. *Koninklijke Nederlandse Akademie van Wetenschappen Amsterdam Proc. Sec. Sci.*, 17:793–806.

[Ortore et al., 2009] Ortore, M. G., Spinozzi, F., Mariani, P., Paciaroni, A., Barbosa, L. R. S., Amenitsch, H., Steinhart, M., Ollivier, J., and Russo, D. (2009). Combining structure and dynamics: non-denaturing high-pressure effect on lysozyme in solution. *Journal of The Royal Society Interface*, 6(Suppl 5):S619–S634.

[Pande et al., 2001] Pande, A., Pande, J., Asherie, N., Lomakin, A., Ogun, O., King, J., and Benedek, G. B. (2001). Crystal cataracts: Human genetic cataract caused by protein crystallization. *Proceedings of the National Academy of Sciences*, 98(11):6116–6120.

[Panick et al., 1998] Panick, G., Malessa, R., Winter, R., Rapp, G., Frye, K. J., and Royer, C. A. (1998). Structural characterization of the pressure-denatured state and unfolding/refolding kinetics of staphylococcal nuclease by synchrotron small-angle X-ray scattering and Fourier-transform infrared spectroscopy. *Journal of Molecular Biology*, 275(2):389–402.

[Panick et al., 1999] Panick, G., Vidugiris, G. J. A., Malessa, R., Rapp, G., Winter, R., and Royer, C. A. (1999). Exploring the Temperature-Pressure Phase Diagram of Staphylococcal Nuclease. *Biochemistry*, 38(13):4157–4164.

[Panine et al., 2003] Panine, P., Gradzielski, M., and Narayanan, T. (2003). Combined rheometry and small-angle x-ray scattering. *Review of Scientific Instruments*, 74(4):2451–2455.

[Paschek and Ludwig, 2011] Paschek, D. and Ludwig, R. (2011). Specific Ion Effects on Water Structure and Dynamics beyond the First Hydration Shell. *Angewandte Chemie International Edition*, 50(2):352–353.

[Paulis et al., 2009] Paulis, M., Bonnefond, A., Mičušik, M., and Leiza, J. R. (2009). New agitated and thermostatized cell for in situ monitoring of fast reactions by synchrotron SAXS. *Journal of Synchrotron Radiation*, 16(6):869–871.

[Paulus et al., 2008] Paulus, M., Lietz, D., Sternemann, C., Shokuie, K., Evers, F., Tolan, M., Czeslik, C., and Winter, R. (2008). An access to buried interfaces: the X-ray reflectivity set-up of BL9 at DELTA. *Journal of Synchrotron Radiation*, 15(6):600–605.

[Pellicane et al., 2003] Pellicane, G., Costa, D., and Caccamo, C. (2003). Phase coexistence in a DLVO model of globular protein solutions. *Journal of Physics: Condensed Matter*, 15(3):375.

[Percus and Yevick, 1958] Percus, J. K. and Yevick, G. J. (1958). Analysis of Classical Statistical Mechanics by Means of Collective Coordinates. *Physical Review*, 110(1):1–13.

[Pernot et al., 2013] Pernot, P., Round, A., Barrett, R., de Maria Antolinos, A., Gobbo, A., Gordon, E., Huet, J., Kieffer, J., Lentini, M., Mattenet, M., Morawe, C., Mueller-Dieckmann, C., Ohlsson, S., Schmid, W., Surr, J., Theveneau, P., Zerrad, L., and McSweeney, S. (2013). Upgraded ESRF BM29 beamline for SAXS on macromolecules in solution. *Journal of Synchrotron Radiation*, 20(4):660–664.

[Perrett and Zhou, 2002] Perrett, S. and Zhou, J.-M. (2002). Expanding the pressure technique: insights into protein folding from combined use of pressure and chemical denaturants. *Biochimica et Biophysica Acta (BBA) - Protein Structure and Molecular Enzymology*, 1595(1-2):210–223.

[Poon et al., 2000] Poon, W. C. K., Egelhaaf, S. U., Beales, P. A., Salonen, A., and Sawyer, L. (2000). Protein crystallization: scaling of charge and salt concentration in lysozyme solutions. *Journal of Physics: Condensed Matter*, 12(35):L569.

[Porod, 1948] Porod, G. (1948). Die Abhängigkeit der Röntgen-Kleinwinkelstreuung von Form und Größe der kolloiden Teilchen in verdünnten Systemen. IV. *Acta Phys. Austriaca*, 2:255.

[Porod, 1951] Porod, G. (1951). Die Röntgenkleinwinkelstreuung von dichtgepackten kolloiden Systemen. *Kolloid-Zeitschrift*, 124(2):83–114.

[Porod, 1982] Porod, G. (1982). General Theory. In Glatter, O. and Kratky, O., editors, *Small Angle X-ray Scattering*, chapter 2, pages 17–51. Academic Press, London.

[Poulter, 1932] Poulter, T. C. (1932). Apparatus for Optical Studies at High Pressure. *Physical Review*, 40(5):860–871.

[Pribil et al., 2008] Pribil, A. B., Hofer, T. S., Randolf, B. R., and Rode, B. M. (2008). Structure and dynamics of phosphate ion in aqueous solution: An ab initio QMCF MD study. *Journal of Computational Chemistry*, 29(14):2330–2334.

[PSI, 2014] PSI (2014). TargetTrack, http://sbkb.org/tt/.

[Quang et al., 2014] Quang, L. J., Sandler, S. I., and Lenhoff, A. M. (2014). Anisotropic Contributions to Protein-Protein Interactions. *Journal of Chemical Theory and Computation*, 10(2):835–845.

[RCSB, 1971] RCSB (1971). Protein Data Bank, www.rcsb.org.

[Roche et al., 2013] Roche, J., Dellarole, M., Caro, J. A., Norberto, D. R., García, A. E., Garcia-Moreno, B., Roumestand, C., and Royer, C. A. (2013). Effect of Internal Cavities on Folding Rates and Routes Revealed by Real-Time Pressure-Jump NMR Spectroscopy. *Journal of the American Chemical Society*, 135(39):14610–14618.

[Rosch and Errington, 2007] Rosch, T. W. and Errington, J. R. (2007). Investigation of the Phase Behavior of an Embedded Charge Protein Model through Molecular Simulation. *The Journal of Physical Chemistry B*, 111(43):12591–12598.

[Rosenbaum et al., 1996] Rosenbaum, D., Zamora, P. C., and Zukoski, C. F. (1996). Phase Behavior of Small Attractive Colloidal Particles. *Physical Review Letters*, 76(1):150–153.

[Roth et al., 2006] Roth, S. V., Dohrmann, R., Dommach, M., Kuhlmann, M., Kroger, I., Gehrke, R., Walter, H., Schroer, C., Lengeler, B., and Muller-Buschbaum, P. (2006). Small-angle options of the upgraded ultrasmall-angle x-ray scattering beamline BW4 at HASYLAB. *Review of Scientific Instruments*, 77(8):85106.

[Royer, 2002] Royer, C. A. (2002). Revisiting volume changes in pressure-induced protein unfolding. *Biochimica et Biophysica Acta (BBA) - Protein Structure and Molecular Enzymology*, 1595(1-2):201–209.

[Russo et al., 2013] Russo, D., Ortore, M. G., Spinozzi, F., Mariani, P., Loupiac, C., Annighofer, B., and Paciaroni, A. (2013). The impact of high hydrostatic pressure on structure and dynamics of β-lactoglobulin. *Biochimica et Biophysica Acta (BBA) - General Subjects*, 1830(10):4974–4980.

[Saikumar et al., 1995] Saikumar, M. V., Glatz, C. E., and Larson, M. A. (1995). Crystallization of lysozyme at high pressures. *Journal of Crystal Growth*, 151(1-2):173–179.

[Sazaki et al., 1999] Sazaki, G., Nagatoshi, Y., Suzuki, Y., Durbin, S. D., Miyashita, S., Nakada, T., and Komatsu, H. (1999). Solubility of tetragonal and orthorhombic lysozyme crystals under high pressure. *Journal of Crystal Growth*, 196(2-4):204–209.

[Schall et al., 1994] Schall, C. A., Wiencek, J. M., Yarmush, M., and Arnold, E. (1994). Lysozyme crystal growth reduced at high pressure. *Journal of Crystal Growth*, 135(3-4):548–554.

[Schroer, 2011] Schroer, M. A. (2011). *Small angle X-ray scattering studies on proteins under extreme conditions*. PhD thesis, TU Dortmund.

[Schroer et al., 2011a] Schroer, M. A., Markgraf, J., Wieland, D. C. F., Sahle, C. J., Möller, J., Paulus, M., Tolan, M., and Winter, R. (2011a). Nonlinear Pressure Dependence of the Interaction Potential of Dense Protein Solutions. *Physical Review Letters*, 106(17):178102.

[Schroer et al., 2010] Schroer, M. A., Paulus, M., Jeworrek, C., Krywka, C., Schmacke, S., Zhai, Y., Wieland, D. C. F., Sahle, C. J., Chimenti, M. S., Royer, C. A., Garcia-Moreno, B., Tolan, M., and Winter, R. (2010). High-Pressure SAXS Study of Folded and Unfolded Ensembles of Proteins. *Biophysical Journal*, 99(10):3430–3437.

[Schroer et al., 2012] Schroer, M. A., Tolan, M., and Winter, R. (2012). Exploring the thermodynamic derivatives of the structure factor of dense protein solutions. *Physical Chemistry Chemical Physics*, 14(26):9486–9491.

[Schroer et al., 2011b] Schroer, M. A., Zhai, Y., Wieland, D. C. F., Sahle, C. J., Nase, J., Paulus, M., Tolan, M., and Winter, R. (2011b). Exploring the Piezophilic Behavior of Natural Cosolvent Mixtures. *Angewandte Chemie International Edition*, 123(48):11615–11618.

[Schurtenberger, 2002] Schurtenberger, P. (2002). Contrast and Contrast Variation in Neutron, X-Ray and Light Scattering. In Lindner, P. and Zemb, T., editors, *Neutrons, X-ray and Light: Scattering Methods Applied to Soft Condensed Matter*, chapter 7. Elsevier, Amsterdam, first edition.

[Sciortino et al., 1991] Sciortino, F., Geiger, A., and Stanley, H. E. (1991). Effect of defects on molecular mobility in liquid water. *Nature*, 354(6350):218–221.

[Sedgwick et al., 2007] Sedgwick, H., Cameron, J. E., Poon, W. C. K., and Egelhaaf, S. U. (2007). Protein phase behavior and crystallization: Effect of glycerol. *The Journal of Chemical Physics*, 127(12):125102.

[Shukla et al., 2008a] Shukla, A., Mylonas, E., di Cola, E., Finet, S., Timmins, P., Narayanan, T., and Svergun, D. I. (2008a). Absence of equilibrium cluster phase in concentrated lysozyme solutions. *Proceedings of the National Academy of Sciences*, 105(13):5075–5080.

[Shukla et al., 2008b] Shukla, A., Mylonas, E., di Cola, E., Finet, S., Timmins, P., Narayanan, T., and Svergun, D. I. (2008b). Reply to Stradner et al.: Equilibrium clusters are absent in concentrated lysozyme solutions. *Proceedings of the National Academy of Sciences*, 105(44):E76.

[Silva et al., 2001] Silva, J. L., Foguel, D., and Royer, C. A. (2001). Pressure provides new insights into protein folding, dynamics and structure. *Trends in Biochemical Sciences*, 26(10):612–618.

[Smeller, 2002] Smeller, L. (2002). Pressure-temperature phase diagrams of biomolecules. *Biochimica et Biophysica Acta (BBA) - Protein Structure and Molecular Enzymology*, 1595(1-2):11–29.

[Smith et al., 2007] Smith, J. D., Saykally, R. J., and Geissler, P. L. (2007). The Effects of Dissolved Halide Anions on Hydrogen Bonding in Liquid Water. *Journal of the American Chemical Society*, 129(45):13847–13856.

[Soper and Ricci, 2000] Soper, A. K. and Ricci, M. A. (2000). Structures of High-Density and Low-Density Water. *Physical Review Letters*, 84(13):2881–2884.

[Sophianopoulos et al., 1962] Sophianopoulos, A. J., Rhodes, C. K., Holcomb, D. N., and Van Holde, K. E. (1962). Physical Studies of Lysozyme: I. CHARACTERIZATION. *Journal of Biological Chemistry*, 237(4):1107–1112.

[Spalla, 2002] Spalla, O. (2002). General Theorems in Small-Angle Scattering. In Lindner, P. and Zemb, T., editors, *Neutrons, X-ray and Light: Scattering Methods Applied to Soft Condensed Matter*, pages 49–72. Elsevier, Amsterdam, first edition.

[St. John et al., 1999] St. John, R. J., Carpenter, J. F., and Randolph, T. W. (1999). High pressure fosters protein refolding from aggregates at high concentrations. *Proceedings of the National Academy of Sciences*, 96(23):13029–13033.

[Stradner et al., 2008] Stradner, A., Cardinaux, F., Egelhaaf, S. U., and Schurtenberger, P. (2008). Do equilibrium clusters exist in concentrated lysozyme solutions? *Proceedings of the National Academy of Sciences*, 105(44):E75.

[Stradner et al., 2004] Stradner, A., Sedgwick, H., Cardinaux, F., Poon, W. C. K., Egelhaaf, S. U., and Schurtenberger, P. (2004). Equilibrium cluster formation in concentrated protein solutions and colloids. *Nature*, 432(7016):492–495.

[Street et al., 2006] Street, T. O., Bolen, D. W., and Rose, G. D. (2006). A molecular mechanism for osmolyte-induced protein stability. *Proceedings of the National Academy of Sciences*, 103(38):13997–14002.

[Stuhrmann, 1982] Stuhrmann, H. B. (1982). Anomale Röntgenstreuung zur Erforschung makromolekularer Strukturen. *Die Makromolekulare Chemie*, 183(10):2501–2514.

[Suzuki et al., 2005] Suzuki, Y., Sazaki, G., Matsui, T., Nakajima, K., and Tamura, K. (2005). High-Pressure Acceleration of the Growth Kinetics of Glucose Isomerase Crystals. *The Journal of Physical Chemistry B*, 109(8):3222–3226.

[Suzuki et al., 2002a] Suzuki, Y., Sazaki, G., Miyashita, S., Sawada, T., Tamura, K., and Komatsu, H. (2002a). Protein crystallization under high pressure. *Biochimica et Biophysica Acta (BBA) - Protein Structure and Molecular Enzymology*, 1595(1-2):345–356.

[Suzuki et al., 2002b] Suzuki, Y., Sazaki, G., Visuri, K., Tamura, K., Nakajima, K., and Yanagiya, S.-i. (2002b). Significant Decrease in the Solubility of Glucose Isomerase Crystals under High Pressure. *Crystal Growth & Design*, 2(5):321–324.

[Svergun, 1991] Svergun, D. I. (1991). Mathematical methods in small-angle scattering data analysis. *Journal of Applied Crystallography*, 24(5):485–492.

[Svergun, 1992] Svergun, D. I. (1992). Determination of the regularization parameter in indirect-transform methods using perceptual criteria. *Journal of Applied Crystallography*, 25(4):495–503.

[Svergun, 1999] Svergun, D. I. (1999). Restoring Low Resolution Structure of Biological Macromolecules from Solution Scattering Using Simulated Annealing. *Biophysical Journal*, 76(6):2879–2886.

[Svergun and Koch, 2003] Svergun, D. I. and Koch, M. H. J. (2003). Small-angle scattering studies of biological macromolecules in solution. *Reports on Progress in Physics*, 66(10):1735.

[Svergun et al., 1998] Svergun, D. I., Richard, S., Koch, M. H. J., Sayers, Z., Kuprin, S., and Zaccai, G. (1998). Protein hydration in solution: Experimental observation by x-ray and neutron scattering. *Proceedings of the National Academy of Sciences*, 95(5):2267–2272.

[Svergun et al., 1988] Svergun, D. I., Semenyuk, A. V., and Feigin, L. A. (1988). Small-angle-scattering-data treatment by the regularization method. *Acta Crystallographica Section A*, 44(3):244–250.

[Takano et al., 1997] Takano, K. J., Harigae, H., Kawamura, Y., and Ataka, M. (1997). Effect of hydrostatic pressure on the crystallization of lysozyme based on in situ observations. *Journal of Crystal Growth*, 171(3-4):554–558.

[Taratuta et al., 1990] Taratuta, V. G., Holschbach, A., Thurston, G. M., Blankschtein, D., and Benedek, G. B. (1990). Liquid-liquid phase separation of aqueous lysozyme solutions: effects of pH and salt identity. *The Journal of Physical Chemistry*, 94(5):2140–2144.

[Tardieu et al., 2002] Tardieu, A., Bonneté, F., Finet, S., and Vivarès, D. (2002). Understanding salt or PEG induced attractive interactions to crystallize biological macromolecules. *Acta Crystallographica: Section D*, 58(10):1549–1553.

[Tardieu et al., 1999] Tardieu, A., Verge, A. L., Malfois, M., Bonneté, F., Finet, S., Riès-Kautt, M., and Belloni, L. (1999). Proteins in solution : from X-ray scattering intensities to interaction potentials. *Journal of Crystal Growth*, 196(2-4):193–203.

[Thomson et al., 1987] Thomson, J. A., Schurtenberger, P., Thurston, G. M., and Benedek, G. B. (1987). Binary liquid phase separation and critical phenomena in a protein/water solution. *Proceedings of the National Academy of Sciences*, 84(20):7079–7083.

[van Leeuwen et al., 1959] van Leeuwen, J. M. J., Groeneveld, J., and de Boer, J. (1959). New method for the calculation of the pair correlation function. I. *Physica*, 25(7-12):792–808.

[Vchirawongkwin et al., 2007] Vchirawongkwin, V., Rode, B. M., and Persson, I. (2007). Structure and Dynamics of Sulfate Ion in Aqueous SolutionAn ab initio QMCF MD Simulation and Large Angle X-ray Scattering Study. *The Journal of Physical Chemistry B*, 111(16):4150–4155.

[Verwey, 1947] Verwey, E. J. W. (1947). Theory of the Stability of Lyophobic Colloids. *The Journal of Physical and Colloid Chemistry*, 51(3):631–636.

[Vivarès and Bonneté, 2004] Vivarès, D. and Bonneté, F. (2004). Liquid-Liquid Phase Separations in Urate Oxidase/PEG Mixtures: Characterization and Implications for Protein Crystallization. *The Journal of Physical Chemistry B*, 108(20):6498–6507.

[Vliegenthart and Lekkerkerker, 2000] Vliegenthart, G. A. and Lekkerkerker, H. N. W. (2000). Predicting the gas-liquid critical point from the second virial coefficient. *The Journal of Chemical Physics*, 112(12):5364–5369.

[Voet et al., 2005] Voet, D., Voet, J. G., and Pratt, C. W. (2005). *Fundamentals of Biochemistry: Life at the Molecular Lever*. WILEY-VCH Verlag, 2nd edition.

[Vrij, 1979] Vrij, A. (1979). Mixtures of hard spheres in the Percus-Yevick approximation. Light scattering at finite angles. *The Journal of Chemical Physics*, 71(8):3267–3270.

[Waghmare et al., 2000] Waghmare, R. Y., Webb, J. N., Randolph, T. W., Larson, M. A., and Glatz, C. E. (2000). Pressure dependence of subtilisin crystallization kinetics. *Journal of Crystal Growth*, 208(1-4):678–686.

[Wang et al., 2010] Wang, Y., Lomakin, A., McManus, J. J., Ogun, O., and Benedek, G. B. (2010). Phase behavior of mixtures of human lens proteins Gamma D and Beta B1. *Proceedings of the National Academy of Sciences*, 107(30):13282–13287.

[Webb et al., 1999] Webb, J. N., Waghmare, R. Y., Carpenter, J. F., Glatz, C. E., and Randolph, T. W. (1999). Pressure effect on subtilisin crystallization and solubility. *Journal of Crystal Growth*, 205(4):563–574.

[Wikimedia, 2014] Wikimedia (2014). http://commons.wikimedia.org.

[Wills and Winzor, 2005] Wills, P. R. and Winzor, D. J. (2005). van der Waals phase transition in protein solutions. *Acta Crystallographica Section D*, 61(6):832–836.

[Winter et al., 2011] Winter, R., Noll, F., and Czeslik, C. (2011). *Methoden der Biophysikalischen Chemie (german)*. Vieweg + Teubner, Wiesbaden, 2nd edition.

[Wirkert et al., 2014] Wirkert, F. J., Paulus, M., Nase, J., Möller, J., Kujawski, S., Sternemann, C., and Tolan, M. (2014). X-ray reflectivity measurements of liquid/solid interfaces under high hydrostatic pressure conditions. *Journal of Synchrotron Radiation*, 21(1):76–81.

[Zhang et al., 2012a] Zhang, F., Roosen-Runge, F., Skoda, M. W. A., Jacobs, R. M. J., Wolf, M., Callow, P., Frielinghaus, H., Pipich, V., Prevost, S., and Schreiber, F. (2012a). Hydration and interactions in protein solutions containing concentrated electrolytes studied by small-angle scattering. *Physical Chemistry Chemical Physics*, 14(7):2483–2493.

[Zhang et al., 2012b] Zhang, F., Roth, R., Wolf, M., Roosen-Runge, F., Skoda, M. W. A., Jacobs, R. M. J., Stzucki, M., and Schreiber, F. (2012b). Charge-controlled metastable liquid-liquid phase separation in protein solutions as a universal pathway towards crystallization. *Soft Matter*, 8(5):1313–1316.

[Zhang et al., 2007] Zhang, F., Skoda, M. W. A., Jacobs, R. M. J., Martin, R. A., Martin, C. M., and Schreiber, F. (2007). Protein Interactions Studied by SAXS: Effect of Ionic Strength and Protein Concentration for BSA in Aqueous Solutions. *The Journal of Physical Chemistry B*, 111(1):251–259.

[Zhang et al., 2008] Zhang, F., Skoda, M. W. A., Jacobs, R. M. J., Zorn, S., Martin, R. A., Martin, C. M., Clark, G. F., Weggler, S., Hildebrandt, A., Kohlbacher, O., and Schreiber, F. (2008). Reentrant Condensation of Proteins in Solution Induced by Multivalent Counterions. *Physical Review Letters*, 101(14):148101.

[Zhang and Cremer, 2006] Zhang, Y. and Cremer, P. S. (2006). Interactions between macromolecules and ions: the Hofmeister series. *Current Opinion in Chemical Biology*, 10(6):658–663.

[Zhang and Cremer, 2009] Zhang, Y. and Cremer, P. S. (2009). The inverse and direct Hofmeister series for lysozyme. *Proceedings of the National Academy of Sciences*, 106(36):15249–15253.

[Zhang and Cremer, 2010] Zhang, Y. and Cremer, P. S. (2010). Chemistry of Hofmeister Anions and Osmolytes. *Annual Review of Physical Chemistry*, 61(1):63–83.

[Zou et al., 2002] Zou, Q., Bennion, B. J., Daggett, V., and Murphy, K. P. (2002). The Molecular Mechanism of Stabilization of Proteins by TMAO and Its Ability to Counteract the Effects of Urea. *Journal of the American Chemical Society*, 124(7):1192–1202.

Acknowledgements

I am thankful to Prof. Dr. M. Tolan and Prof. Dr. R. Winter for giving me the opportunity to work on this interesting and challenging research topic. Their advice and help was highly appreciated throughout the years.

I thank Dr. Martin Schroer for his detailed and dedicated introduction to small angle scattering. Dr. Michael Paulus and Dr. Martin Schroer were constant support and help during the time of this thesis.

I am deeply thankful to all the colleagues who contributed to the outcome of this thesis. Without their help, day and night(-shift), this thesis would not have been possible. Many thanks to Dr. Martin Schroer, Dr. Michael Paulus, Dr. Christian Sternemann, Sebastian Grobelny, Julian Schulze, Mirko Erlkamp, Steffen Bieder, Dr. Andre Steffen, Dr. Florian Wieland, Dr. Christoph Sahle, Dr. Sebastian Tiemeyer, David Engemann, and everybody else I might have forgotten.

The local contacts Dr. M. Sztucki (ID02, ESRF), Dr. M. Malfois, Dr. A. Smith (I22, Diamond Light Source), and Dr. J. Perlich (BW4, HASYLAB, DESY) are kindly acknowledged for their support during the experiments.

For proof reading this thesis, I want to thank Dr. Martin Schroer, Dr. Michael Paulus, Dr. Julia Nase, Verena Ihrig, and Ralf Kuhne.

DELTA, ESRF, Diamond Light Source, and DESY are kindly acknowledged for providing synchrotron radiation and access to their facilities. BMBF is acknowledged for financial support.

Eidesstattliche Erklärung

Hiermit erkläre ich an Eides Statt, dass ich die vorliegende Arbeit ausschließlich unter Anleitung meiner wissenschaftlichen Betreuer und Verwendung der angegebenen Hilfsmittel angefertigt habe. Ich habe keine anderen als die angegebenen Quellen und Hilfsmittel benutzt sowie wörtliche und sinngemäße Zitate kenntlich gemacht. Die Arbeit wurde weder ganz noch in Teilen an anderer Stelle im Rahmen eines Prüfungsverfahrens vorgelegt.

Dortmund, den

_____

(Johannes Möller)